THE UNIVERSITY OF MANITOBA

AN INVESTIGATION OF THE MAGNETIC AND CRYSTALLOGRAPHIC STRUCTURES OF SOME IRON CHALCOGENIDES

by

C. BOUMFORD

A THESIS

SUBMITTED TO THE FACULTY OF GRADUATE STUDIES

IN PARTIAL FULFILLMENT OF THE REQUIREMENTS FOR THE DEGREE

OF DOCTOR OF PHILOSOPHY

DEPARTMENT OF PHYSICS

WINNIPEG, MANITOBA

November 1976

"AN INVESTIGATION OF THE MAGNETIC AND CRYSTALLOGRAPHIC STRUCTURES OF SOME IRON CHALCOGENIDES"

by

C. BOUMFORD

A dissertation submitted to the Faculty of Graduate Studies of the University of Manitoba in partial fulfillment of the requirements of the degree of

DOCTOR OF PHILOSOPHY

To Maggie

ABSTRACT

Experimental studies of the magnetic properties of an iron selenide with a vacancy ordered NiAs structure, and a series of iron containing compounds with the spinel structure, are presented.

The ordering of cation vacancies in the iron selenide Fe_7Se_8 creates two crystallographic superstructures differing in repeat distance along the c axis. The '3c' and '4c' phases are both stable at room temperature causing the magnetic properties of the compound to be extremely sensitive to the thermal history of the sample. Single crystal X-ray techniques are employed to verify that single phase samples could be produced and clear evidence for an abrupt spin rotation at $\sim$130 K is found in samples with the 3c structure from both magnetization and Mössbauer effect measurements. The abrupt changes characteristic of this rotation are not found in the 4c samples.

The Mössbauer spectra are analyzed in terms of overlapping six-line patterns which are identified with iron ions in different crystallographic sites called A, B and C. The isomer shifts of the different patterns indicate that the cations are all in the ferrous state, in conflict with a proposed ionic model. An alternative metallic model is presented which is in agreement with both magnetic and conductivity data.

It is found that cold working the powder samples, even for a brief period of time, leads to a large increase in absorption in the central regions of the Mössbauer spectra, including the appearance of a spectrum characteristic of Fe_3Se_4.

The series $Fe_xCu_{1-x}Rh_2S_4$ ($0 < x \leqslant 0.94$) provides some of the few examples of iron containing spinels with magnetic ions limited to the A-sites. The rhodium occupies the B-sites in an essentially non-magnetic low-spin state. Copper and iron share the A-sites and X-ray results indicate that they order onto the two interpenetrating face-centred-cubic A-site sublattices in the middle region of the series ($0.45 \leqslant x \leqslant 0.7$). It is suggested that the copper ions retain the 1+ valence state throughout the series leaving the iron as the only magnetic ion.

The antiferromagnetic ordering produces unusually high ordering temperatures in the low-iron content members of the series, and displaced hysteresis loops in the compounds with $x > 0.5$. Curie constants, determined from susceptibility measurements above the ordering temperature, indicate that the iron is in the Fe^{3+} state for samples with $x \leqslant 0.5$ but show a gradual change to Fe^{2+} as $x \rightarrow 1$. This is confirmed by the Mössbauer spectra recorded from this series of samples. Evidence for the separate existence of iron in both valence states can be seen in low temperature spectra recorded from absorbers with $x \geqslant 0.7$.

The low temperature Mössbauer spectra become

increasingly broadened and complex as $x \rightarrow 1$, and since the end member of the series, $FeRh_2S_4$, cannot be produced with the spinel structure it is suggested that this broadening is caused by strain induced at the individual iron sites.

ACKNOWLEDGEMENTS

The author would like to take this opportunity to thank Dr. A.H. Morrish for his supervision and constant encouragement throughout this research project. Thanks are also due to Dr. I. Maartense and Dr. M.R. Spender for numerous helpful discussions during the course of the work. The excellent typing was done by Mrs. G. Anderson.

Financial support was received from both the University of Manitoba and the National Research Council of Canada.

CONTENTS

PAGE

INTRODUCTION

Iron chalcogenides have been studied extensively for many years using a number of different techniques. They occur with a wide range of crystal structures and often have interesting magnetic properties. In this thesis chalcogenides with two closely related structures have been investigated. The selenide Fe_7Se_8 crystallises with the nickel arsenide structure whereas sulphides of the series $Fe_xCu_{1-x}Rh_2S_4$ $(0 \leqslant x < 1)$ are spinels. The basis of both structures is a close packed array of anions. Hexagonal-close-packed anions and octahedrally-co-ordinated cations characterize the NiAs structure whereas the spinels have both octahedral and tetrahedral cation sites in a face-centred cubic close-packed array of anions.

Many transition metal oxides are spinels and their sulphide equivalents often retain this structure, Fe_3O_4 and Fe_3S_4 for example. However selenide and telluride spinels are rare, frequently forming cation deficient NiAs structures as do Fe_3Se_4 and Fe_3Te_4. Non-oxide spinels often convert to the NiAs structure on the application of high pressures.[1] This suggests that decreasing the size of the smaller spinel tetrahedral sites either by increasing the pressure or by increasing the anion size may prevent spinel formation. A more detailed description of the two crystal forms is given in later sections.

Synthetic samples were prepared in the laboratory and their crystallographic properties examined using a variety of X-ray diffraction techniques. Magnetization measurements, using a vibrating sample magnetometer, and Mössbauer effect studies were used to investigate the magnetic structures of the compounds.

CHAPTER I

BASIC THEORY

1. X-Ray Techniques

The powder diffractometer and Debye-Scherrer camera are frequently used to analyse future Mössbauer absorbers or simply to check for impurity phases. [2, 3, 4] Single crystal Laue photographs have been used in our laboratory mainly to check crystal symmetry and to align crystals for magnetization measurements. Aligned crystallites have also been cut into slices to form single crystal Mössbauer absorbers.[5] However further X-ray analysis has rarely been attempted since the basic structure of most of the samples studied is usually well documented.

The ordering of the cation vacancies in Fe_7Se_8 leads to a number of different phases described later. In order to distinguish between these phases more complex single crystal techniques had to be used and their theory is outlined below.

1.1 Rotation Photographs

The crystal is rotated about an important axis, usually a principal axis, in a monochromatic beam of X-rays. The diffracted beams form spots which lie on a series of layer lines as shown in Figure 1-1.

The Laue conditions for diffraction maxima from a plane (h k l) are:

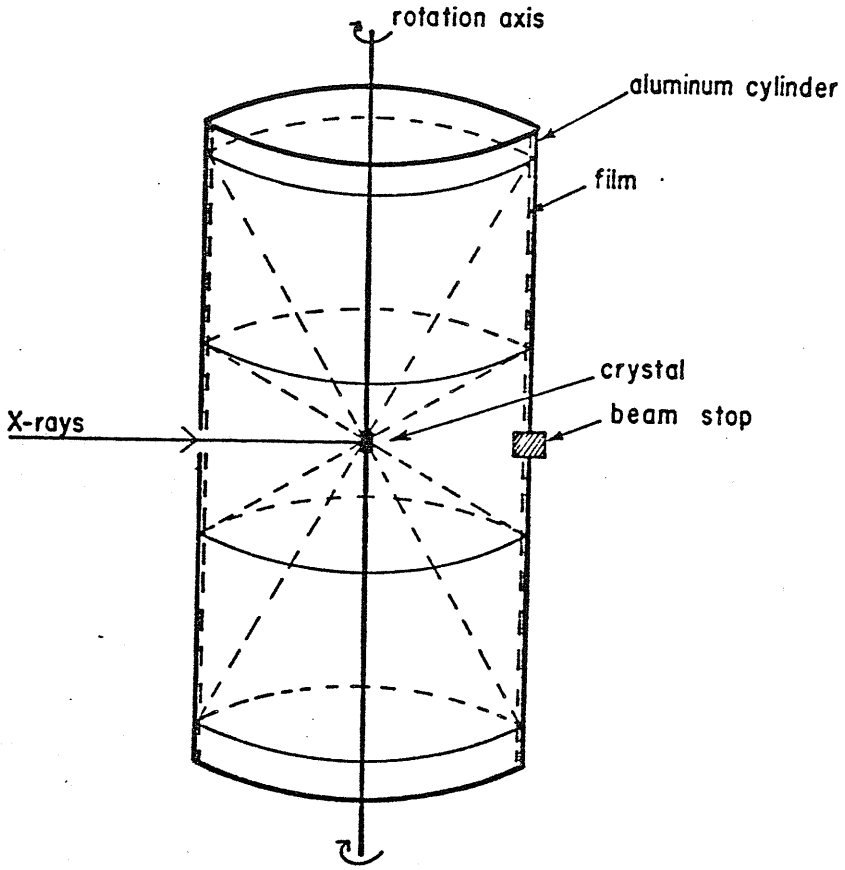

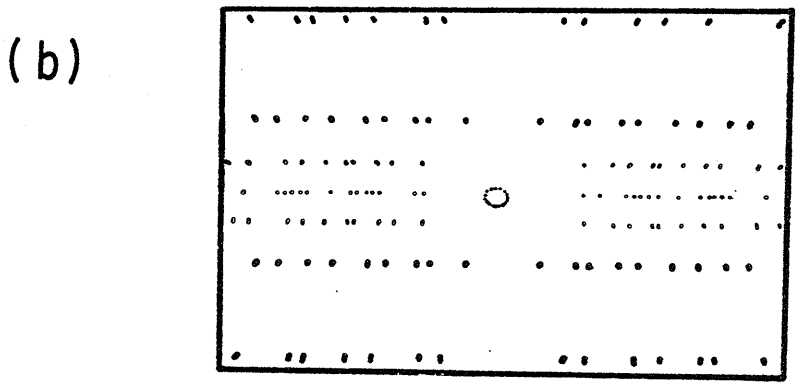

FIGURE 1-1: a) A Rotation Camera with the diffraction cones intersecting a coaxial cylindical film.

b) A typical rotation photograph showing the layer lines.

$$(\underline{S} - \underline{S}_0).\underline{a} = h\lambda$$

$$(\underline{S} - \underline{S}_0).\underline{b} = k\lambda$$

$$(\underline{S} - \underline{S}_0).\underline{c} = l\lambda$$

where $\underline{S}$ and $\underline{S}_0$ are unit vectors in the direction of the incident and diffracted beams and $\underline{r}$ is the shortest lattice vector in the direction about which the crystal is being rotated (Figure 1-2).

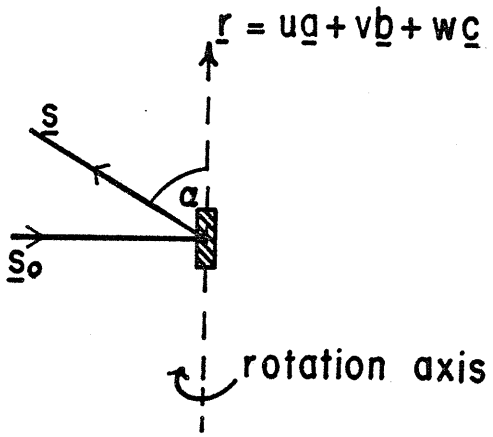

FIGURE 1-2: A diagram of the vectors used in the Laue equations for a rotation photograph.

From the Laue conditions:

$$u\underline{S}.\underline{a} + v\underline{S}.\underline{b} + w\underline{S}.\underline{c} = \lambda (hu + kv + lw)$$

since $\underline{S}_0.\underline{r} = 0$

$$\therefore \frac{\underline{S}.\underline{r}}{\lambda} = hu + kv + lw = \frac{r}{\lambda} \cos \alpha$$

$$hu + kv + lw = 0, 1, 2....n \qquad (1)$$

$$\therefore \cos \alpha = \frac{n \lambda}{r}$$ where n is the order of the layer line.

e.g. If an orthorhombic crystal of cell dimensions $\underline{a}$ $\underline{b}$ $\underline{c}$ is rotated about the $[001]$ direction then

$$c = \frac{n \lambda}{\cos \alpha}$$

$\cos \alpha$ can be measured from the spacing of the layer lines. It should be noted that equation (1) is a general condition for layer lines. For an actual spot to form, all the Laue conditions must be satisfied simulataneously.

Rotation photographs may be indexed using a Bernal chart but some ambiguity remains. For example indexing the $\{111\}$ reflections of a cubic crystal rotated about the c axis, a spot will appear at the same position from the (111), $(\bar{1}11)$, $(1\bar{1}1)$ and $(\bar{1}\bar{1}1)$ planes. Some of this ambiguity can be removed by oscillating the crystal over a few degrees rather than rotating through a full 360^{o}.

1.2 The Precession Method

Difficulties encountered with fixed film methods usually arise from attempting to map the three indices h, k and l onto the two dimensions of a photographic film. The precession method overcomes this problem by isolating a set of reflections with one index constant, and then moving the film so as to split up the remaining indices. It is based on the de Jong-Bouman method devised in 1938 for recording the reciprocal lattice in undistorted form on a flat film.[6] It is illustrated in Figures 1-3a and 1-3b for a crystal rotated about its c axis. On rotation of the crystal, the reciprocal lattice rotates about the normal at P causing the different planes to sweep through the sphere of reflection. An annular screen permits only reflections from one specific level through to the film and an undistorted photograph of this level is recorded by causing the film to duplicate the motion of the level, i.e. rotating it about P' in phase with rotation of the crystal.

The precession method was developed from a generalization of the de Jong-Bouman principle. Any level of the reciprocal lattice can be recorded on a flat film without distortion and any motion of the reciprocal lattice whatever can be utilized to bring the various points into reflecting condition providing only that a corresponding motion is given to the photographic film. The precession method was devised by M.J. Buerger.[7, 8] Instead of a simple rotation movement, the normal to the reflecting

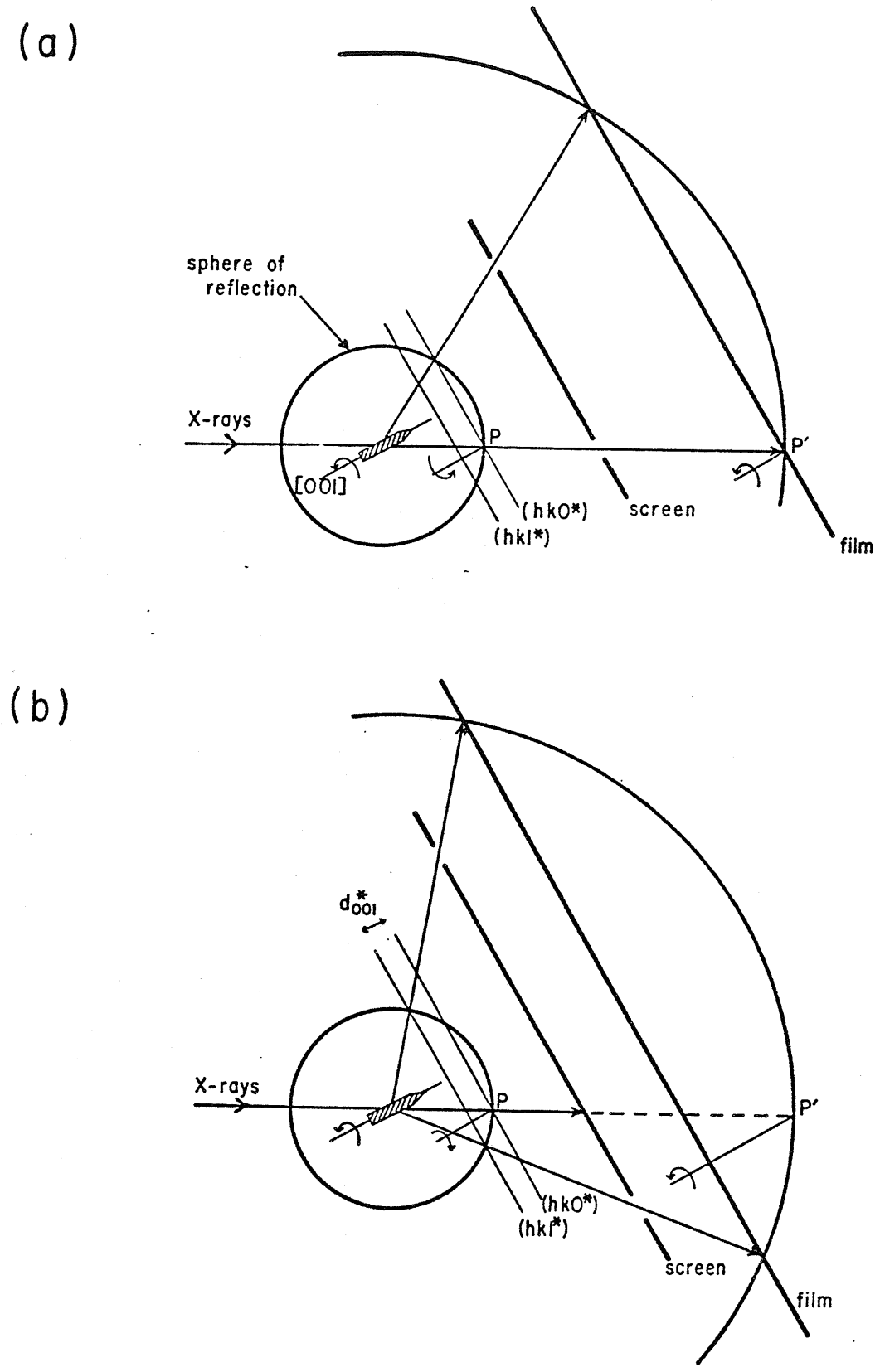

FIGURE 1-3: A diagramatic representation of the de Jong-Bouman method of recording a) the zero level and b) the 1st level of reflections.

plane is caused to precess about the X-ray beam at a constant angle to it. A diagram of the instrument is shown in Figure 1-4.

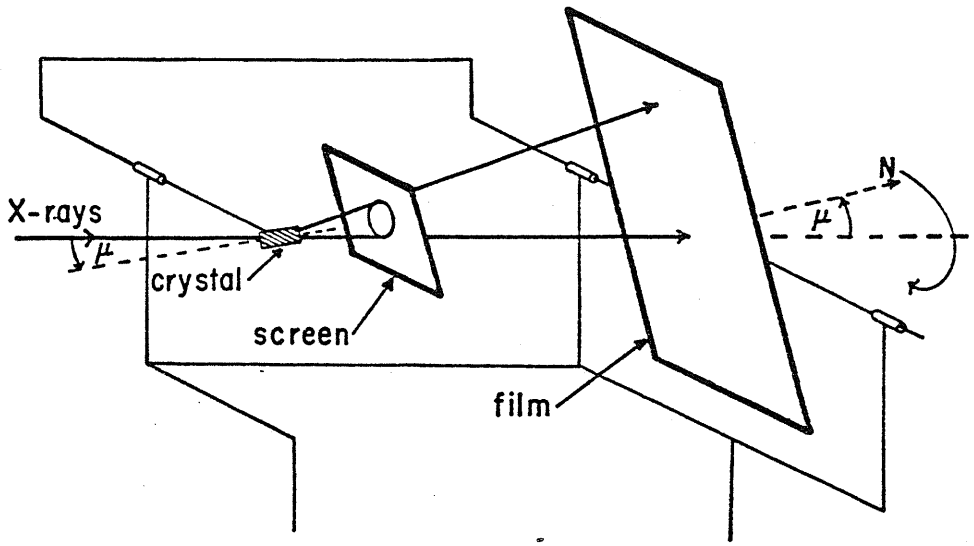

FIGURE 1-4: The Buerger Precession Instrument.

The various linkages serve only to cause the film to move in simultaneous motion with the reflecting plane.

Since only a limited number of reflections can be recorded with this method, it is advantageous to use a short wavelength radiation, thus increasing the area of the reciprocal lattice recorded by increasing the radius of the reflecting sphere (= $1/\lambda$).

2. Magnetization Measurements

A paramagnetic material containing N atoms per unit volume, each bearing a magnetic moment μ , will have a susceptibility χ which is inversely proportional to the temperature.

$$\chi = \frac{N \mu_{eff}^2 \mu_B^2}{3\ kT} = \frac{C}{T}$$

$\mu_{eff} = g\left[J(J+1)\right]^{\frac{1}{2}}$ is called the effective number of Bohr magnetons.

C is the Curie constant.

$$\therefore \mu_{eff}^2 = \frac{3kC}{N\mu_B^2}$$

In the transition metal series the electric field produced by the neighbouring ions (Crystal Field) on the outer 3d electrons tends to break up the L-S coupling and remove the degeneracy of the 2L + 1 orbital levels. This splitting diminishes the contribution of the orbital motion to the magnetic moment so that

$$\mu_{eff} = g\left[S(S+1)\right]^{\frac{1}{2}} \quad (g = 2 \text{ the spin only value})$$

is often in better agreement with experimental values.

Given an internal interaction between the magnetic moments which at some temperature overcomes the thermal motion, magnetic ordering will take place. This interaction can be represented by a magnetic field H_e called the

exchange or molecular field. From the Weiss Molecular Field theory H_e is proportional to the magnetization M

$$H_e = N_w M$$

where N_w is the molecular field constant. i.e. Each spin sees the average magnetization of the rest of the spins.

Due to this interaction, far enough above the ordering temperature the susceptibility retains a temperature dependance very similar to that of a paramagnet.

$$\chi = \frac{C}{T - \theta} \qquad \theta = \text{Weiss parameter}$$

for ferromagnetic materials.

$$\chi = \frac{C}{T + \theta}$$

for antiferromagnets. For a ferromagnet using the molecular field approximation this becomes:

$$\chi = \frac{C}{T - CN_w}$$

giving $\theta = CN_w = T_c$

where T_c is the Curie Point.

$$N_w = \frac{T_c}{C} = \frac{3kT_c}{Ng^2S(S+1)\,\mu_B{}^2}$$

For iron this gives a molecular field of the order of 10^7 Oersteds. This is much greater than the dipole field

produced at an ion site by other ions in the crystal.[9] In fact, the molecular field is only an approximate representation of the quantum mechanical exchange interactions produced by overlap of the charge distributions of neighbouring ions. It can be seen however that the effect of any magnetic field produced in the laboratory is likely to be small compared to interactions of this magnitude. There is no exact classical analogue of the exchange energy since its origin lies in the Pauli exclusion principle. A change in the relative direction of two spins will cause the spacial charge distribution to change, thus affecting the Coulomb energy of the system. Therefore neighbouring spins act as if a direct coupling existed between them, leading to the concept of a very large internal magnetic field.

A ferromagnetic material has a singularity in the susceptibility at the ordering or Curie temperature. Below this temperature a spontaneous moment exists (neglecting domain formation). The magnetic moment μ, is given by

$$\mu = g \mu_B S$$

Therefore the saturation magnetization at absolute zero will give a value for the average moment and hence the spin of each ion.

In a Néel antiferromagnet the spins are ordered in an antiparallel arrangement with zero net moment at

temperatures below the ordering or Néel temperature. The susceptibility is not infinite at the Néel point but usually shows a weak cusp in the susceptibility versus temperature curve just above the ordering temperature.[10]

Ferrimagnetism was originally postulated by Néel to explain the magnetic properties of ferrites.[11] Here the ordering is similar to that of an antiferromagnet except that either the number or size of the moments on the different magnetic sublattices differ. Far above the ordering temperature (T_{FN}) the susceptibility follows the Curie-Weiss law of the antiferromagnet, but a spontaneous moment exists below T_{FN}. Since the moments on each sublattice may have a different temperature dependence, the magnetization below T_{FN} can be complex. However it may provide valuable information for determining the spin distribution between the various sublattices.

More complex spin arrangements occur. These arise due to competing magnetic interactions or anisotropy axes which cause non-collinear alignment of the different sublattices,[9] leading to triangular or spiral structures.

3. The Mössbauer Effect

The phenomenon of recoil-free emission or absorption of a gamma ray by a nucleus bound in a crystal, was first observed in 1957 by R.L. Mössbauer.[12] He discovered that an ^{191}Ir nucleus can decay to its ground state with a finite probability of emitting no phonons in the process, the recoil momentum being taken up by the whole lattice.

The energy of recoil of the nucleus, $E_R = \frac{1}{2} M v^2$

$$\therefore E_R = \frac{p^2}{2M} = \frac{E_\gamma^2}{2Mc^2}$$

where E_γ is the energy of the γ-ray emitted. It can be seen that if the emitting nucleus is unable to recoil freely due to chemical binding, the recoiling mass can be considered to be the mass of the crystal rather than the mass of the emitting nucleus. This reduces the recoil velocity to negligible values.

The property which has made these zero-phonon gamma rays so valuable is to be found in their linewidths. If the lattice is not excited, only the widths of the nuclear levels determine the linewidth of the emitted gamma ray. For a nuclear lifetime of 10^{-7} s the uncertainty principle predicts a width $\sim 10^{-8}$ eV. For a 100 KeV gamma ray this is equivalent to saying that the energy is defined to less than one part in 10^{13}. More important however is the fact that 10^{-8} eV is smaller than characteristic values for the various interactions of nuclei with their

own electrons. Due to this fact, although Mössbauer's original discovery was in the realms of nuclear physics, its principal applications have been in solid state physics, the nucleus being used as a probe to sample its immediate environment. The isomer shift, quadrupole interaction and hyperfine field at the nucleus, measurable quantities in Mössbauer studies, are all affected by the surrounding electrons.

Although theoretically present in all excited state-ground state gamma ray transitions, Mössbauer gamma rays have been detected in only 101 transitions in 83 isotopes of 44 different elements. Of these, all but a few require extreme experimental conditions which eliminate them as a useful tool for solid state applications.[13]

Many of the conditions necessary for an isotope to exhibit a detectable Mössbauer effect may be deduced from the expression for the recoil free fraction f.

$$f = \exp\left(-\frac{E_\gamma^2 \langle x^2 \rangle}{\hbar^2 c^2}\right)$$

where $\langle x^2 \rangle$ is the component of the mean square vibrational amplitude of the nucleus in the direction of emission of the gamma ray. If E_γ^2 or $\langle x^2 \rangle$ are too large then f becomes negligible. The highest transition energy for which a measurable Mössbauer effect has been reported is 155 keV for ^{188}Os [14] but to be useful as a source of gamma rays in a Mössbauer experiment, E_γ must be less than 50 keV if the

experiment is to be performed without cooling the source. The exponential dependence of f on $\langle x^2 \rangle$ makes the Mössbauer effect undetectable in gases or non viscous liquids.

For resonant absorption it is also necessary that the recoil energy of the crystal in which the nucleus is bound does not exceed the natural linewidth of the gamma ray. This requires particles of $\sim 10^6$ atoms. Since even fine powder particles are a factor of 10^9 larger than this, the recoil energy is evidently negligible. For solid-state applications, the half-life of the excited state must be such that the natural linewidth of the gamma ray is at least an order of magnitude less than the hyperfine interactions.

The two transitions which best satisfy the above conditions are the 14.41 keV, $3/2 \rightarrow 1/2$ transition in ^{57}Fe and the 23.87 keV $3/2 \rightarrow 1/2$ transition in ^{119}Sn, both of which have been used in our laboratory. The experiments in this thesis were performed on ^{57}Fe which is a stable isotope constituting 2.17% of natural iron. ^{57}Co diffused into a suitable matrix is usually used as a source. Its decay scheme together with some important nuclear parameters for ^{57}Fe are shown in Figure 1-5.

In a Mössbauer spectrum, the emission and absorption lines must be folded together so that the minimum linewidth will be 2Γ . The distribution of energies about E_0 is

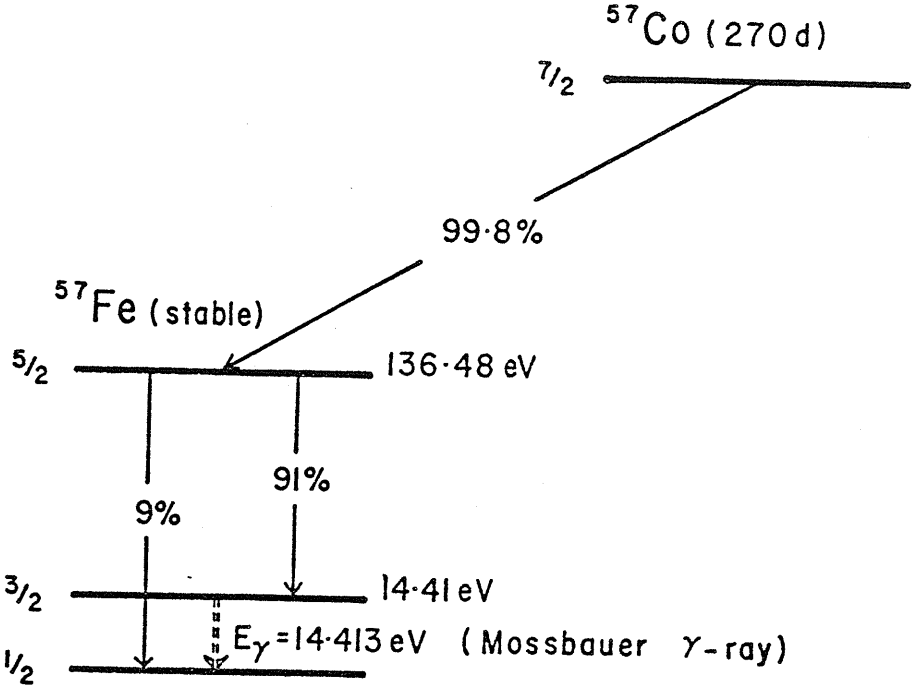

Quadrupole Moments	$Q_{1/2}$ = 0b	$Q_{3/2}$ ~ 0.21 b
Nuclear g factors	$g_{1/2}$ = 0.181	$g_{3/2}$ = -0.103

Natural linewidth (Γ) = 4.665×10^{-9} eV

Natural lifetime ($\tau_{1/2}$) = 9.78×10^{-9} s

Minimum experimental linewidth (2Γ) = 0.194 mm/s

FIGURE 1-5: The ^{57}Co decay scheme and some important parameters for the I = 3/2 and I = 1/2 nuclear states.

given by the Breit-Wigner formula[15] and leads to a Lorentzian lineshape

$$I(E_\gamma) = \frac{I(E_0)}{\left(\frac{2(E_\gamma - E_0)}{\Gamma}\right)^2 + 1}$$

By moving the source relative to the sample we can Doppler shift the energy of the gamma ray

$$\frac{\Delta E}{E_\gamma} = {}^{v}/_{c}$$

where v is velocity of the source in the gamma ray direction 1 mm/s $= 4.804 \times 10^{-8}$eV for ^{57}Fe. Since the hyperfine splitting of nuclear levels is $\sim 10^{-7}$eV, mm/s have become the conventional Mössbauer energy units.

If a hyperfine splitting is to be observed in a Mössbauer experiment then the fluctuation time of the electronic spin (τ_s) i.e. the fluctuation time of the hyperfine field, must be long compared to the lifetime of the excited state of the Mössbauer nucleus ($\tau_{1/2}$). Fluctuations must also be longer than the Larmor precession time of the nucleus. If ω_L is the Larmor precession frequency, then

$$\tau_s > \tau_{1/2} > 1/\omega_L$$

4. Hyperfine Interactions

The Hamiltonian for the hyperfine interaction between a nucleus and its surroundings can be written as

$$H = E_0 + M_1 + E_2$$

neglecting higher terms. E_0 represents the electric monopole (i.e. Coulomb) interaction between the nuclear and electronic charge density due to the finite nuclear size and is usually called the Isomer Shift. M_1 refers to interaction of the nuclear magnetic dipole with the hyperfine field of the electrons. E_2 represents the interaction of the nuclear quadrupole moment with the electric field gradient at the nucleus.

4.1 The Isomer Shift

The E_0 interaction alters the energy separation between ground and excited states of the nucleus causing a shift in position of the observed resonance line. The nuclear volume must be taken into account when considering nucleus-electron interactions due to the finite s electron density at the nucleus. A change in volume of the nucleus during emission or absorption of the gamma ray will cause a change in the Coulomb interaction energy.

Consider the nucleus as a uniformly charged sphere radius R and let the electronic charge density over the nuclear volume be ρ . Let the difference in electrostatic energy between the point and the finite nucleus be δE.

The Electrostatic potential for the finite nucleus

$$V = \frac{Ze}{R}\left(\frac{3}{2} - \frac{r^2}{2R^2}\right) \qquad r \leqslant R$$

$$V = V_{pt} = \frac{Ze}{r} \qquad r \geqslant R$$

$$\delta E = \int_0^{\infty} \rho (V - V_{pt})\, 4\pi r^2\, dr$$

$$= -\frac{2\pi}{5} Ze\, \rho\, R^2 = \frac{2\pi}{5} Ze^2 \left|\psi(0)\right|^2 R^2$$

where $-e\left|\psi(0)\right|^2$ replaces ρ the electronic charge density.

A gamma ray results from a transition between two levels with different nuclear radii $R_{excited}$ and R_{ground}

$$\delta E_{ex} - \delta E_{gd} = \frac{2\pi}{5} Ze^2 \left|\psi(0)\right|^2 \left\{R^2_{excited} - R^2_{ground}\right\}$$

$$= K \times \left|\psi(0)\right|^2$$

where the constant K depends on nuclear parameters. n.b. its value will change for different Mössbauer nuclei. What is observed in the Mössbauer experiment is the difference in energy shifts between source and absorber.

i.e. The Isomer Shift $\delta = K \times \left\{\left|\psi_a(0)\right|^2 - \left|\psi_s(0)\right|^2\right\}$

Therefore δ is dependent on the charge density at the nucleus and will be very much affected by the valence state of the atom, screening effects of p, d and f electrons or by covalency and bond formation.

The 14.41 KeV excited state of iron has a smaller nuclear radius than the ground state therefore the constant K is negative. i.e. A positive isomer shift signifies a decrease in s electron density at the nucleus in going from source to absorber.

4.2 Second Order Doppler Shift

There is a second contribution to the shift of the observed resonance line, which is temperature dependent and arises from second order Doppler effects. The relativistic expression for the Doppler shift is

$$E = E_\gamma\left(1 - \frac{v}{c}\right)\left(1 - \frac{v^2}{c^2}\right)^{-\frac{1}{2}}$$

where v is the velocity of the vibrating nucleus. Since vibration frequencies are $\sim 10^{13}\ s^{-1}$, the first order terms will average to zero over the lifetime of the excited nuclear state.[16] Second order effects will not average to zero however and the Mössbauer line will experience a shift δ_D given by

$$\delta_D = -\ E_\gamma \cdot \frac{1}{2}\ \frac{v^2}{c^2} \qquad \text{giving}$$

$$\frac{\partial \delta_D}{\partial T} = -\ \frac{1}{2}\ E_\gamma\ \frac{C_p}{Mc^2}$$

where C_p is the specific heat of the lattice at constant pressure. In the high temperature limit ($C_p = 3k$) this gives

$$\delta_D = -\ 7.31 \times 10^{-4} \quad \text{mm/s/K}$$

By using the Debye Model to obtain an expression for the lattice vibration energy then

$$\delta_D = -\frac{9kE_\gamma}{4Mc^2}\left(\frac{\theta_D}{4T} + 2\left(\frac{T}{\theta_D}\right)^3 \int_0^{\theta_D/T} \frac{x^3}{e^x - 1}\, dx\right) T$$

$$= 1.1 \times T\left(\frac{\theta_D}{4T} + 2\left(\frac{T}{\theta_D}\right)^3 \int_0^{\theta_D/T} \frac{x^3}{e^x - 1}\, dx\right) \text{mm/s}$$

for ^{57}Fe.

Universal curves have been plotted from this function[17] so that it is possible to subtract δ_D from the observed shift providing δ_D is the same over the whole temperature range.

4.3 Electric Quadrupole Interactions

The interaction E_2 between the nuclear electric quadrupole moment Q, and the electric field gradient is expressed by the Hamiltonian

$$H_Q = Q.\ \nabla E$$

Nuclei with spin I = 0 or ½ are spherically symmetric and have a zero quadrupole moment e.g. The ground state of ^{57}Fe with I = ½ exhibits no quadrupole splitting. Nuclei with I > ½ have non-spherical charge distributions which if expanded as a series of multipoles contain a quadrupole term. The electric field gradient is a 3 x 3 tensor which reduces to diagonal form so that it can be

completely specified by the terms $\partial^2 V / \partial x_i \partial x_i$ (abbreviated to V_{xx} V_{yy} V_{zz}) where V is the electrostatic potential.

Only s electrons have a finite charge density at the nucleus and since they are spherically symmetric they will not contribute to the field gradient. Since there are no other free charges at the nucleus, Laplace's equation restricts the number of independent parameters in the electric field gradient to two.

$$\nabla^2 V = V_{xx} + V_{yy} + V_{zz} = 0$$

By convention[16] $V_{zz} = eq$ is the maximum value of the field gradient and chosen as one of the independent parameters. The other is the asymmetry parameter η defined as

$$\eta = \frac{(V_{xx} - V_{yy})}{V_{zz}}$$

$0 \leqslant \eta \leqslant 1$ since by convention $|V_{zz}| > |V_{yy}| \geqslant |V_{xx}|$

The Hamiltonian may be written:

$$H_Q = \frac{V_{zz} Qe}{4I(2I-1)} \left\{ 3 I_z^2 - I(I+1) + \frac{\eta}{2} (I_+^2 + I_-^2) \right\}$$

where I_+ and I_- are raising and lowering operators. For $I = 3/2$ this gives eigenvalues

$$E_Q = \frac{V_{zz} Qe}{4I(2I-1)} \left\{ 3 M_I^2 - I(I+1) \right\} (1 + \eta^2/3)^{\frac{1}{2}}$$

$M_I = I, (I-1), \ldots -I$

For the ^{57}Fe nucleus, the first excited state is split in two, $M_I = \pm 3/2$ and $M_I = \pm \frac{1}{2}$ as shown in Figure 1-6, separated by an energy ϵ where

$$\epsilon = \frac{e^2qQ}{2} \left(1 + \eta^2/_3\right)^{\frac{1}{2}}$$

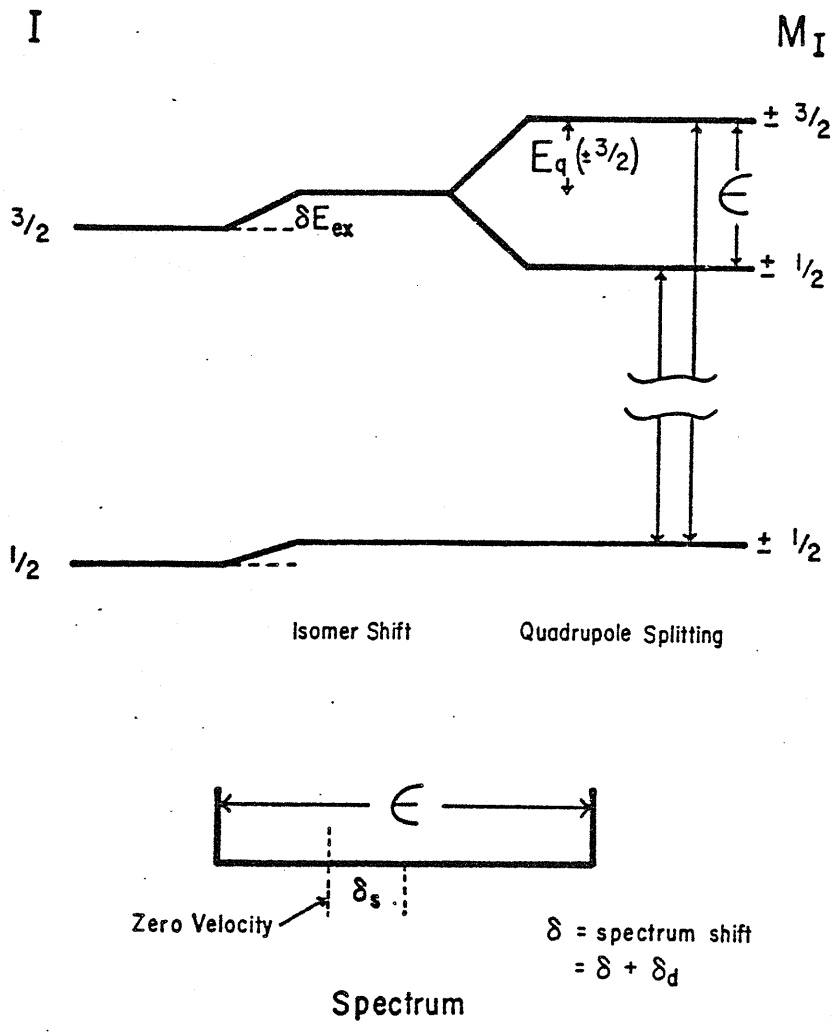

FIGURE 1-6: The isomer shift and quadrupole splitting of the nuclear levels of ^{57}Fe.

The electric field gradient at the nucleus contains contributions from the valence electrons of the atom and from the surrounding ionic charges in the lattice . The principal component V_{zz} may be written[18]

$$V_{zz} = (1 - \gamma_\infty) V_{zz}^{lat} + (1 - R) V_{zz}^{ion}$$

The parameters γ_∞ and R are the Sternheimer antishielding factors for the lattice and ionic contributions. Normally polarization of the inner spherical shells of the ion enhances V_{zz}^{lat}. In the case of ^{57}Fe, $\gamma_\infty = -9.14$ and $R = 0.32$.[18]

There are a number of ways of calculating V_{zz}^{lat} making use of various modification of the point charge model.[19] All in general have some procedure for calculating $\frac{e_i (3 \cos^2\theta_i - 1)}{r_i^3}$ for each surrounding ion on the central ion, and summing over the lattice. The ionic contribution is a result of non-spherical symmetry of the charge distribution. Fe^{3+} has a half filled d shell (5 electrons) and is spherically symmetric i.e. $V_{zz}^{ion} = 0$. Fe^{2+} has an extra 3d electron outside the shell which, in environments with symmetry lower than cubic, may cause large polarization of inner shells and hence a large contribution of V_{zz}^{ion}.

4.4 Magnetic Hyperfine Interactions (Nuclear Zeeman Effect)

The Hamiltonian describing the magnetic dipole hyperfine interaction is:

$$H_{mag} = - \underline{\mu}.\underline{H} = - g\mu_N \underline{I}.\underline{H}$$

where H is the field at the nucleus, $\underline{\mu}$ is the nuclear magnetic moment, μ_N is the nuclear Bohr magneton ($e\hbar/2Mc$), g is the nuclear g factor and I is the nuclear spin. If $\underline{H}$ defines the axis of quantization this Hamiltonian has eigenvalues

$$E_{mag} = \frac{- \mu H M_I}{I} = -g \mu_N H M_I$$

$$M_I = I, I-1 \ldots\ldots\ldots -I$$

Thus the (2I + 1) fold degeneracy of the nuclear states is lifted. This situation is illustrated for ^{57}Fe in Figure 1-7. Only $\Delta M_I = 0, \pm 1$ transitions are allowed and their angular dependence is given in Table 1-1. Integrated over all θ, the angle between the γ-ray direction and $\underline{H}$, this gives the relative intensities indicated. Therefore for a randomly oriented poly-crystalline absorber with no quadrupole interactions, we expect a symmetrical six-line Mössbauer spectrum with intensities 3:2:1:1:2:3. From the angular dependence it can be seen that if $\theta = 0$ only $\Delta M_I = \pm 1$ transitions are allowed, resulting in a 4-line spectrum with an intensity

ratio 3:1:1:3. This situation will arise if the γ-rays are directed along the easy axis of a single crystal i.e. parallel to $\underline{H}$, or if the sample (polycrystalline or single crystal) can be completely saturated by application of a large external magnetic field parallel to the gamma ray direction.

Magnetic Splitting

Transition	ΔM_I	Relative Probability	Angular Dependence
3/2 → 1/2	-1	3	9/4 $(1 + \cos^2\theta)$
-3/2 → -1/2	+1		
1/2 → 1/2	0	2	3 $\sin^2\theta$
-1/2 → -1/2	0		
-1/2 → 1/2	+1	1	3/4 $(1 + \cos^2\theta)$
1/2 → -1/2	-1		

Quadrupole Splitting

$\pm$3/2 → $\pm$1/2	$\pm$1	1	3/2 $(1 + \cos^2\theta)$
$\pm$1/2 → $\pm$1/2	0	1	1 + 3/2 $\sin^2\theta$

TABLE 1-1: The allowed excited state → ground state transitions of ^{57}Fe.

There are several contributions to the hyperfine field H. A general expression would be

$$H = H_0 - DM + \frac{4}{3}\pi M + H_S + H_L + H_D$$

H_0 is the externally applied magnetic field. The next two terms are the demagnetizing and Lorentz fields respectively. Both are usually small and exactly cancel for spherical single domain particles.[9] H_S is a result of the interaction of the nucleus with the s electron spin density at the nucleus. It is usually the largest contribution to H (10^5 - 10^6 0e) and can be written:

$$H_S = -\frac{16\pi}{3} \mu_B < (\Sigma (s\uparrow - s\downarrow)) >$$

where $s\uparrow$ and $s\downarrow$ are the s electron spin densities at the nucleus with spin up and spin down. H_S is referred to as the Fermi contact term and is very large even in atoms with filled s-shells if the atom contains a partially filled magnetic shell. The exchange interaction between a spin-up polarized d-shell and the spin-up s-electron is attractive whereas that between the d-shell and the spin-down s-electron is repulsive. Hence the radial parts of the s-electron wave functions will be distorted giving an imbalance of spin density at the nucleus. Calculations using this polarization scheme[20] predict the approximate magnitude and the sign of the hyperfine field in high spin iron ions. The direction of the hyperfine field is

opposite to the ionic moment in ^{57}Fe.

H_L is the contribution from the orbital angular momentum, given by

$$H_L = -2\mu_B \frac{\langle \underline{L} \rangle}{\langle r^3 \rangle}$$

It is estimated to be $\sim +\ 7 \times 10^4$ Oe in iron metal but is zero for Fe^{3+} since L = 0.

The final term H_D arises from the dipolar interaction of the nucleus with either the spin moment of the atom itself or with the moment on surrounding magnetic atoms. It is expressed in the usual dipole form

$$H_D = -2\mu_B \left\langle \left(\frac{3\underline{r}\ (\underline{S}.\underline{r})}{r^5} - \frac{\underline{S}}{r^3} \right) \right\rangle$$

and can give contributions of the order of 10^4 Oe to the hyperfine field.

The above description of the origins of the internal field suggests that a hyperfine splitting would be observed for all compounds with unpaired valence electrons. The electronic spins which generate H are subject to fluctuations, so in order to observe the splitting with a Mossbuaer spectrometer, the time scale of these fluctuations must obey $\tau_S > \tau_{1/2} > 1/\omega_L$ as explained earlier. In paramagnetic materials these fluctuations are usually rapid and result in H having a time average of zero so that no magnetic splitting is seen. When

magnetic ordering takes place the relaxation rates are effectively slower and a splitting is observed. Complicated Mössbauer spectra arise when the spin relaxation time becomes comparable with that of the nuclear transition.[21, 22]

4.5 Combined Magnetic and Quadrupole Interactions

The complete interaction of the nucleus with its surroundings may now be expressed by the Hamiltonian:

$$H(I) = g_I \mu_N \underline{I}\cdot\underline{H} + \underline{Q}_I.\nabla\epsilon + \frac{2\pi}{5} Z R_I^2 e^2 \left|\psi(0)\right|^2$$

Analytical solutions can not generally be found, but several computer programs have been developed to calculate the Mössbauer spectrum mathematically.[23, 24, 25]

In the case where the quadrupole splitting is small compared to the magnetic interaction ($\underline{Q}.\nabla\epsilon \ll g\mu_N \underline{I}\underline{H}$) and the electric field gradient symmetric ($\eta = 0$), the following solutions exist:[16]

$$E_{3/2} = g_{3/2}\mu_N H M_I + (-1)^{\left|M_I + \frac{1}{2}\right|} \frac{e^2qQ}{4}\left\{\frac{3\cos^2\theta - 1}{2}\right\} + \frac{2\pi}{5} Ze^2 R_{3/2}^2 \left|\psi(0)\right|^2$$

$$E_{1/2} = g_{1/2}\mu_N H M_I + \frac{2\pi}{5} Ze^2 R_{1/2}^2 \left|\psi(0)\right|^2$$

where θ is the angle between the hyperfine field and the principal axis of the electric field gradient. These are the energy levels shown in Figure 1-7.

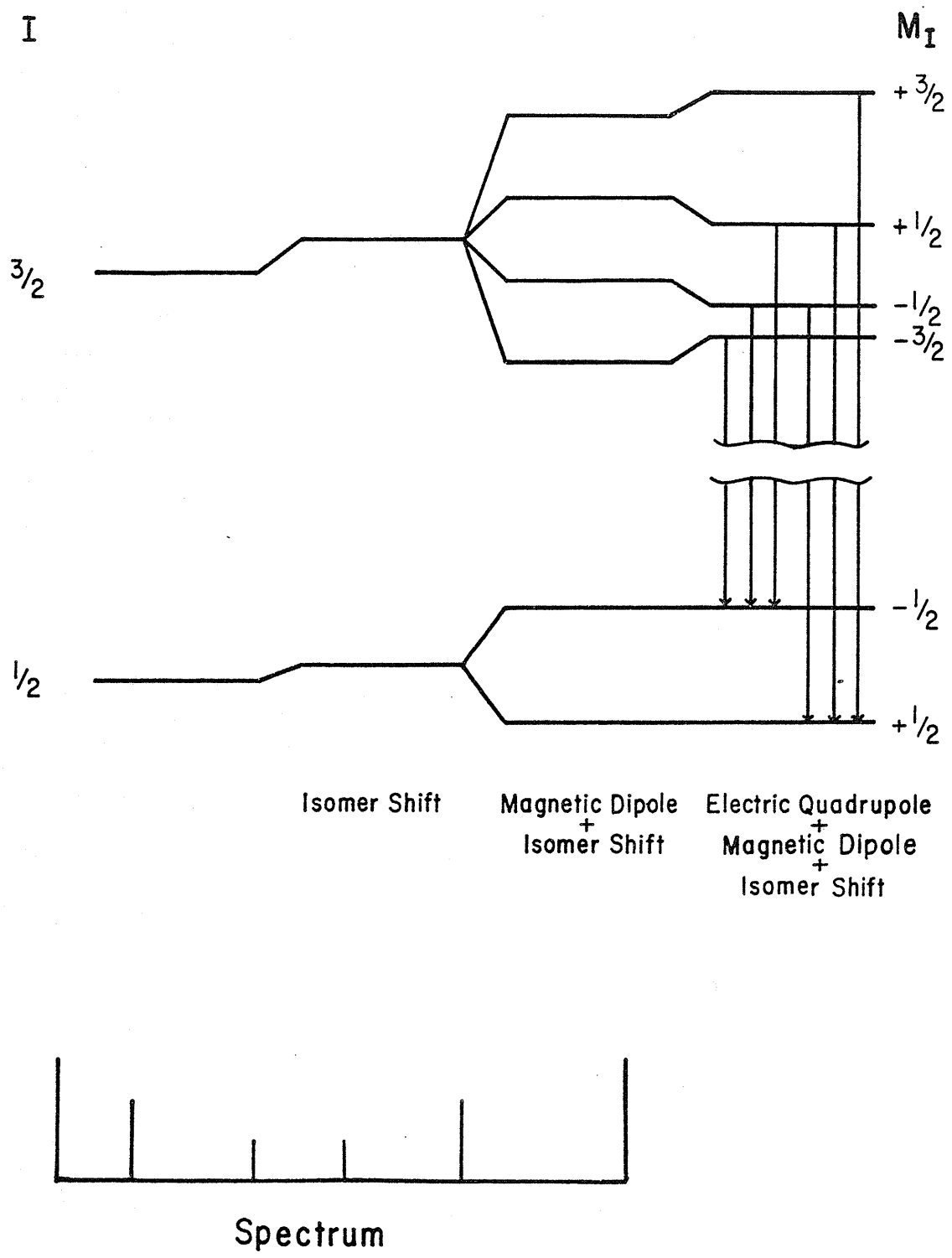

FIGURE 1-7: The combined isomer shift, electric quadrupole and magnetic dipole splitting of the ground and first excited state of ^{57}Fe.

REFERENCES - CHAPTER I

1. R.E. Tressler and V.S. Stabican, N.B.S. Pub. 364, (Sol. State Chem. Proc. of 5th Mat. Res. Symp., 1972) p. 695.
2. S. Hafner and M. Kalvius, Z. Kristallogr. 123, 443 (1966).
3. E.N. Goncharov, Yu. M. Ostanevich, S.B. Tomilov and L. Cser, Phys. Stat. Sol. 37, 141 (1970).
4. J.A. Morice, L.V.C. Rees and D.T. Rickard, J. Inorg. Nucl. Chem. 31, 3797 (1969).
5. J.A. Eaton, Ph.D. Thesis, University of Manitoba (1970).
6. E.W. Nuffield, X-Ray Diffraction Methods, John Wiley and Sons, New York (1966).
7. M.J. Buerger, X-ray Crystallography, John Wiley and Sons, New York (1942).
8. M.J. Buerger, The Precession Method, John Wiley and Sons, New York (1964).
9. A.H. Morrish, The Physical Principles of Magnetism, John Wiley, New York (1965).
10. J.S. Smart, Effective Field Theories of Magnetism, Sanders, Philadelphia (1966).
11. L. Néel, Ann. Phys. (Paris) 3, 137 (1948).
12. R.L. Mössbauer, Z. Phys. 151, 124 (1958).
13. Mossbauer Effect Data Index, 1974, John Wiley, New York (1974).
14. L. Grodzins and Y.W. Chow, Phys. Rev., 142, 86 (1966).

15. G. Breit and E. Wigner, Phys. Rev., 49, 519 (1936).

16. N.N. Greenwood and T.C. Gibb, Mössbauer Spectroscopy, Chapman and Hall Ltd., London (1971).

17. J.M.D. Coey, Ph.D. Thesis, University of Manitoba (1971).

18. R. Sternheimer, Phys. Rev. 146, 140 (1966).

19. F. de Wette, Phys. Rev. 123, 103 (1961).

20. R. Watson and A. Freeman, Phys. Rev. 123, 2027 (1961)

21. M. Blume, Phys. Rev. Letters, 14, 96 (1965)

22. H.H. Wickman, in Mössbauer Effect Methodology, Vol. 2, Plenum Press, New York (1966).

23. G.R. Hoy and S. Chandra, J. Chem. Phys, 47, 961 (1967).

24. W. Kündig, Nuclear Instr. Methods, 48, 219 (1967)

25. J.R. Gabriel and D. Olsen, Nuclear Instr. Methods 70, 209 (1969).

CHAPTER II

EQUIPMENT AND TECHNIQUES

1. X-Ray Diffraction

A variety of X-ray diffraction techniques were used for sample analysis. For powder samples, Debye-Scherrer photographs provided accurate lattice parameters and a room-temperature powder diffractometer was used to detect the presence of impurity phases or to compare line intensities. Small single crystals of the selenide compound could be produced which enabled the vacancy ordering in this sample to be examined in more detail using single crystal X-ray methods.[1] Laue photographs were used to align the crystals which were then rotated about one of their principal axes in a rotation camera. This camera was built by the department machine-shop. It consists of an electric motor which rotates the sample about the axis of an aluminium cylinder of known radius against the inside of which a sheet of film is held. A collimator directs the monochromatic beam of X-rays onto the sample.

Further single-crystal work on this compound was performed using the Buerger precession camera[2] belonging to the Crystallography Laboratory in the Department of Earth Sciences. This method provides undistorted pictures of planes of the reciprocal lattice.[3] It is much more complex and time consuming than fixed film X-ray techniques but interpretation of the results is more straightforward.

For accurate determination of lattice parameters, Debye-Scherrer powder photographs provide the best results. If a single crystal is available however it may not be convenient to grind it to a powder. The crystal may be required for other types of measurements or, as in the case of Fe_7Se_8, grinding may introduce undesirable side effects. If this is the case, the Gandolfi camera may be used to provide 'powder' photographs of a single crystal. The camera itself is identical to the Debye-Scherrer camera, but the sample mount is designed to rotate the crystal in different directions so as to duplicate the random orientation of the powder crystallites with respect to the X-ray beam.

A recent addition to the X-ray equipment in the Physics Department has been a low-temperature attachment to the powder diffractometer. Temperatures of 2 to 300 K are attainable by controlled transfer of liquid helium from a storage dewar. The helium flows at a constant rate through a high efficiency transfer line to the copper sample block. A schematic diagram of the equipment is shown in Figure 2-1. A micrometer needle valve (Figure 2-2) permits precise control of the flow rate and a sample block heater connected to an automatic temperature controller provides a stability of better than ±0.1 K from 4.2 to 300 K.

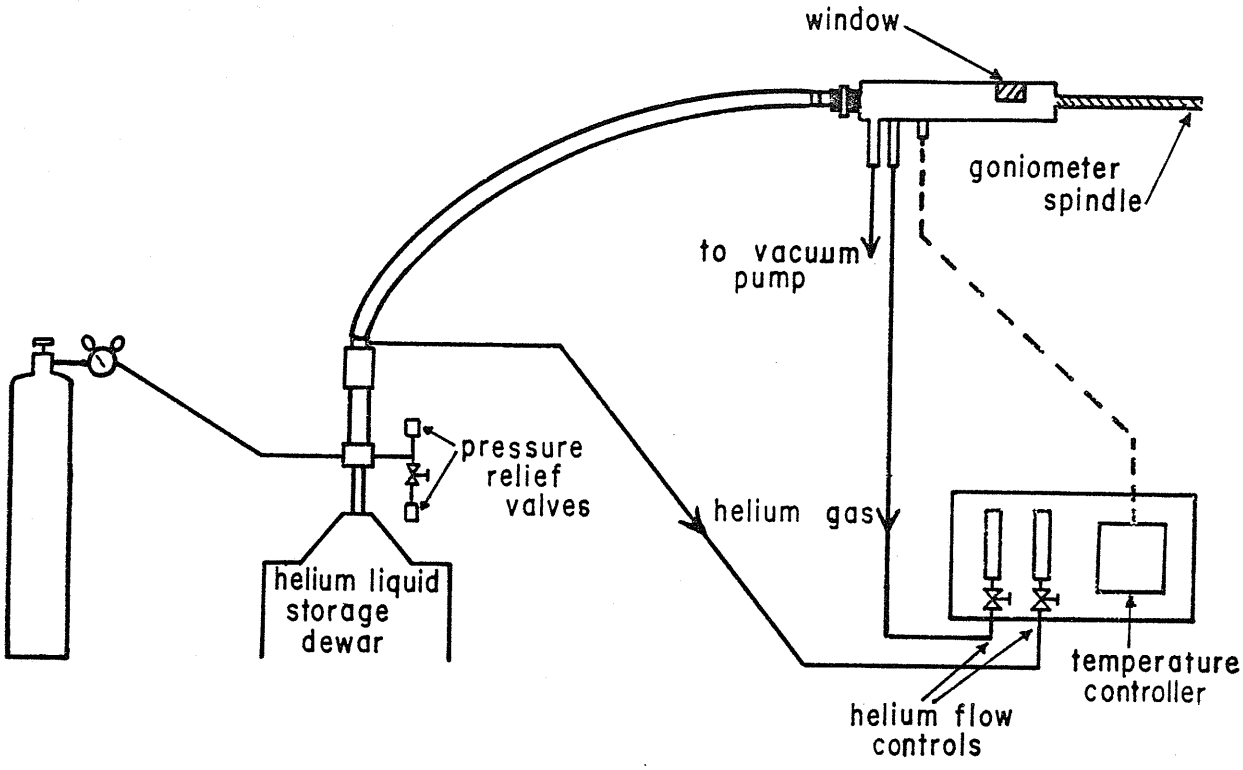

FIGURE 2-1: A diagram of the low temperature X-ray equipment.

The vacuum shroud has a Beryllium window through which the X-rays pass and is specially designed for a Phillips goniometer. The cryotip is attached to the shroud via the 'O' rings shown in Figure 2-2 and a locking pin prevents rotation of the tip with respect to the shroud. Even with the shroud evacuated however this 'O' ring seal is not sufficiently rigid to prevent movement of the axis of rotation of the sample as the goniometer rotates the shroud. An adjustable clamp had to be designed which allows the cryotip to rotate with the goniometer but which does not allow the axis of rotation to change once it has been

adjusted to coincide with that of the shroud. If these axes are misaligned, the diffraction lines are broadened and their shape is severely distorted.

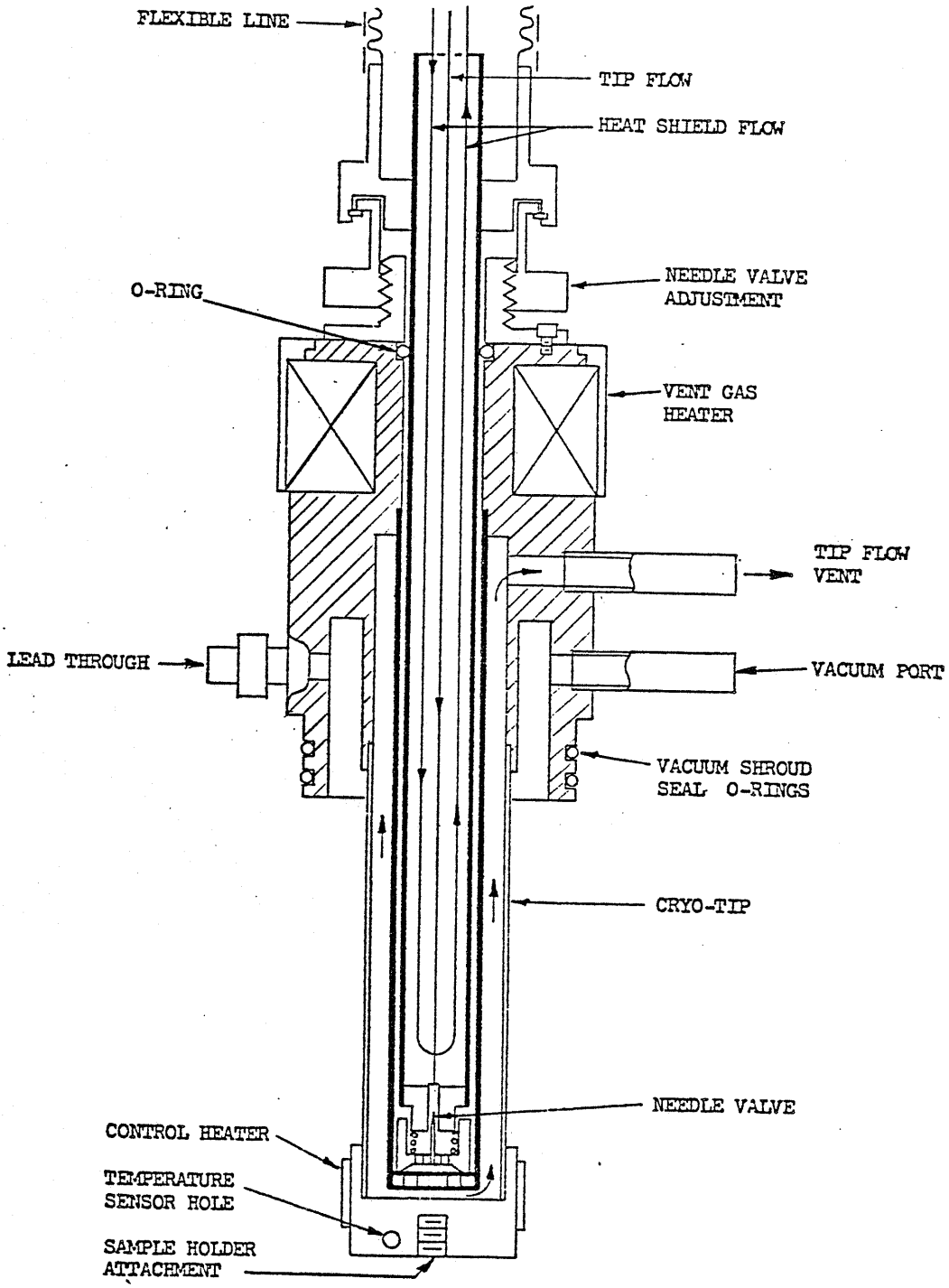

FIGURE 2-2: The low temperature X-ray diffractometer attachment.

Once the equipment is aligned at room temperature, operation is both convenient and efficient. Initial cool down to liquid helium takes approximately twenty minutes and uses very little coolant in comparison with a conventional dewar system. Helium consumption is approximately 3/4 litres/hour at 4.2 K but is much less at higher temperatures when the flow rate may be reduced. Temperature control is equally good using liquid nitrogen for temperatures above 77 K although flow rates are much higher.

2. Magnetization Measurements

All the magnetization results were taken using a vibrating sample magnetometer which has been described elsewhere.[4] Magnetic fields to a maximum of 18 kOe could be applied using a water cooled electromagnet. When used as a null detector in conjunction with a five digit potential divider, the equipment is capable of detecting susceptibility charges of 5×10^{-9} emu or $\sim 10^{-4}$ emu/Oe.[4] Changes of this magnitude are however comparable to the background noise and so for good reproducibility 10^{-3} emu/Oe is a more realistic figure. A recent improvement has been to make the horizontal sample position controls independent of vertical adjustments. This has greatly reduced the time required to position samples in the centre of the pick-up coils.

A flow through liquid-helium cryostat provides a temperature range of 2 K to 300 K and a stability of ±0.5 K by balancing heat input against gas flow. Above room temperature a vacuum furnace provides a temperature stability of ±2 K up to a specified maximum of 1050 K. The furnace requires continuous pumping during operation and also causes rather a large negative background. This should be taken into account when measuring samples which give small signals such as antiferromagnets or paramagnets. The origin of this background could be either the aluminium sample holder and its boron nitride support, or vibrations of the furnace itself caused by the pumping line.

The equipment is calibrated using spectroscopically pure nickel. Values for the calibration constant, obtained by different people over a number of years, have been within 1% of the mean.[4]

3. Mössbauer Effect Measurements

3.1 Spectrometers and Ancillary Equipment

A schematic layout of one of the Mössbauer spectrometers is shown in Figure 2-3. Vibrations of the transducer Doppler shift the energy of the gamma rays leaving the source. These pass through an absorber, which may be mounted in a furnace or cryostat, to the detector where they produce voltage pulses proportional to their energies. After amplification, a single channel analyser is used to reject all but the Mössbauer gamma rays.

All the Mössbauer measurements described later were taken with the system operating in the constant-acceleration mode.[5] The source scans a predetermined range of velocities, from negative to positive, and counts obtained at different velocities are stored in different channels of a multi-channel analyser. Clock pulses, provided by either the multichannel analyser, or in the newer systems by the transducer drive unit itself, synchronize the source velocity and the memory channel advance rate. The contents of the memory are shown continuously on a cathode ray tube and can be read out onto printed or punched tape, or plotted on an X-Y recorder. The punched tape is converted to cards using a UNIVAC DCT 1000 data communications terminal with a UNIVAC 1710 card punch.

The sources of ^{57}Co nuclei diffused substitutionally into a Chromium host were purchased from the New England Nuclear Corporation. Chromium is body-centred cubic and

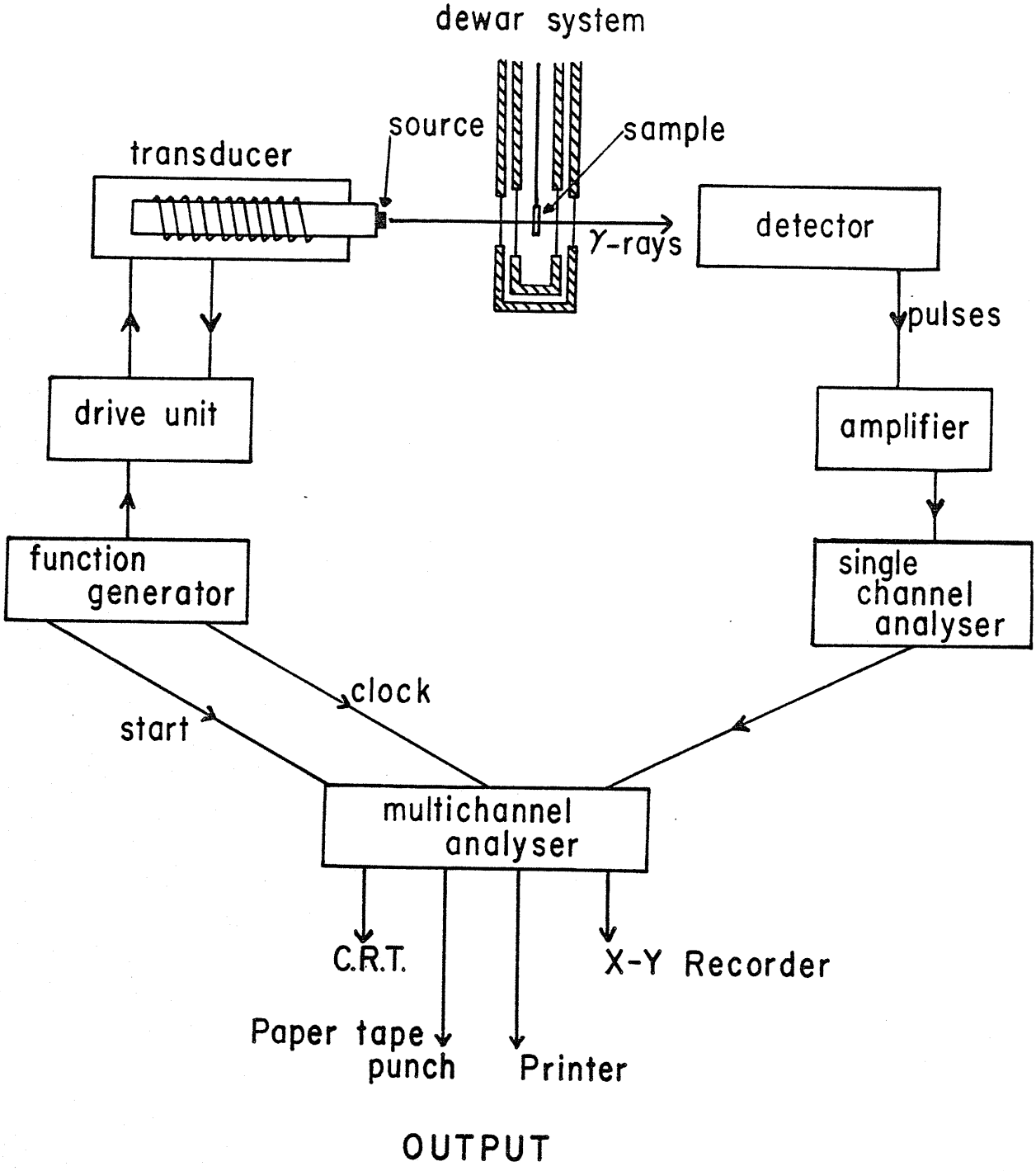

FIGURE 2-3: A schematic layout of a Mössbauer spectrometer.

produces no electric field gradient or magnetic field at the ^{57}Co nucleus. Data for this thesis were collected using sources initially 25-65 mC of ^{57}Co, attached to an aluminium holder with epoxy cement to prevent vibrations. Their activity decreases exponentially with time, with a half-life of 270 days.

Both scintillation and proportional counters were used as detectors. The NaI(Tl) scintillation counters are manufactured by Horshaw N.V. They can handle high count rates and are insensitive to the high energy γ-rays from the 122 keV, $5/2 \rightarrow 3/2$ transition. However these detectors contain photomultiplier systems and are therefore extremely sensitive to stray magnetic fields. When recording measurements involving externally applied magnetic fields, proportional counters must be used. These are of two types, Argon-methane and Xenon-methane. Both are field independent but their efficiency decays with time. The Xenon type are much more efficient in the 14.4 keV region, but are also sensitive to the 122 keV gamma rays. Great care must be taken when using the latter in order to prevent saturation of the counting system by the high energy counts.

Another problem which frequently arises is in the setting of the discrimination window of the single channel analyser to accept only the Mössbauer gamma ray. Frequently the 6.5 keV iron X-ray counts make the isolation of the 14.4 keV gamma rays quite difficult. The number of X-rays

can be substantially reduced by inserting a few millimetres of perspex between the source and the detector.

The superconducting solenoid (Figure 2-4), producing magnetic fields of up to 50 kOe has been described elsewhere.[6, 7]

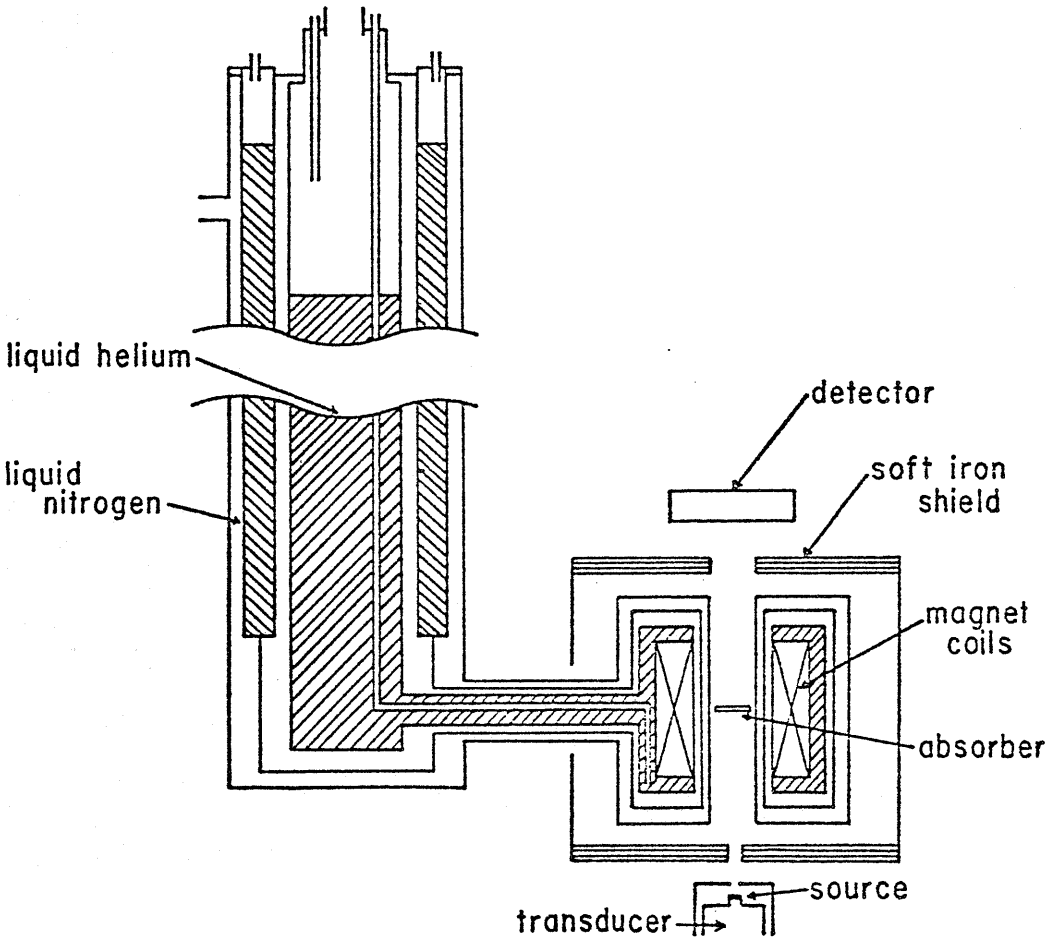

FIGURE 2-4: A schematic diagram of the superconducting solenoid.

The magnet shielding is designed to reduce fringing fields to below 100 Oe. Extra protection for the transducer is provided by a mumetal shield manufactured by the Perfection

Mica company, but despite this shielding, at fields above 30 kOe the calibration constant of the system is changed significantly[8] although the linearity remains acceptable. This necessitates recalibration of the spectrometer at each field. It is possible to record spectra from absorbers at low temperatures by placing the absorber inside the magnet, with vacuum windows placed across the ends of the bore. The sample is positioned in contact with the liquid nitrogen or liquid helium bores in order to obtain absorber temperatures of 77 K and approximately 7 K respectively. Apart from only being able to produce the two temperatures, this method is most inconvenient since the field must be removed and the solenoid warmed to room temperature to change the sample.

A custom designed liquid helium dewar has now been purchased which may be inserted into the bore of the solenoid. Together with a high field vacuum furnace described elsewhere,[8] this permits Mössbauer spectra to be recorded at temperatures from 4.2 K to 700 K in applied fields of up to 50 kOe with a temperature stability better than ±0.1 K. Other equipment provides higher and lower temperatures, but is not designed for operation with the solenoid.

3.2 Cryogenic Equipment

Due to the physical and magnetic properties of the compounds studied, all the Mössbauer spectra for this

thesis were recorded from absorbers at or below room temperature. The majority of these measurements were taken using a cryostat which was custom built by the Oxford Instrument Company. A thorough description of its design and operation will be found in reference 4. The cryostat is very efficient, with a liquid helium consumption rate of less than 0.25 l/hour and extremely convenient to use. Samples may be changed in a few minutes even when operating at 4.2 K and a stability of ±0.1 K is easily attainable over a temperature range of < 2 K to 300 K. Temperatures below 35 K are measured with a germanium resistance thermometer mounted in the sample block, and above 35 K with a Au -0.3 at.% Fe/Chromel thermocouple.

The Oxford cryostat was designed for efficiency and convenience over a large temperature range. It was not designed for use with externally applied fields. For this purpose a vertical dewar system was required, capable of being inserted into the bore of the superconducting solenoid. The cryostat shown in Figure 2-5 was designed and built by Thor Cryogenics Ltd.

The sample chamber is shielded by a gold-plated copper radiation shield inside an outer stainless steel vacuum tube designed to fit into the room temperature bore of the solenoid. The cryogen storage dewars are offset to allow gamma rays to pass through the sample. The main cryostat is a stainless steel, liquid nitrogen shielded, dewar.

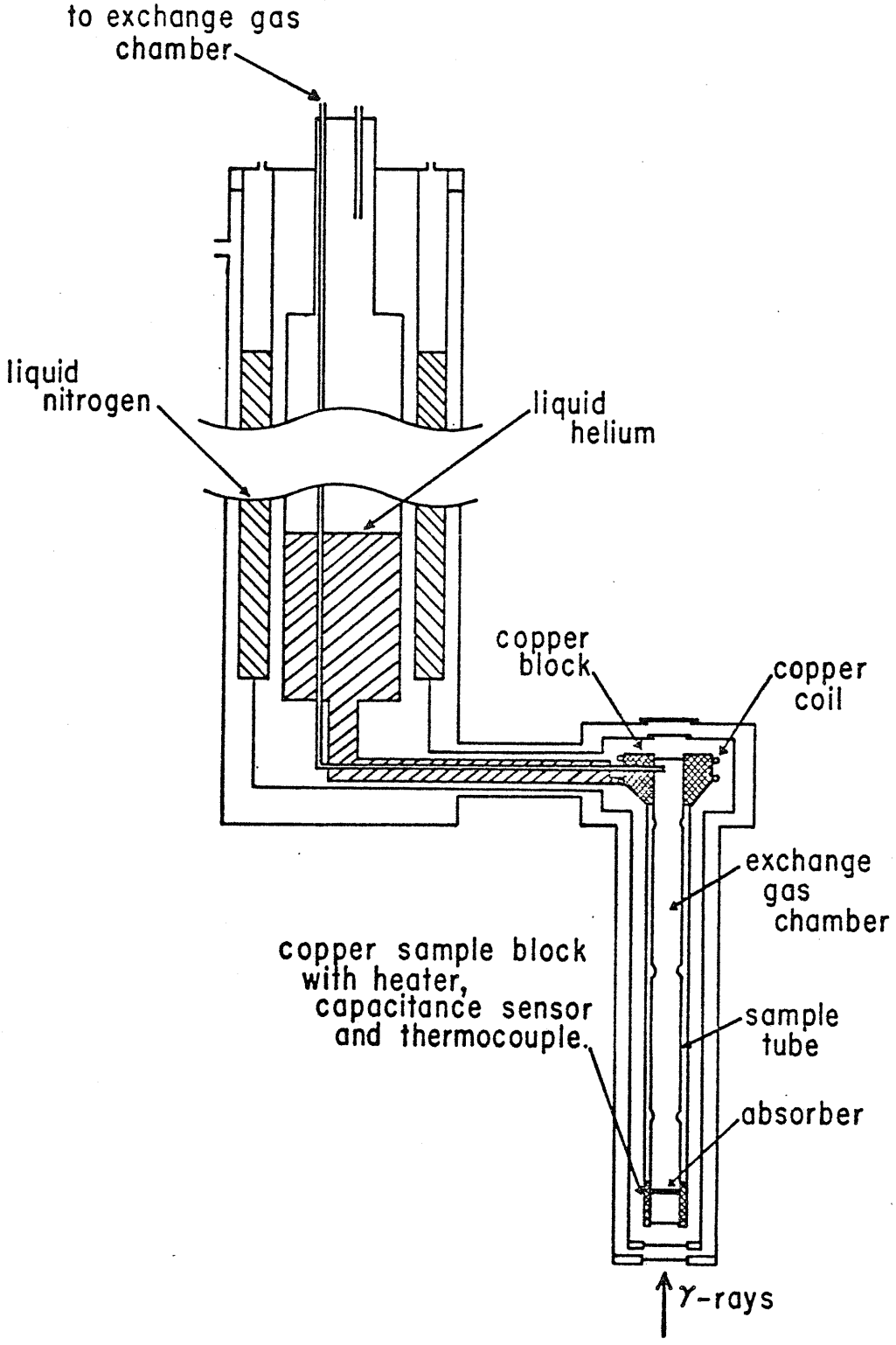

FIGURE 2-5: A diagram of the insert dewar for experiments with applied magnetic fields.

Radiation shielding, for the sample chamber in the foot dewar and the horizontal liquid helium feed through tube, is attached to the main liquid nitrogen reservoir. The sample chamber consists essentially of a stainless steel tube closed at both ends with beryllium windows. The copper block at the lower end of the chamber is fitted with an electrical heater, a Au -0.07 at. % Fe/Chromel thermocouple and a capacitance sensor. The bore of this block is machined to accept a copper sample mount containing the absorber clamped between beryllium discs. The upper copper block is cooled via the horizontal helium feed through tube, and the exchange gas pressure in the sample chamber, balanced against heat input, determines the sample temperature.

Heat input is controlled during high field measurements by a Lakeshore Cryogenic Capacitance Controller connected to the capacitance sensor in the sample block.[9] A capacitance against temperature curve is plotted in Figure 2-6. The magnetic field temperature error is $\pm$ 1 mK in a field of 150 kOe [10] and its useful range is $<$ 10 mK to 60 K, 70 K to 400 K, due to the peak between 60 K and 70 K. In this range, temperature control is better than 0.1 K over long periods.

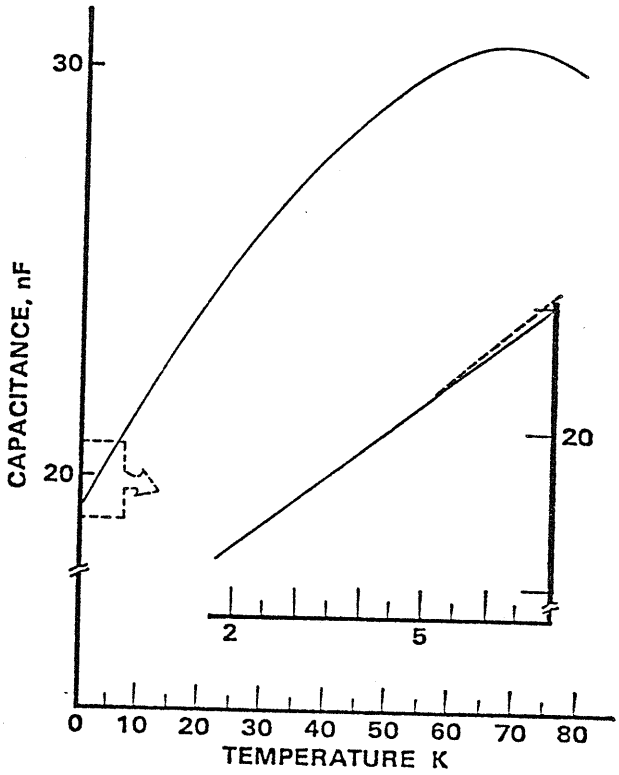

FIGURE 2-6: A typical capacitance versus temperature calibration curve.

The specified sensitivity of the controller and sensor is ± 2 millikelvin and so the system may be used as a precision thermometer. By adjusting the set point capacitance until the error signal is zero, the sensor capacitance can be read in nanofarads from the front panel controls. Reference to a sensor capacitance versus temperature calibration curve yields the temperature. If it is necessary to control at temperatures between 60 K and 70 K, the Harwell temperature controller currently used with the Oxford cryostat [4] may be connected to the heater and the Au -0.07 % Fe/Chromel thermocouple mounted in the heater block. Due to field effects on the thermo-

couple, it must be calibrated against the capacitance sensor for different fields.

The helium storage dewar is equipped with a helium level detector and holds 6.5 litres of liquid. This will last for 24 hrs even when measuring at 100 K, provided reasonable care is exercised when selecting the exchange gas pressure.

Use of the insert dewar increases the distance and reduces the solid angle between source and detector, both of which tend to reduce the number of gamma rays reaching the detector. Since liquid helium is also being supplied to the superconducting magnet, field experiments are very expensive unless strong sources are used.

3.3 Data Analysis

The spectrometers must be calibrated at regular intervals even when the velocity scale of the transducer is not changed, so as to provide accurate values for the calibration constant in mm/s/channel and for the position of the zero velocity channel. Iron Foil and αFe_2O_3 were used to calibrate the equipment taking their hyperfine fields to be 330 and 517 kOe and the splitting of the outer lines to be 10.657 and 16.70 mm/s respectively.[11]

The zero velocity channel is found by subtracting the isomer shift of the absorber with respect to chromium (.152 and .512 mm/s respectively) from the position of the centre of the spectrum. Peak positions in channel numbers can

then be converted to energies in mm/s. Table 2-1 shows the isomer shifts of Iron and αFe_2O_3 with respect to other common source hosts. It can be used to compare data from laboratories using ^{57}Co diffused into materials other than Chromium.

Absorber	Source Host					
	Chrom-ium	Stain-less Steel	Iron	Pallad-ium	Copper	Platinum
Fe	0.152	0.092	0	-0.185	-0.226	-0.347
αFe_2O_3	0.512	0.452	0.36	0.175	0.134	0.013

TABLE 2-1: The isomer shifts (in mm/s of) Fe and Fe_2O_3 with respect to various source hosts.

Theoretically, as noted earlier, a Mössbauer absorption peak will have a Lorentzian line shape with a full width at half maximum which is the sum of the natural linewidths of source and absorber. This peak will be superimposed upon a baseline which will be parabolic for the constant-acceleration spectra recorded in this thesis.[12] The transducer, a freely moving cylindrical coil mounted in the field of a permanent magnet, is driven by a saw-tooth voltage. The velocity waveform of the coil is shown in Figure 2-7.

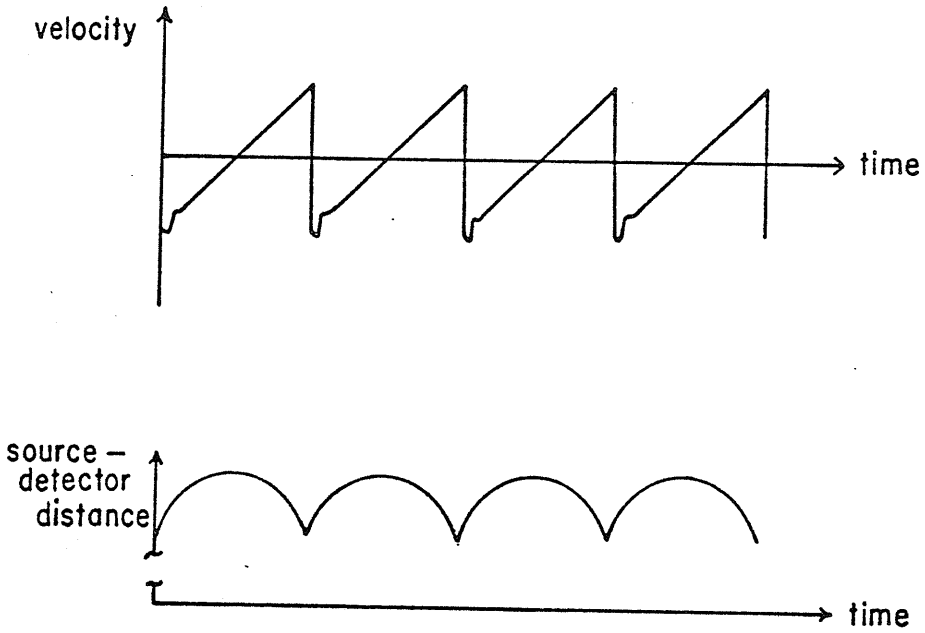

FIGURE 2-7: The velocity and position of the Mössbauer source as a function of time.

The source is closest to the absorber when moving at its maximum positive or negative velocity hence a parabolic baseline results. The shape of the baseline is given by:

$$b(x) = c_1(x-xo) + c_2(x-xo)^2$$

where x is in channel numbers and xo is the zero velocity channel. c_1 should be zero for a constant acceleration spectrum i.e. no linear slope.

The absorption spectrum then has the form

$$n(x) = b(x)\ n(o) \left(1 - \sum_{i=1}^{N} \left\{ a_i / \left[\left(2(x-x_i)/\Gamma_i \right)^2 + 1 \right] \right\} \right)$$

where n(o) is the number of counts in the background. N is the total number of peaks and x_i, a_i, and Γ_i are the position, fractional absorption, and full width at half maximum of the i th peak.

The various programs available in the laboratory perform a least-squares fit of this equation to the data. They differ in the manner in which constraints on the various parameters are applied. The programs also calculate a goodness of fit parameter called chi squared (χ^2) defined as:

$$\chi^2 = \sum_{i=1}^{N_p} \frac{\left[n_{obs}(x_i) - n_{calc}(x_i)\right]^2}{n_{calc}(x_i)}$$

where N_p is the total number of data points. A chi squared value of N_p indicates a perfect fit within statistical error.

REFERENCES - CHAPTER II

1. C. Boumford and A.H. Morrish, Phys. Stat. Sol. (a) 22, 435 (1974).
2. M.J. Buerger, The Precession Method, John Wiley and Sons, New York (1964).
3. E.W. Nuffield, X-Ray Diffraction Methods, John Wiley and Sons, New York (1966).
4. M.R. Spender, Ph.D. Thesis, University of Manitoba (1973).
5. G.K. Wetheim., Mössbauer Effect: Principles and Applications, Academic Press, New York (1964).
6. L.K. Leung, Ph.D. Thesis, University of Manitoba (1972).
7. M.R. Spender and A.H. Morrish, Can. J. Phys., 50, 1125 (1972).
8. J.M.D. Coey, Ph.D. Thesis, University of Manitoba (1971).
9. W.N. Lawless, Rev. Sci. Inst., 42, 561 (1971).
10. L.J. Neuringer and L.G. Rubin, Fifth Temperature Symposium, Washington D.C. (1972).
11. Mössbauer Effect Data Index, 1958-1965, John Wiley, New York (1966).
12. N.N. Greenwood and T.C. Gibb, Mössbauer Spectroscopy, Chapman and Hall Ltd., London (1971).

CHAPTER III

IRON SELENIDE Fe_7Se_8

1. Introduction

The crystallographic and magnetic structures of the series of iron selenide compounds $FeSe_x$ ($1 \leqslant x \leqslant 1.35$) have generated a great deal of interest in recent years.[1 - 7] This has been due in part to their close relationship to the iron sulphide system. Properties of iron sulphides are of particular importance in the treatment of sulphide ores. In addition, the possibility of extracting geomagnetic data from these naturally occurring minerals requires a detailed knowledge of their magnetic structures. The need for this knowledge is evident in the case of pyrrhotite Fe_7S_8 which has been found reversely magnetized in nature with some form of self-reversing mechanism being the most likely explanation.[8, 9]

The many phases and superstructures of these two systems make detailed analysis of their crystallographic and magnetic structures extremely complex. A sizeable amount of the work on Fe_7Se_8 was concerned with sample preparation and crystal structure analysis, to ensure that all powder samples were single phase material with the required crystallographic superstructure.

1.1 Crystal Structure

Fe_7Se_8 crystallizes with the NiAs structure. In this structure, the anions form a hexagonal-close-packed array, i.e. repeating every two layers, with octahedral and tetrahedral interstices. Only the octahedral sites are occupied by cations; the tetrahedral sites remain vacant. The cation sites are arranged in layers in a simple hexagonal lattice, (Figure 3-1a), with each site having six nearest-neighbour anions in cubic symmetry as indicated in Figure 3-1b.

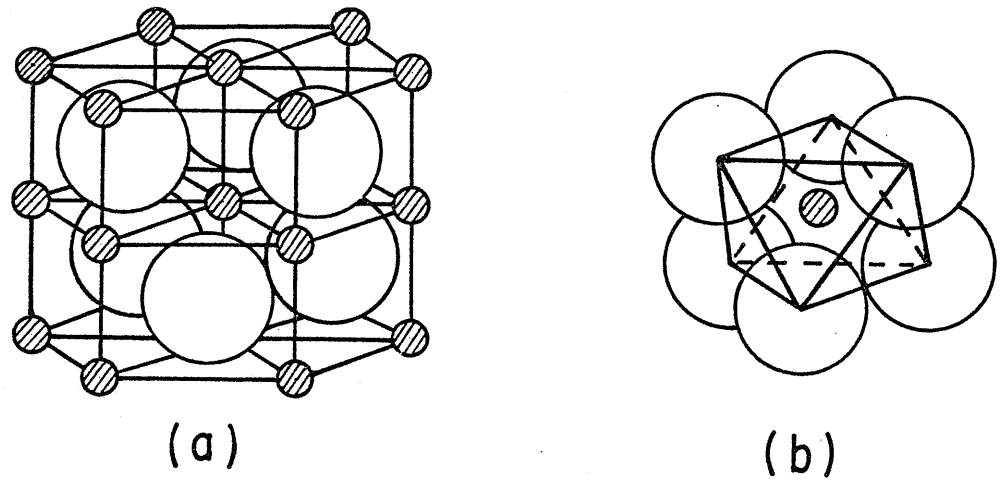

FIGURE 3-1: a) The NiAs structure b) An octahedral site. Small circles represent anions and large circles represent cations.

The octahedral sites are equal in number to the anion ions and so the iron deficiency in Fe_7Se_8 leads to vacancies in the cation lattice. These vacancies are not randomly

distributed in the iron lattice but are ordered on alternate planes, the stacking sequence forming well defined superstructures.[2] Since at least two superstructures are stable at room temperature, crystallographic and magnetic properties of Fe_7Se_8 samples are very sensitive to their thermal history.

Figure 3-2 shows the two superstructures with the selenium atoms omitted for clarity.

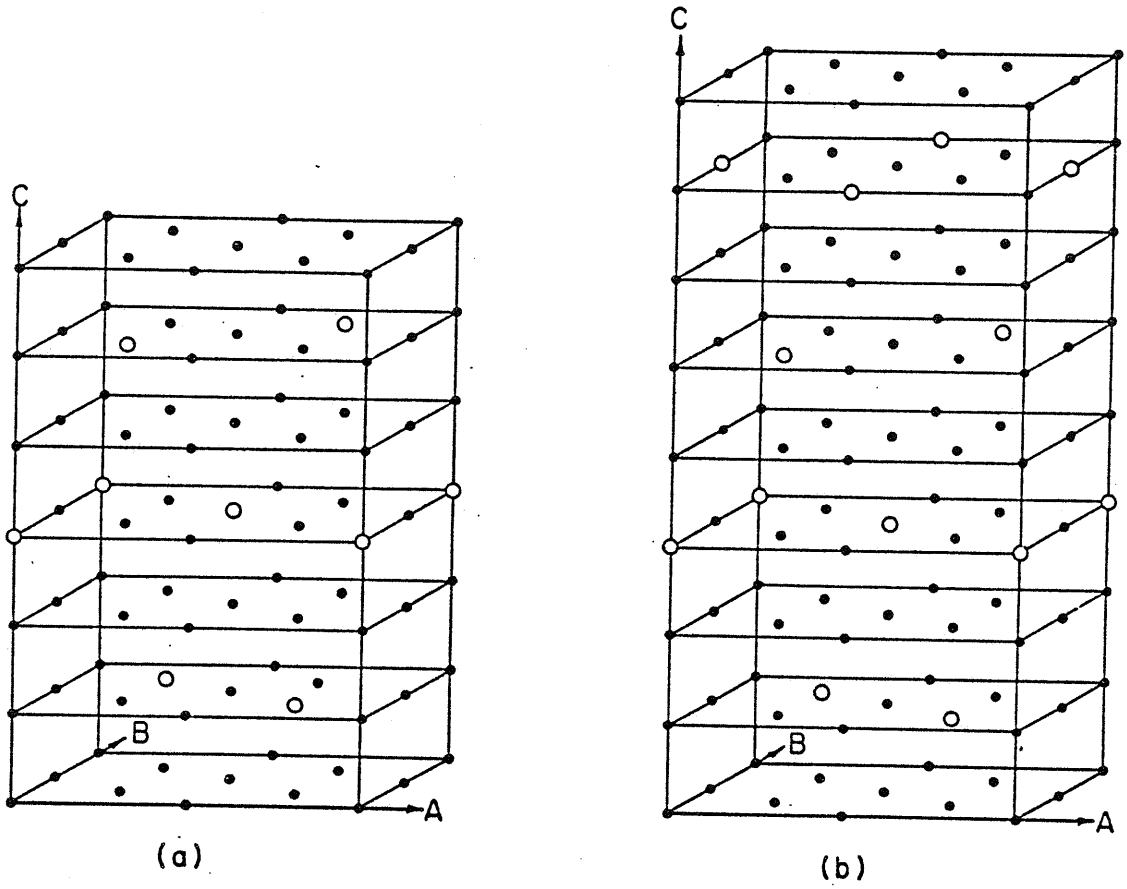

FIGURE 3-2: Unit cells with a) The 3c superstructure and b) the 4c superstructure of Fe_7Se_8. Selenium atoms omitted for clarity.

They differ in repeat distance along the c-direction. A unit cell of the 3c superstructure contains six molecules of Fe_7Se_8 and, neglecting the vacancies, retains the basic hexagonal symmetry. The 4c structure contains eight molecules

and has been reported to have a slight triclinic distortion.[2]

1.2 Magnetic Structure

The magnetic moments of iron ions in the same c-layer align parallel to one another whereas moments in adjacent c-planes are antiparallel. The deficiency of iron ions in alternate layers results in a net spontaneous moment below the ordering temperature and hence Fe_7Se_8 is ferrimagnetic.

Hirakawa[3] investigated the magnetic properties of a sample of the 4c structure using a torque magnetometer. He found that the ferrimagnetic Néel point (T_{FN}) was 443 K and that the direction of easy magnetization lay in the c-plane at room temperature. On lowering the temperature below 220 K however, the easy direction gradually rotated out of the c-plane to make an angle of $\sim 20^{o}$ with the c-axis at 4.2 K.

A similar effect was noted by Andresen and Leciejewiez[4] in powder samples of the 3c structure. Their neutron diffraction study gave an angle of 18^{o} between the spin direction and the c-axis at 4.2 K but indicated that the rotation from the c-plane took place in a narrow temperature range between 120 K and 130 K. Neutron diffraction data from a later study[6] of single crystal samples agree with Hirakawa's results for the 4c structure, but suggest that an abrupt rotation of 90^{o} takes place at 130 K in crystals with the 3c structure. The direction of the spontaneous

moment lies in the c-plane above this temperature and parallel to the c-axis below.

The saturation magnetization of a 4c sample was measured by Hirakawa[3] and found to be 70 G/cm^3. (extrapolated to absolute zero). A net moment of $2\mu_B$/molecule would give a saturation magnetization of 69 G/cm^3 which lead Hirakawa to predict the ionic model $\left[Fe_4^{2+}\right]\left[Fe_2^{3+}\ Fe^{2+}\ \square\ \right]\ Se_8^{2-}$ for the magnetic structure, where $\square$ represents an ion vacancy and the brackets indicate successive c-planes.

2. Sample Preparation

Samples were prepared by heating iron and selenium in an evacuated quartz ampule. The quartz tubes were thoroughly cleaned and first heated to close to their melting point (above 1000 C) while attached to a vacuum pump, in an attempt to remove absorbed gases from the inside walls. Both the iron and selenium were 99.999% pure and the iron powder was reduced before use by heating in a stream of hydrogen gas. When the ampules were to be subjected to a high temperature for long periods, care had to be taken to remove all grease from the outer surfaces since this slowly attacked the quartz, occasionally causing the ampules to crack.

The melting point of Fe_7Se_8 was found to be $\sim$1050 C. This, together with the phase diagram of the 4c and 3c superstructures[5] shown in Figure 3-3 determined the heat treatment given to the samples.

Stoichiometric quantities of selenium and freshly reduced iron powder were sealed in an evacuated quartz ampule and heated to 1150 °C. At this temperature the selenium was present as a dark brown vapor in the tube. The vapor disappeared after 3 days, at which time the furnace was switched off and allowed to cool to room temperature. The product was a shiny black polycrystalline solid, which was ground to a fine powder, pressed into a pellet and resealed in an evacuated ampule. The pellet was fired at 1050°C for 3 days then cooled to 350°C, where it

was annealed for 1 week. From Figure 3-3, quenching then produces the 3c superstructure or samples of the 4c structure can be formed by cooling to room temperature at 10°C/hour.

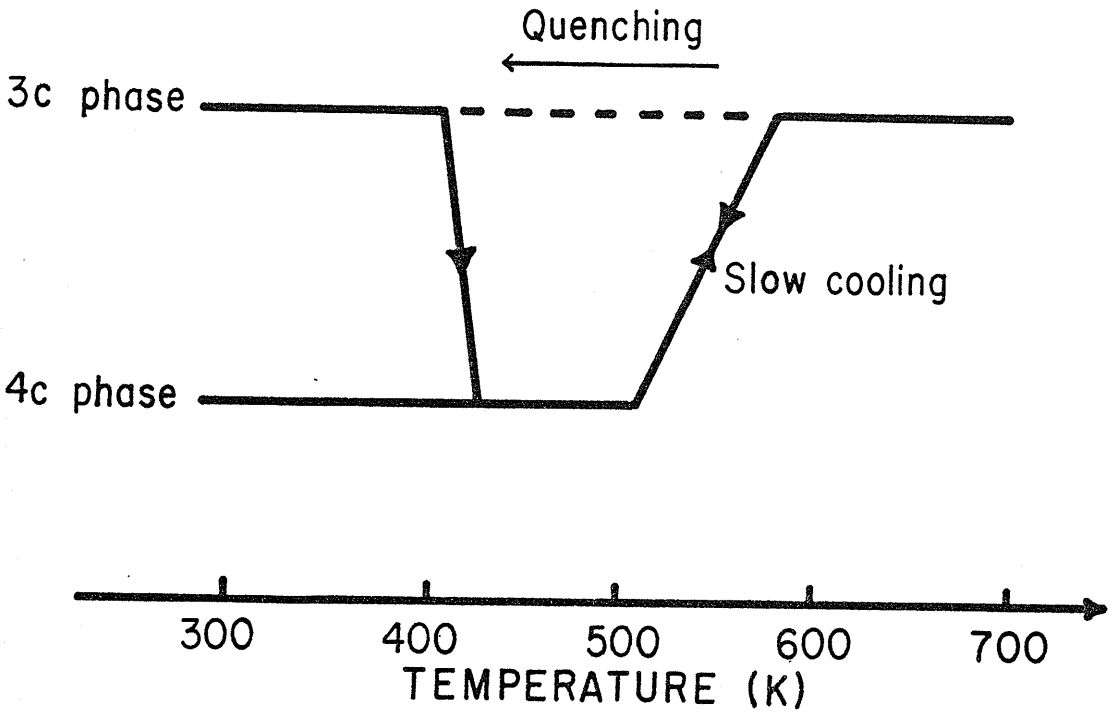

FIGURE 3-3: The phase diagram of the 3c and 4c superstructures.

The samples thus produced were ground to a fine powder and Debye-Scherrer X-ray photographs were taken of both types. The high angle lines of these photographs were slightly diffuse but all lines could be indexed using the lattice parameters reported by Okazaki, although it was not possible to distinguish between the two superstructures. Reannealing at 600°C for 1 week and either quenching or slow cooling from 350°C seemed to produce a slight improvement

in the sharpness of the X-ray lines, but it was still not possible to distinguish between the 3c and 4c structures.

Since original characterization of the 3c and 4c superstructures had been performed using single crystal X-ray techniques [1, 2] an attempt was made to grow single crystals of the two structures.

The reground material from the initial firing at 1150°C was sealed in a quartz ampule. This was placed in the furnace in a position such that a temperature gradient existed across the sample. Single crystals of the 4c structure were produced by annealing at 1050°C for 3 days and cooling to room temperature at about 10°C/hour, annealing for 12 hours at 100 degree intervals. Crystals of the 3c type were produced by quenching the 4c samples from 400°C.

3. Single Crystal X-Ray Analysis

Laue photographs of the crystals frequently showed splitting of the diffraction spots.

The splitting was always present in the 4c crystals but this could be caused by the slight triclinic distortion reported by Okazaki. From the Laue photographs, standard techniques were used to align the crystal with the [001] direction parallel to the axis of rotation of the goniometer. The goniometer head was then transferred to the rotation camera and examples of results for both superstructures are shown in Figure 3-4. The superlattice reflections are clearly visible and can be seen to divide the spacing of the layer lines into three or four for the 3c or 4c structure respectively. Photographs from rotations around the B-axis produced superlattice reflections which split the layer lines into two for both structures.

The cell dimensions measured from the separation of the layer lines are shown in Table 3-1. Small letters denote the fundamental NiAs cell.

Superstructure	C (Å)	B = 2a (Å)	A = $\sqrt{3}$B (Å)
3c	17.51 ± 0.05	7.24 ± 0.05	12.54 ± 0.05
4c	23.38 ± 0.05	7.22 ± 0.05	12.51 ± 0.05

TABLE 3-1: The cell dimensions of Fe_7Se_8 as measured from rotation photographs.

(a)

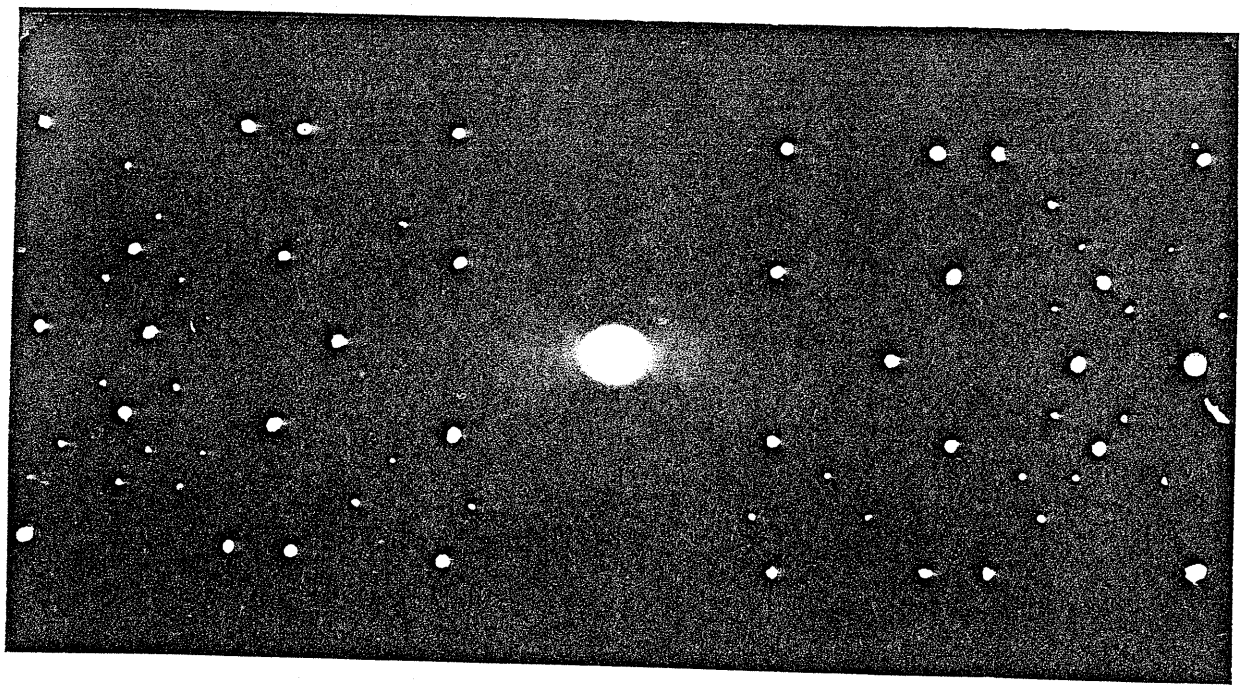

(b)

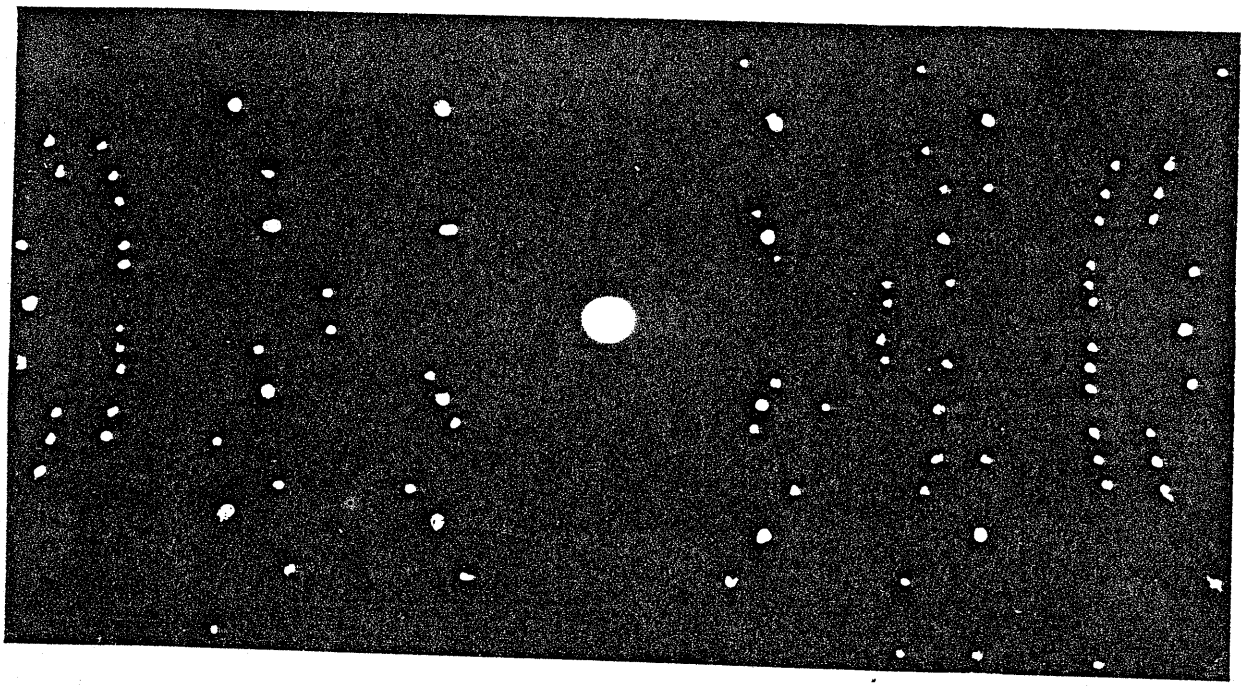

FIGURE 3-4: Rotation photographs about the c axis of a) the 3c structure and b) the 4c structure.

From the large errors it can be seen that this is not a very accurate method of measuring the lattice parameters. However the object of the exercise was to distinguish between the two superstructures, for which rotation photographs proved ideal.

A more detailed analysis of the 3c structure was undertaken using the Buerger precession method. The 3c structure was chosen since crystals with this superstructure gave consistently sharper X-ray spots using the Laue and rotation cameras. If however this was due to the slight triclinic distortion of the 4c crystals it would not have affected the precession photographs. The precession method produces a picture of a single reciprocal lattice plane i.e. planes (h k l)* and $(\bar{h}$ k l)* form different diffraction spots.

The crystal was mounted on a goniometer head which was transferred directly to the precession instrument. Initial orientation pictures were taken using unfiltered molybdenum radiation and polaroid film. The precession angle was set at 10^{o} and no layer screen was included. Standard techniques were used to align the crystal such that the b-axis was precessing about the X-ray beam and hence the a* c* plane in reflecting position. The precession angle was then set at 25^{o} and a screen inserted at the correct distance to allow only the '0' level reflections to reach the film.[10] A zero level photograph was taken using

zirconium filtered molybdenum radiation.

In order to record higher level photographs it is necessary to know the spacing of planes along the precession axis. Although this was known from previous powder data it was checked by taking a Cone Axis photograph. The motion of the screen is such that it remains perpendicular to the precession axis, thus allowing only the required set of reflections (Laue cones) through to the film. If however the screen is replaced by a film holder the different Laue cones can be recorded and hence the layer spacing determined. From this spacing a screen was chosen to allow only reflections from the '1' level of the reciprocal plane and a '1' level photograph recorded. Examples of '0' level, '1' level and cone axis photographs are shown in Figure 3-5.

If the relative positions of reflection spots on the '0' and '1' level photographs are examined, it will be seen that the true periodicity along the a* axis is half that measured from either photograph. Effects of the 3c superlattice can be seen on the '1' level photograph as faint spots forming lines parallel to the a* axis with a periodicity of one third c*.

Additional evidence for the proposed superlattice can be gained by examining the symmetry of the 3c unit cell (Figure 3-2). Looking along the B-axis it can be seen that without vacancies the symmetry would be 2 mm. With the vacancies however this is reduced to 2. Returning to the

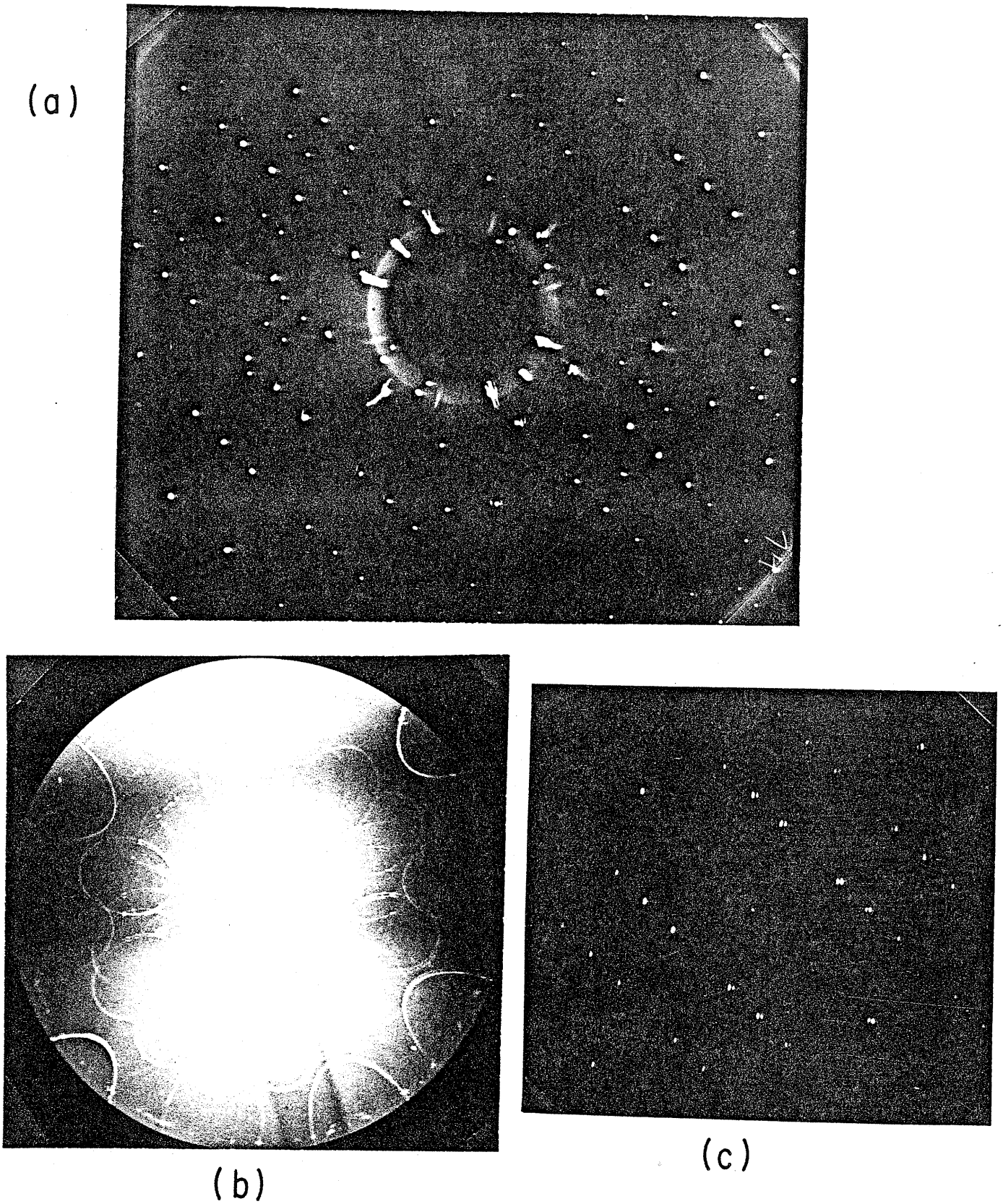

FIGURE 3-5: Examples of precession photographs of 3c-Fe_7Se_8 taken about the b axis. a) 'l' level reflections b) A cone axis photograph c) '0' level reflections. The doubling in the '0' level photograph is an instrumental effect.*

level photographs, although the symmetry appears at first to be 2mm, careful examination of the intensities suggests that the true symmetry is indeed 2.

The angle between the a* and c* axes was measured from both level photographs and was found to be $90^{o} \pm 30'$. From the level photographs, ignoring superlattice reflections,

$c^* = .122$ r.l.u. (reciprocal lattice units)

$a^* = .113$ r.l.u.

and from the cone axis photograph

$b^* = .202$ r.l.u.

Indexing on an orthorhombic cell this gives

$$c = \frac{\lambda}{c^*} = 5.83 \text{ Å}$$

$a = 6.27$ Å

$b = 3.51$ Å

This leads to superlattice cell dimensions of

$A = 2a = 12.54$ Å

$B = 2b = 7.02$ Å

$C = 3c = 17.49$ Å

Errors of less than 1% are estimated on A and C, but the error on B, measured from cone axis photographs will be much larger. This method however was not developed for accurate determination of cell dimensions. Its great advantages lie in its undistorted picture of the reciprocal

lattice. Far more accurate values for the lattice parameters can be determined using the much simpler Gandolfi camera, provided the reflections are correctly indexed.

As mentioned earlier, the Gondolfi camera is a modification of the Debye-Scherrer camera and provides 'powder' photographs of a single crystal. The Gandolfi photograph of the 3c crystal was identical to the earlier powder photographs except for the extremely sharp high angle lines. An indexed pattern for Fe_7Se_8 is given in Table 3-2. The intensities were taken from a powder diffractometer trace up to $2\theta = 140^{o}$, but above this they had to be estimated from the photograph since the diffractometer could only scan to this angle. The cell dimensions were found to be

$$A = 12.540\ \text{Å} \quad B = 7.240\ \text{Å} \quad C = 17.665\ \text{Å}$$

These are in good agreement with the Okazaki values obtained from less accurate rotation photographs.

$$A = 12.5_3\ \text{Å} \quad B = 7.23_4\ \text{Å} \quad C = 17.6_5\ \text{Å}$$

The indexing and lattice parameter determination was simplified by the use of a least squares fit computer program provided by the Crystallography Laboratory. After all lines had been indexed and initial estimates of the cell dimensions had been made, the low angle reflections were removed and the program re-run with the Miller indices of the high angle reflections fixed, to obtain the final

h k l	Intensity	d_{obs} (A)	d_{calc} (A)
0 0 6	2	2.9047	2.9442
2 0 3	2	2.7435	2.7672
2 1 0	1	2.3566	2.3698
2 0 6	10	2.1369	2.1461
3 0 0	2	2.0728	2.0900
2 2 0	7	1.8033	1.8100
3 0 6	1	1.6941	1.7043
2 0 9	8	1.6589	1.6636
2 2 6	4	1.5384	1.5419
4 0 3	6	1.5110	1.5147
0 0 12	5	1.4688	1.4721
4 0 6	5	1.3822	1.3836
2 0 12	1	1.3281	1.3325
4 0 9	4	1.2239	1.2248
4 2 3	7	1.1609	1.1616
2 2 12	7	1.1415	1.1421
2 0 15	4	1.1019	1.1024
4 2 6	6	1.0997	1.0992
6 0 0	6	1.0447	1.0450
4 2 9	8	1.0145	1.0144
6 0 6	6	0.9850	0.9849

TABLE 3-2: An indexed powder pattern from a sample of Fe_7Se_8 with the 3c superstructure.

accurate cell dimensions.

There are a number of reasons for the inherent inaccuracy of low-angle measurements. The most important in the selenide case proved to be absorption of the X-ray beam by the sample. This tends to increase the measured 2θ values at low angles. From the Bragg equation it can be seen that an error in the measurement of θ is more serious at low angles

$$\lambda = 2d \sin\theta$$

$$\frac{\Delta d}{d} = -\cot\theta \, \Delta\theta$$

An error in θ is less critical at high angles ($\theta \rightarrow 90$) where $\cot\theta \rightarrow 0$.

4. Preparation of Mössbauer Absorbers

Due to the large non-resonant absorption of the Mössbauer γ-rays by the selenium, it was necessary to enrich the Mössbauer absorbers with ^{57}Fe so that less sample could be used. Samples to be used as Mössbauer absorbers were made in the same way as the single crystals except that iron powder enriched in ^{57}Fe was used. The crystals were ground to a fine powder and mixed with boron nitride to provide a uniform sample in the form of a disc with 0.5 mg/cm^2 of ^{57}Fe. All absorbers were immediately sealed in wax to prevent oxidation.

Debye-Scherrer photographs of Mössbauer samples prepared in this manner again showed the broad high-angle lines mentioned earlier. Examples of Mössbauer spectra from such an absorber without externally applied fields are shown in Figure 3-6. It can be seen that the absorption peaks are very broad and seem to be composed of large numbers of overlapping lines.

The c/a ratio for Fe_7Se_8 was measured as 1.627 and so very little distortion from cubic symmetry is expected at the iron sites. It can therefore be assumed that the quadrupole interaction is going to be small compared to the magnetic coupling and the usual 6-line Mössbauer patterns are expected. With this assumption a superposition of at least five such patterns on a broad central doublet was required to fit the less complex 4c spectra. This indicated the

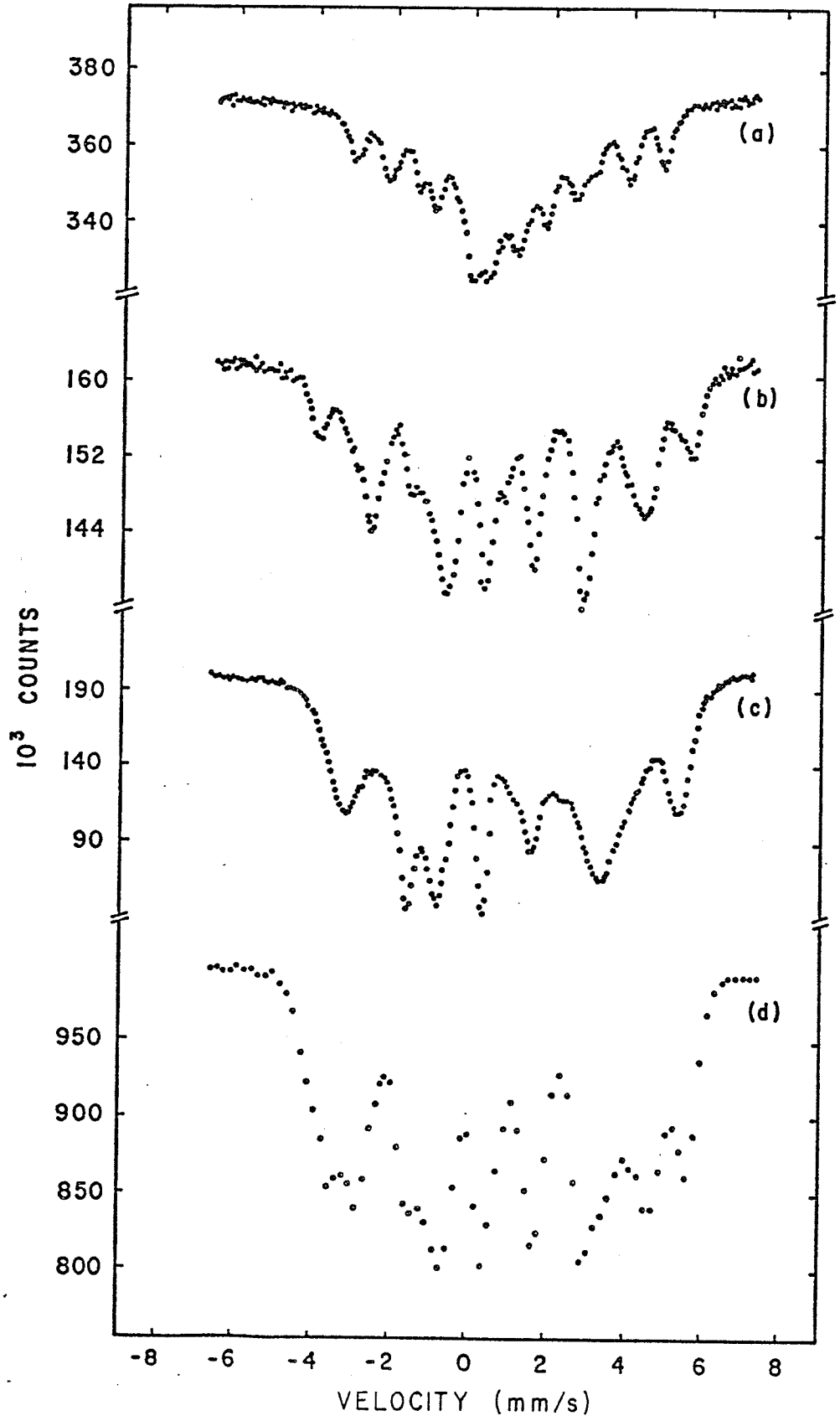

FIGURE 3-6: Examples of Mössbauer spectra recorded from 'ground' absorbers a) '4c' at 300 K b) '4c' at 77K c) '3c' at 77 K d) '4c' at 4.2 K.

presence of five or more magnetically inequivalent iron sites which was inconsistent with the superstructure proposed by Okazaki[2] and verified by the previous X-ray work.

It was also noted that one of the six-line patterns had a much smaller hyperfine field (107 kOe at 77 K) and a much larger quadrupole shift $(\Delta_{21} - \Delta_{56})/4 = -0.24$ mm/s at 77 K than the rest. A similar field had been reported by Regnard and Hocquenghem[11] for Fe_3Se_4. This observation, together with the broad high-angle lines in the Debye-Scherrer powder photographs, suggested that other phases or structures may have been introduced into the samples while grinding the crystals to a powder.

The method of preparation of Mössbauer absorbers had to be modified to eliminate any cold working following the heat treatment. After the initial firing at 1150°C the reground material was annealed for 3 days at 880°C (well below the melting point). Samples of the 4c structure were produced by slow cooling as described earlier, and 3c samples by quenching from 400°C. Debye-Scherrer photographs of the resultant black powder did not show the line broadening of the ground crystals and their Mössbauer spectra showed no trace of either the central doublet or the inner six-line pattern.

To illustrate this effect, room temperature spectra of the 3c material after various heat treatments are shown in Figure 3-7. Spectra 3-7a and b display the difference between samples without and with cold working respectively.

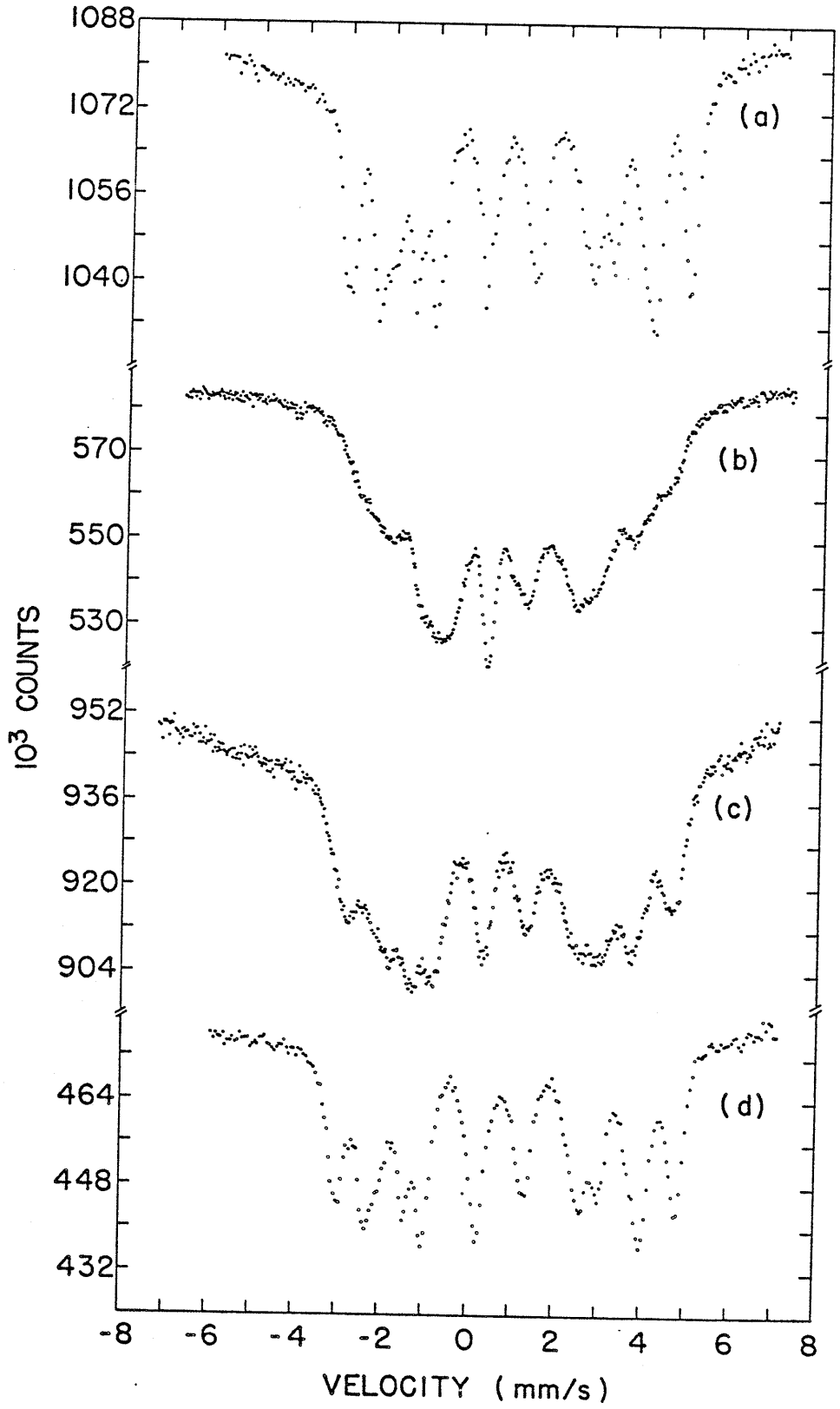

FIGURE 3-7: *Spectra obtained at room temperature from absorbers with the 3c superstructure prepared a) without grinding the final product b) by grinding the crystallites to a fine powder c) by annealing a 'ground' sample for 1 week at 600°C and d) by annealing a 'ground' sample for 3 weeks at 750°C.*

Spectra c and d illustrate the improvement in the ground samples after prolonged annealing.

Similar results were found for the 4c material, but after annealing it was progressively more difficult to produce the pure 4c phase. Traces of the 3c phase were always introduced. Care was taken to perform all further measurements on samples which had not been cold worked.

5. Magnetization Measurements

The vibrating sample magnetometer discussed in Chapter I was used to measure the magnetization of powder samples of Fe_7Se_8 at temperatures from 4.2 to 500 K. The M vs H curve shown in Figure 3-8 was recorded from a 3c sample at 4.2 K. Particles of the powder samples were examined under a microscope and appeared roughly spherical. Since shape anisotropy is therefore not expected to be large, the lack of saturation and high coercive field indicated by the above curve suggest that the material has a high crystalline anistropy.

Kamimura et al.[7] measured the magnetization along the x-axis of a single crystal of the 4c structure and described their results with a magnetocrystalline anisotropy energy of the form

$$E(\theta) = -K_0|\cos\theta| + K_3\cos^2\theta + K_4\cos^4\theta$$

where θ is the angle between the magnetic moment and the c-axis. The 3rd term was found to be small compared with the first two. At room temperature they found $K_0 = .3 \times 10^6$ ergs/cm^3 and $K_3 = 2.5 \times 10^6$ ergs/cm^3 and at 4.2 K $K_0 = 6.5 \times 10^7$ ergs/cm^3 and $K_3 = 3.5 \times 10^6$ ergs/cm^3. These values for the anisotropy constants are much greater than the corresponding values measured for pyrrhotite.[12]

The magnetization of a 4c powder sample as a function of temperature is shown in Figure 3-9. The easy direction of magnetization moves slowly from the c-plane toward the

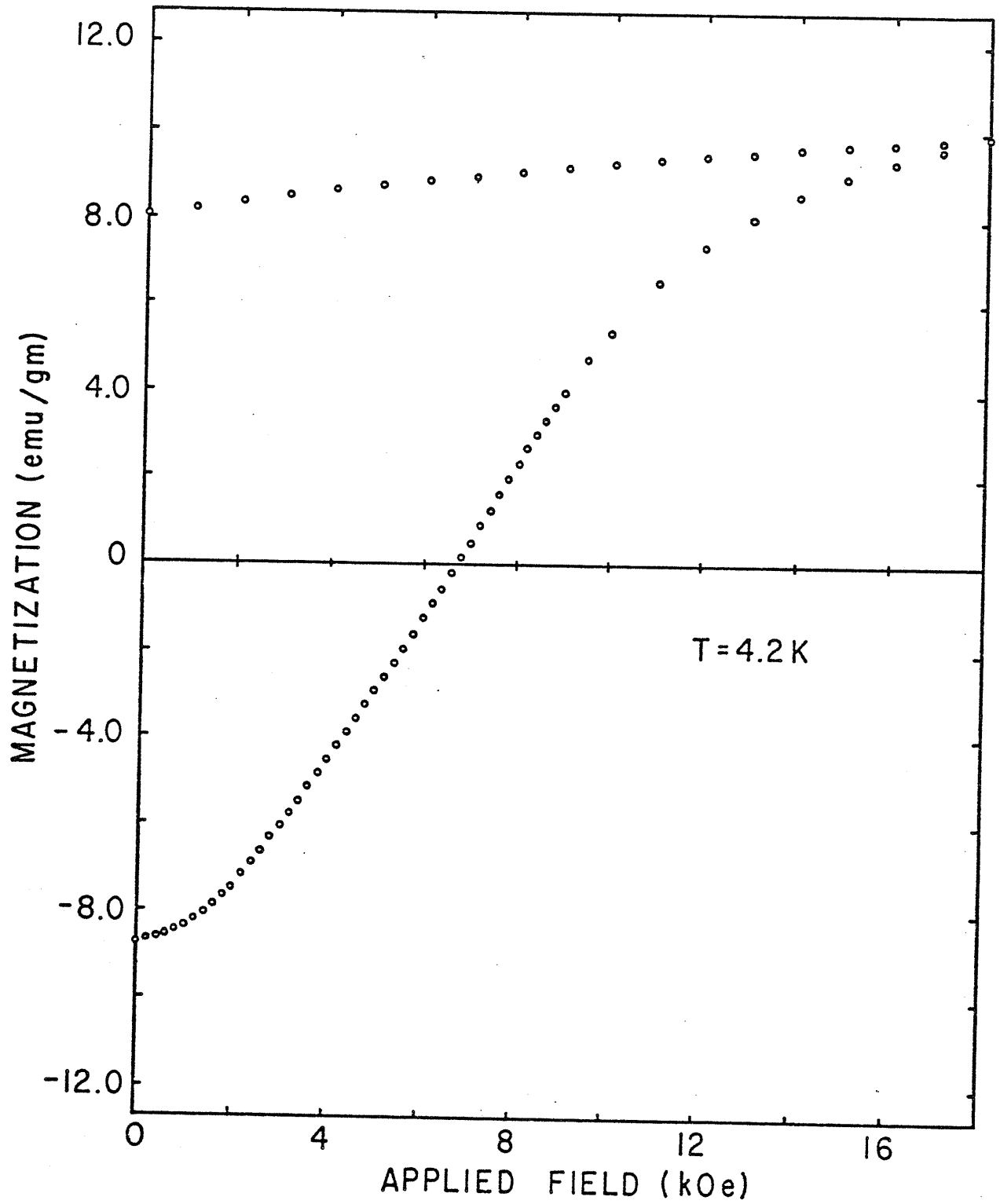

FIGURE 3-8: A plot of magnetization against applied field for a 3c sample of Fe_7Se_8 at 4.2 K.

c-axis as we lower the temperature. At room temperature the spin direction lies in the c-plane for both structures. By using a torque magnetometer, Hirakawa[3] found three easy directions of magnetization in the c-plane of a single crystal of the 4c structure, consistent with the slightly distorted hexagonal symmetry. This explains the reduction in magnetization of the randomly oriented powder samples as the temperature is lowered.

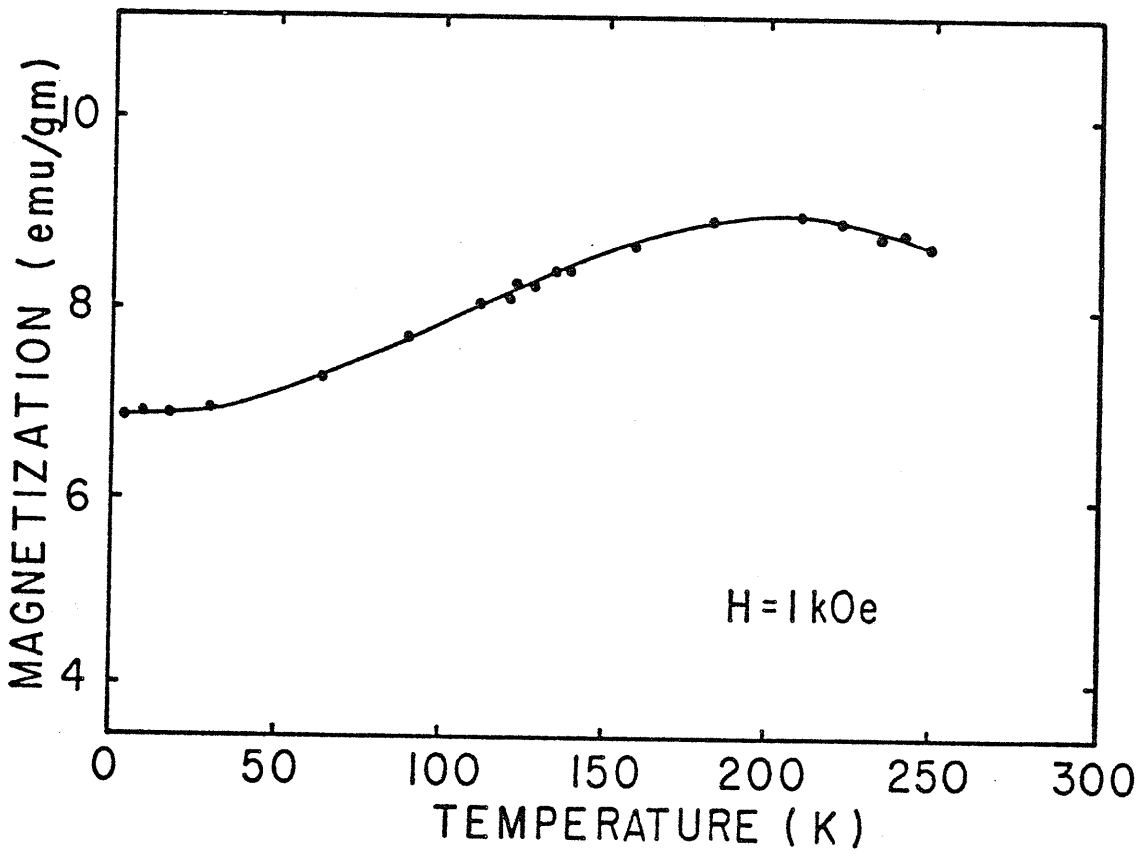

FIGURE 3-9: The magnetization as a function of temperature for a sample with the 4c superstructure in an applied field of 1 kOe.

Evidence for the abrupt spin rotation reported for the 3c structure [6] is shown in Figure 3-10. The peak occurs at

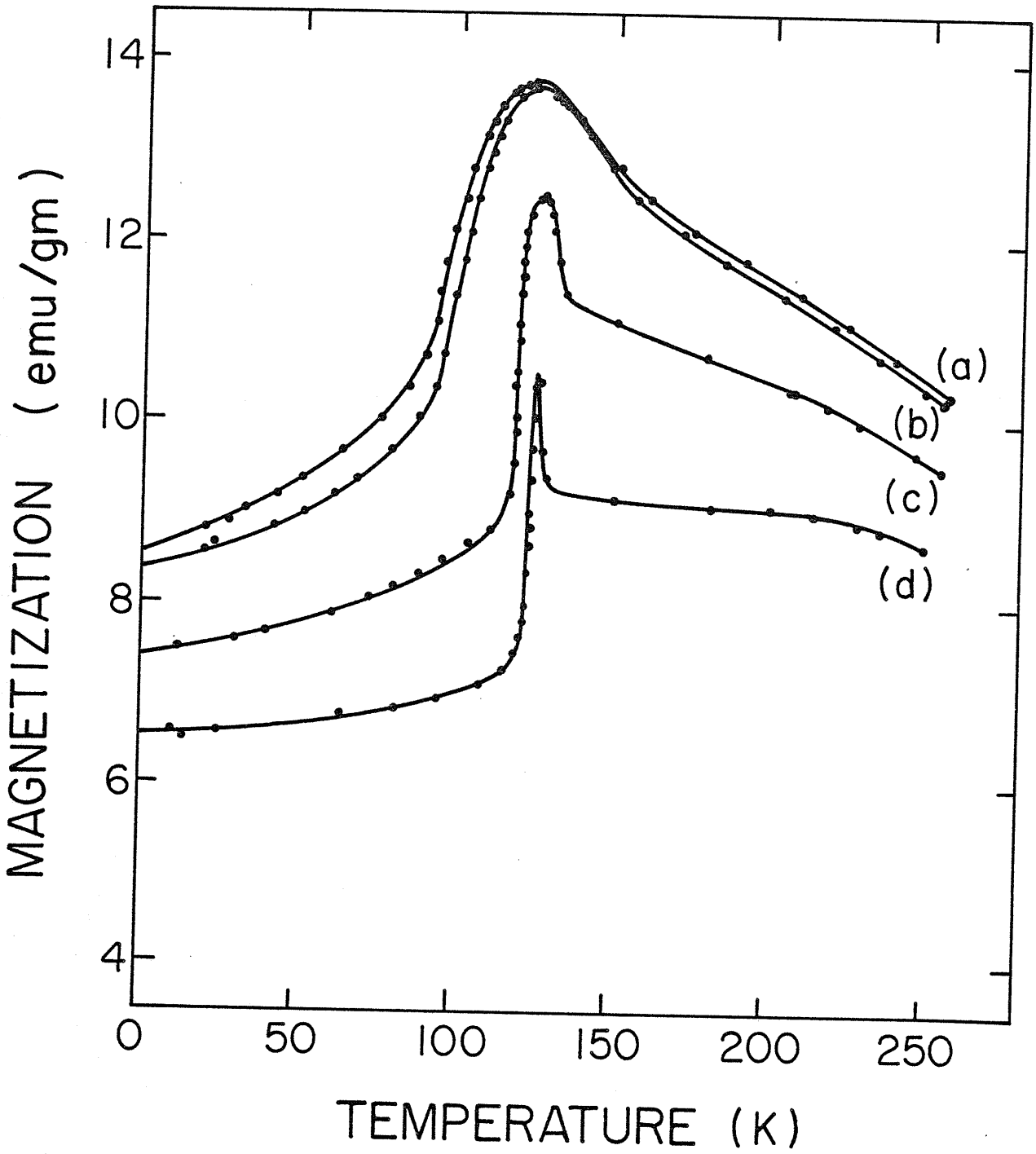

FIGURE 3-10: The magnetization as a function of temperature for a sample with the 3c superstructure in various applied fields: a) H = 18 kOe b) H = 16 kOe c) H = 4 kOe and d) H = 1 kOe.

126 ± 5 K as is expected for a powder sample at the critical temperature where the spins are no longer locked in either the c-plane or along the c-axis. It is worth noting that although fields in the vicinity of 100 kOe are required to saturate powder samples of Fe_7Se_8 at 4.2 K, our value of the magnetization in 18 kOe at T = 126 K, 13.5 emu/gm, is close to the saturation value measured for single crystals at T = 4.2 K.[7]

Below the peak, the magnetization is lower than that above, again due to the reduction in the number of easy directions in the powder as the spin aligns along the c-axis. The coercive field as a function of temperature is plotted for both structures in Figure 3-11. The loosening of spins at the critical temperature in the 3c structure is evident as a sharp reduction in the coercive field.

Both oxidation and decomposition caused problems at higher temperatures. In fact after raising the temperature of samples above their ordering temperature for prolonged periods, distinct changes in their Mössbauer spectra were frequently observed. This restricted the temperature range of the measurements, especially for Mössbauer experiments where collection times of 24 hours or more are not uncommon. The ordering temperature was therefore determined from magnetization measurements only. In Figure 3-12 the magnetization in low fields is plotted as a function of temperature. From this thermal scanning, T_{FN} was found to

(a)

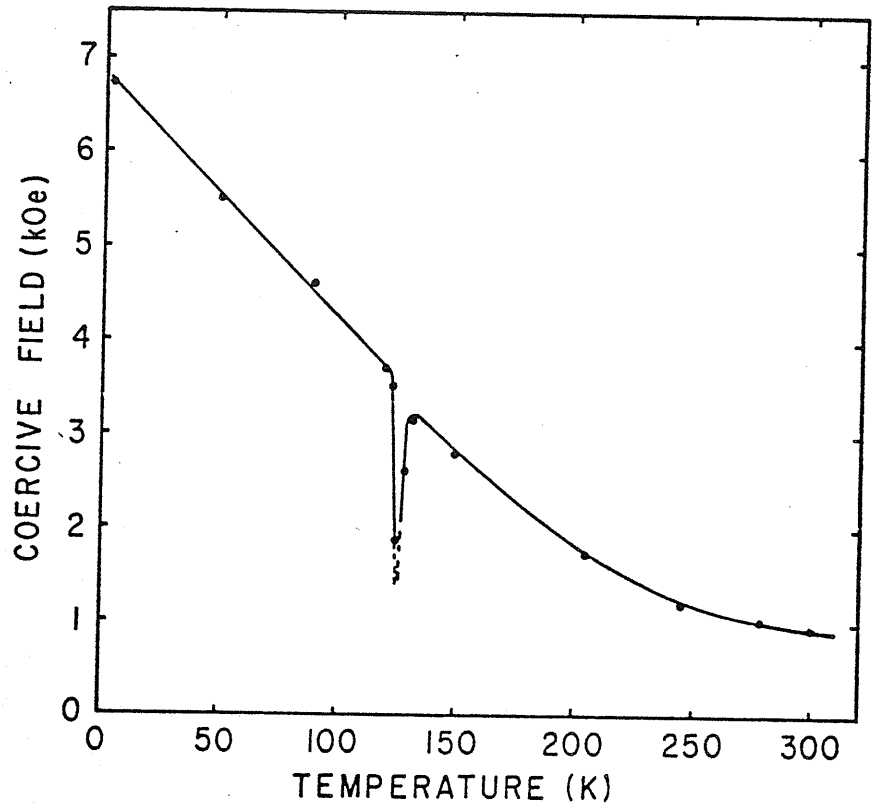

(b)

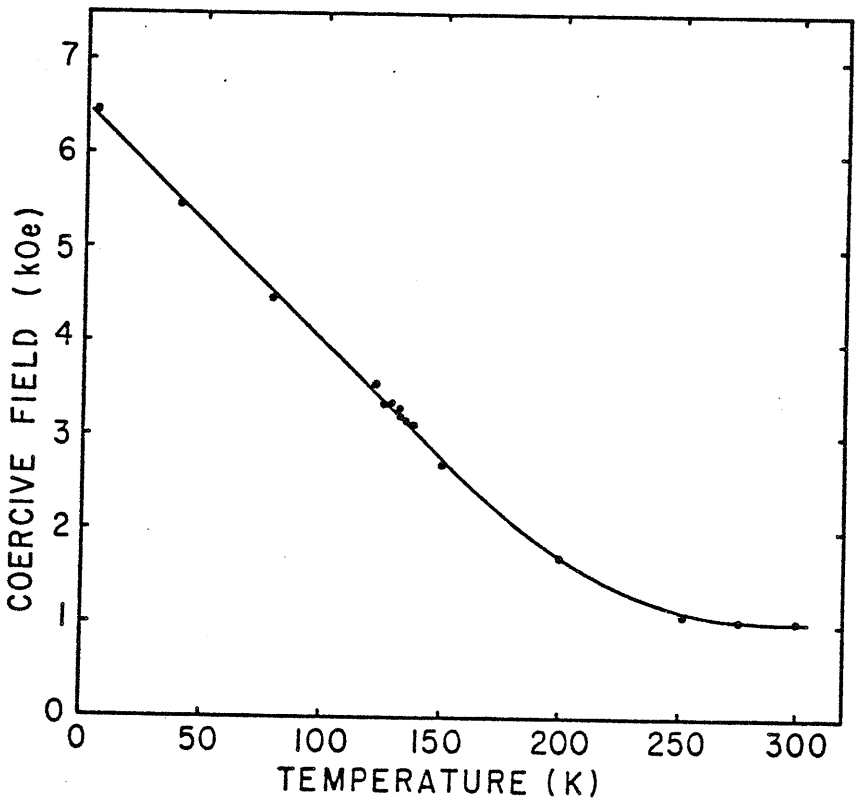

FIGURE 3-11: The coercive field as a function of temperature for a) the 3c and b) the 4c superstructure.

be 457 ± 2 K for both 3c and 4c samples. This is consistent with the phase diagram (Figure 3-3) since after heating from room temperature only the 3c superstructure exists in the temperature range 425 → 510 K.

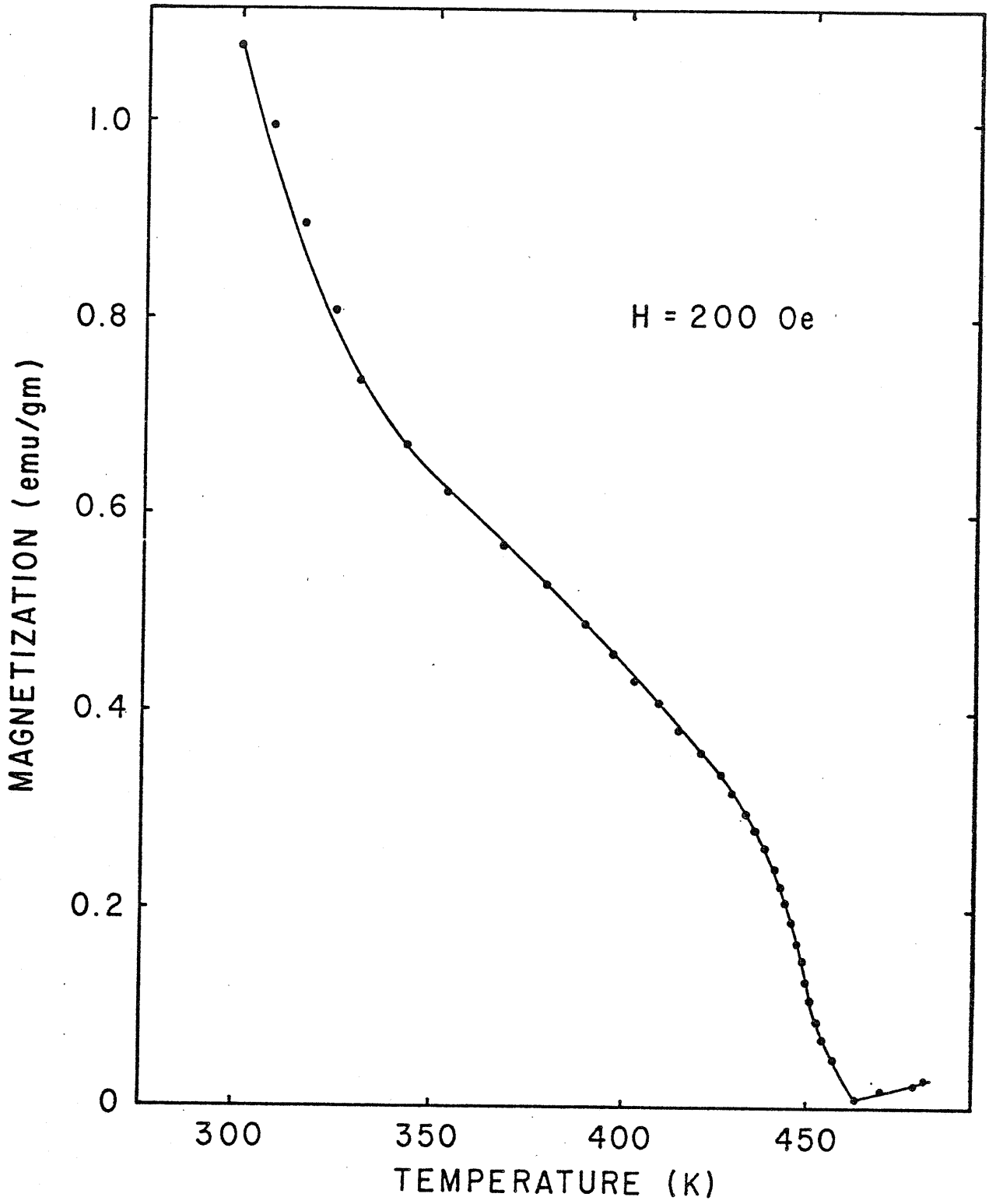

FIGURE 3-12: The magnetization against temperature in low fields close to the ordering temperature.

6. Mössbauer Measurements

Mössbauer spectra were recorded at temperatures from 4.2 to 300 K for both 3c and 4c absorbers using a 25 mCi source of ^{57}Co diffused into a chromium host. External magnetic fields were applied parallel to the γ-ray direction using superconducting solenoids. Fields up to 90 kOe were applied to 'cold worked' samples by Dr. A.H. Morrish at Monash University, Australia, in an unsuccessful attempt to simplify the analysis of the complex spectra shown earlier in Figure 3-6. Examples of the results obtained can be seen in Figure 3-13. The broad overlapping peaks, particularly in the central regions due to the collapse of the inner six-line pattern, prevented a full analysis of these spectra.

6.1 The 3c Structure

Mössbauer spectra over the range 4.2 to 300 K are shown in Figure 3-14. Full computer analysis was performed on the spectra recorded at and above 77 K. Below this temperature the overlapping outer lines caused the programs to give unreliable values for the various Mössbauer parameters.

If the 3c structure proposed by Okazaki is correct, it should be possible to identify the various six-line patterns required to fit the spectra,with iron in magnetically inequivalent sites in the lattice. The different iron sites are shown in Figure 3-15 and their locations in Fe_7Se_8 are

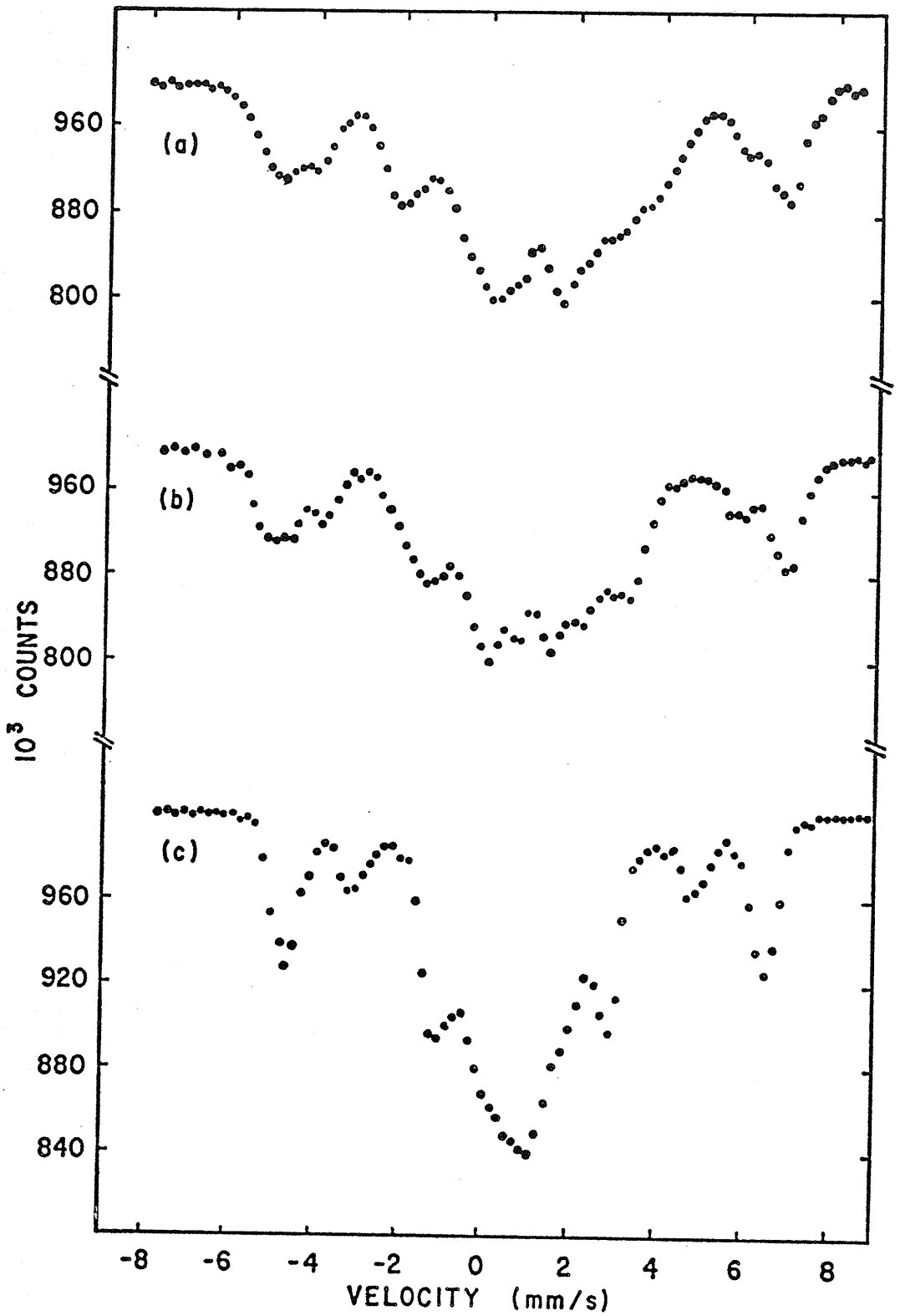

FIGURE 3-13: Examples of Mössbauer spectra recorded from 'ground' absorbers in 90 kOe at a) 4.2 K b) 77 K and c) 250 K.

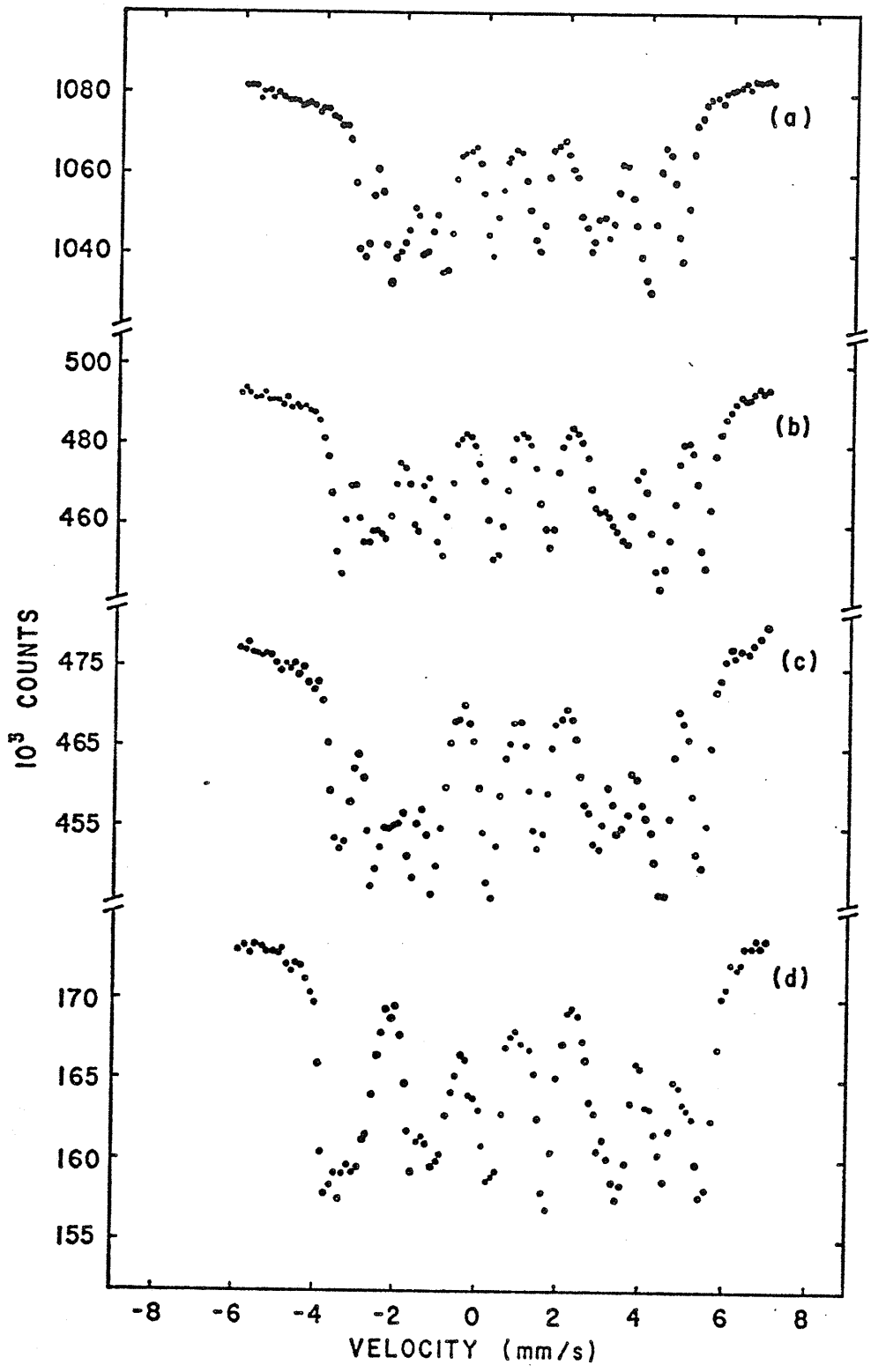

FIGURE 3-14: Mössbauer spectra from samples of Fe_7Se_8 with the 3c superstructure at a) 300 K b) 77 K c) 195 K d) 4.2 K.

indicated schematically in Figure 3-16. The positions of the selenium atoms are not shown, but are in planes between the iron layers.

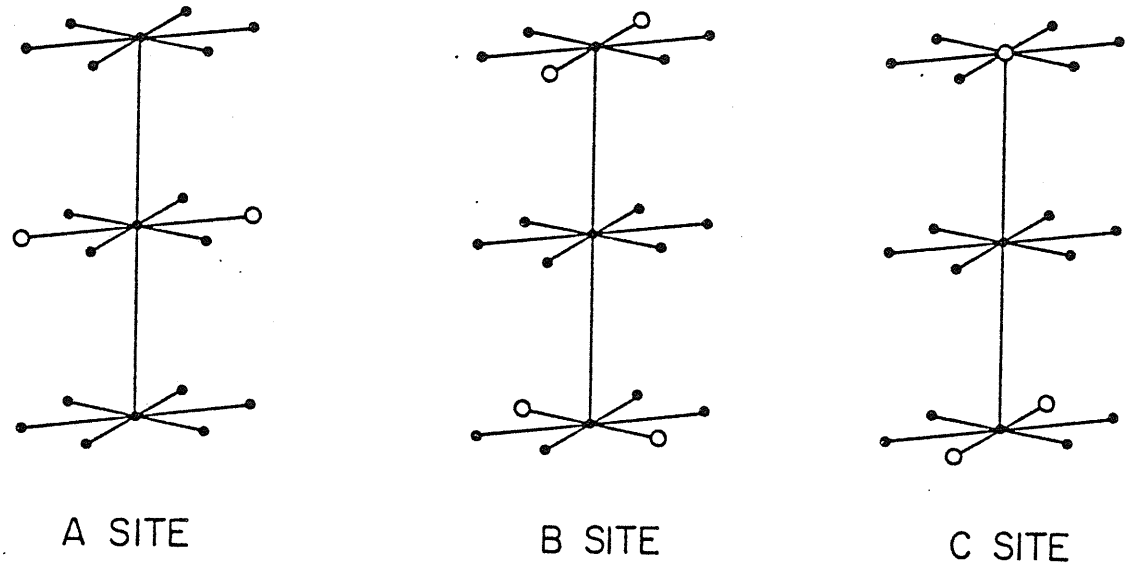

FIGURE 3-15: Configurations of magnetic neighbours and vacancies giving three distinct iron sites in Fe_7Se_8.

There are three main types of iron sites, A, B and C. The strongest magnetic interactions are the antiferromagnetic Fe-Se-Fe superexchange interactions between iron ions in adjacent planes.[13] It is assumed that the hyperfine field depends on the number of such bonds to ions on neighbouring planes. The ferromagnetic interaction between ions on the same plane is supposed to be much weaker [14, 15, 16] and is neglected. These assumptions are strongly supported by the Mössbauer experiments. An A-site has two adjacent ferromagnetic cation sites vacant. B- and C-sites have four and three antiferromagnetic cations missing respectively. Since

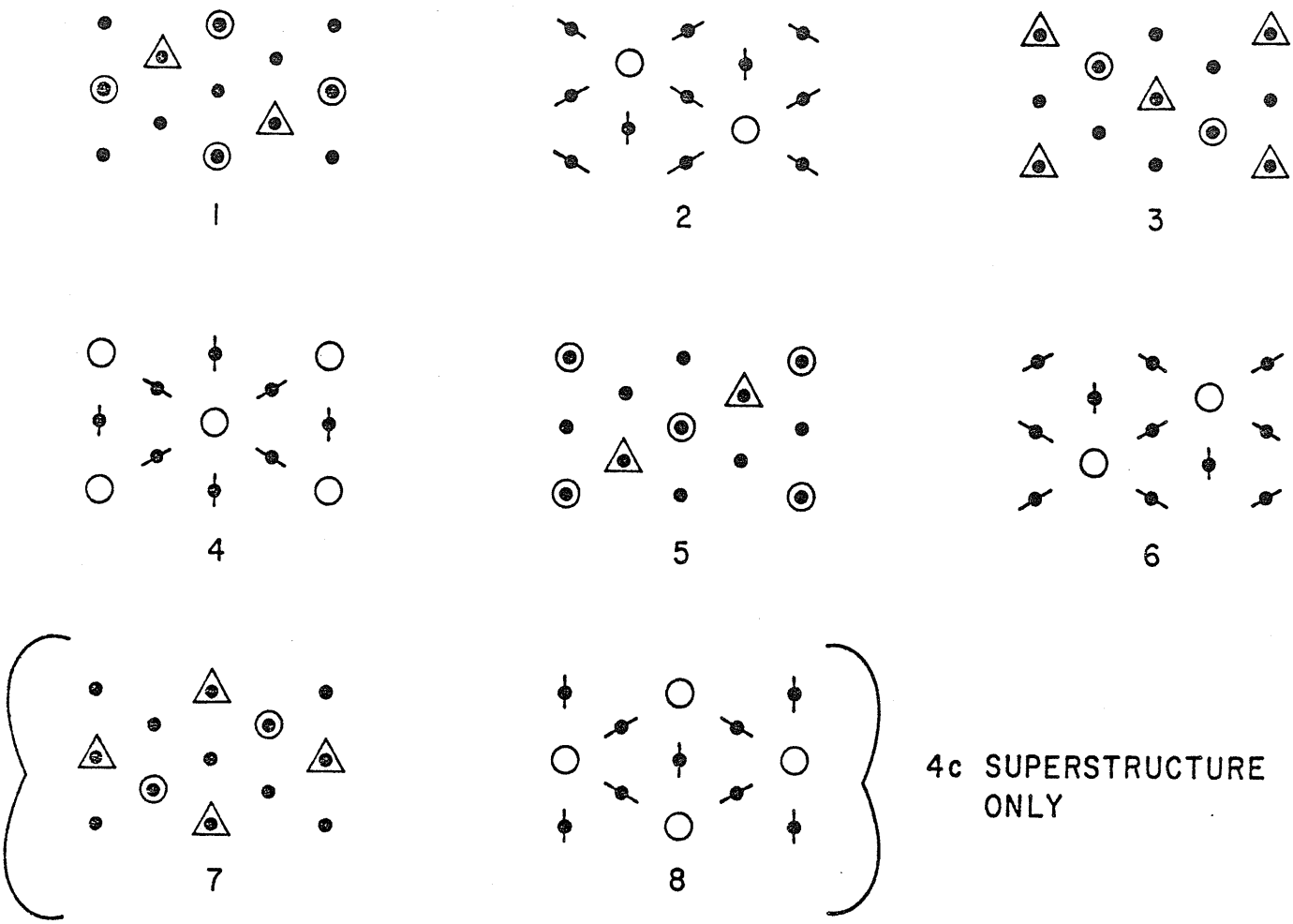

SYMBOL	DESCRIPTION	TYPE OF SITE	NUMBER/UNIT CELL	
			4c super structure	3c super structure
⊷	Vacancies in the plane in the direction of the lines	A	24	18
•	No nearest neighbour vacancies	B	16	12
◉	Vacancy below	C	8	6
▲	Vacancy above		8	6
○	Vacancy		8	6

FIGURE 3-16: Positions of the different iron sites on the layers of the unit cells shown in Figure 3-2. Selenium atoms omitted for clarity.

there are three interplanar cation-anion-cation links between cations vertically adjacent to each other, the C-sites have 5 bonds missing and we expect $H_A > H_B > H_C$ where H_A, H_B and H_C represent the hyperfine fields at the A, B and C-sites respectively.

The A-sites can be further subdivided into A_1- and A_2-sites depending on whether the line joining the vacant sites lies along or is at an angle of 60^o to the spin-direction in the c-plane as indicated in Figure 3-15. The angular dependence $(3\cos^2\theta - 1)$ of the electric quadrupole coupling will give different contributions to the quadrupole shift for the two sites when the spins lie in the c-plane and hence split their Mössbauer patterns above the spin rotation temperature. The multiplicity ratio of the sites is $A_1:A_2:B:C = 1:2:2:2$ and their corresponding Mössbauer spectra should have these relative intensities.

Figure 3-17 shows fully fitted spectra above and below the spin rotation temperature. The only constraints on the final fit were that all peaks should have a Lorentzian line shape with the same line width. The outermost lines are identified as absorptions from ions in A_1- and A_2-sites and the relative intensities are 1:2 as predicted. It is then anticipated that there will be two absorption lines, one each for B- and C-site ions. In fact, although the data can be fitted with only two additional patterns, a better chi-squared value is obtained with three patterns (as shown).

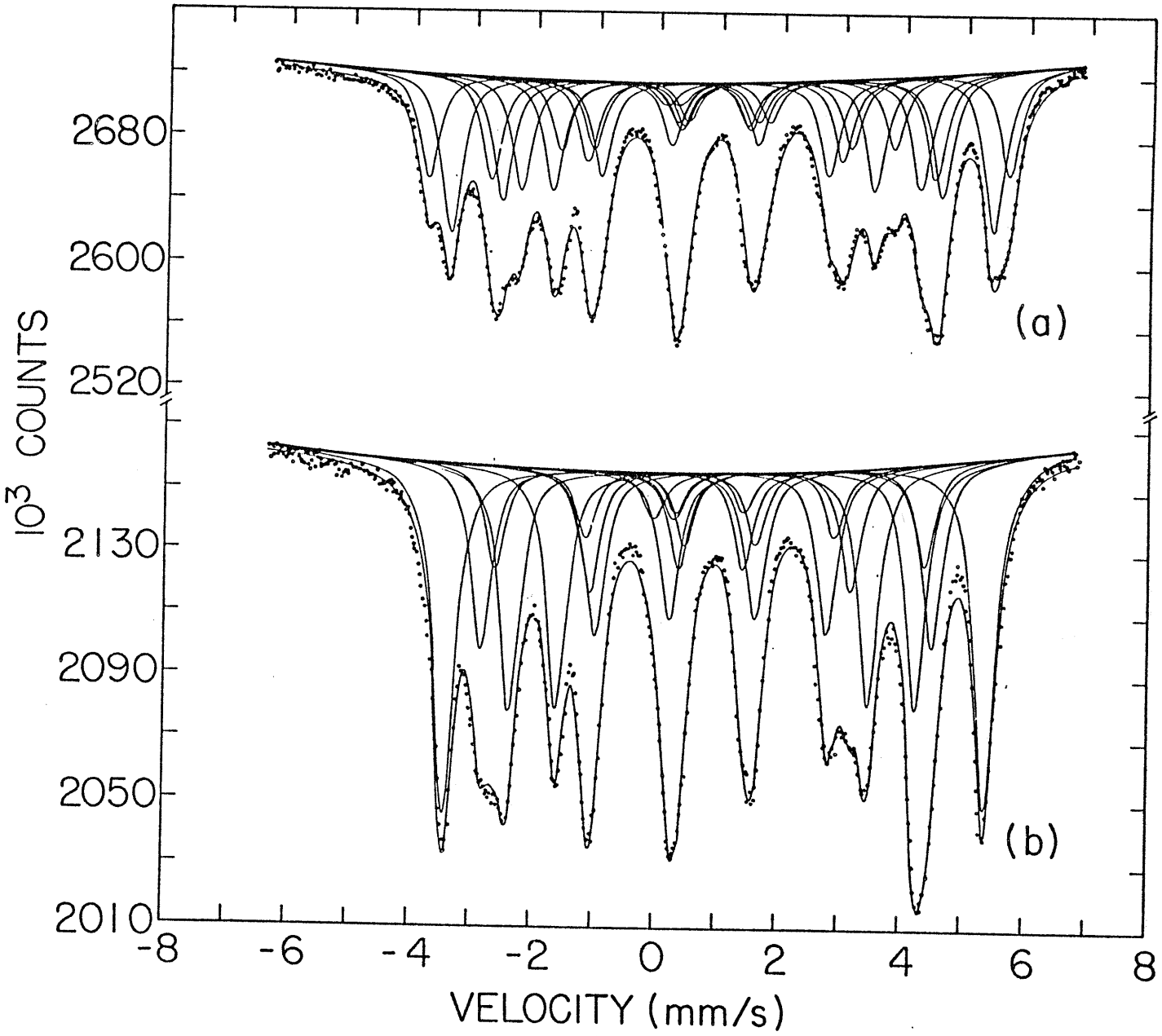

FIGURE 3-17: Spectra from a sample with the 3c superstructure a) at 135.5 K

The sum of the three intensities compared to that of the two A-absorptions agrees with the predicted value of 4:3.

It seems reasonable to suppose that if some minor disorder does exist, it must be confined to the vacancies on alternate planes so as not to effect the overall superstructure. If our assumption of a weak ferromagnetic interaction between ions on the same plane is correct, then the effect of this disorder on the A-sites will be much smaller than on the B- and C-sites. This is indeed the case. Instead of two distinct hyperfine fields from the B- and C-sites, there is a distribution which can apparently be better represented by three six-line Mössbauer patterns.

At T = 130.0 K and below, the spectra show only one A-site pattern (Figure 3-17 spectrum b). The three patterns for the B- and C-sites still persist and the intensity ratio $I_A:(I_B + I_C)$ remains 3:4. The difference in the A-site spectrum above and below the phase transition temperature suggests that the dipole-dipole interactions are at least partially responsible. The dipole contributions to the hyperfine fields at the A_1- and A_2-sites are equal when the spins are parallel to the c-axis, whereas when the spins are in the c-plane the contributions depend on the orientation of the vacant sites. The absence of any A-site splitting in Figure 3-17 spectrum b supports the observations of Okazaki and Hirakawa [2] that the spins lie exactly along the c-axis below the transition temperature.

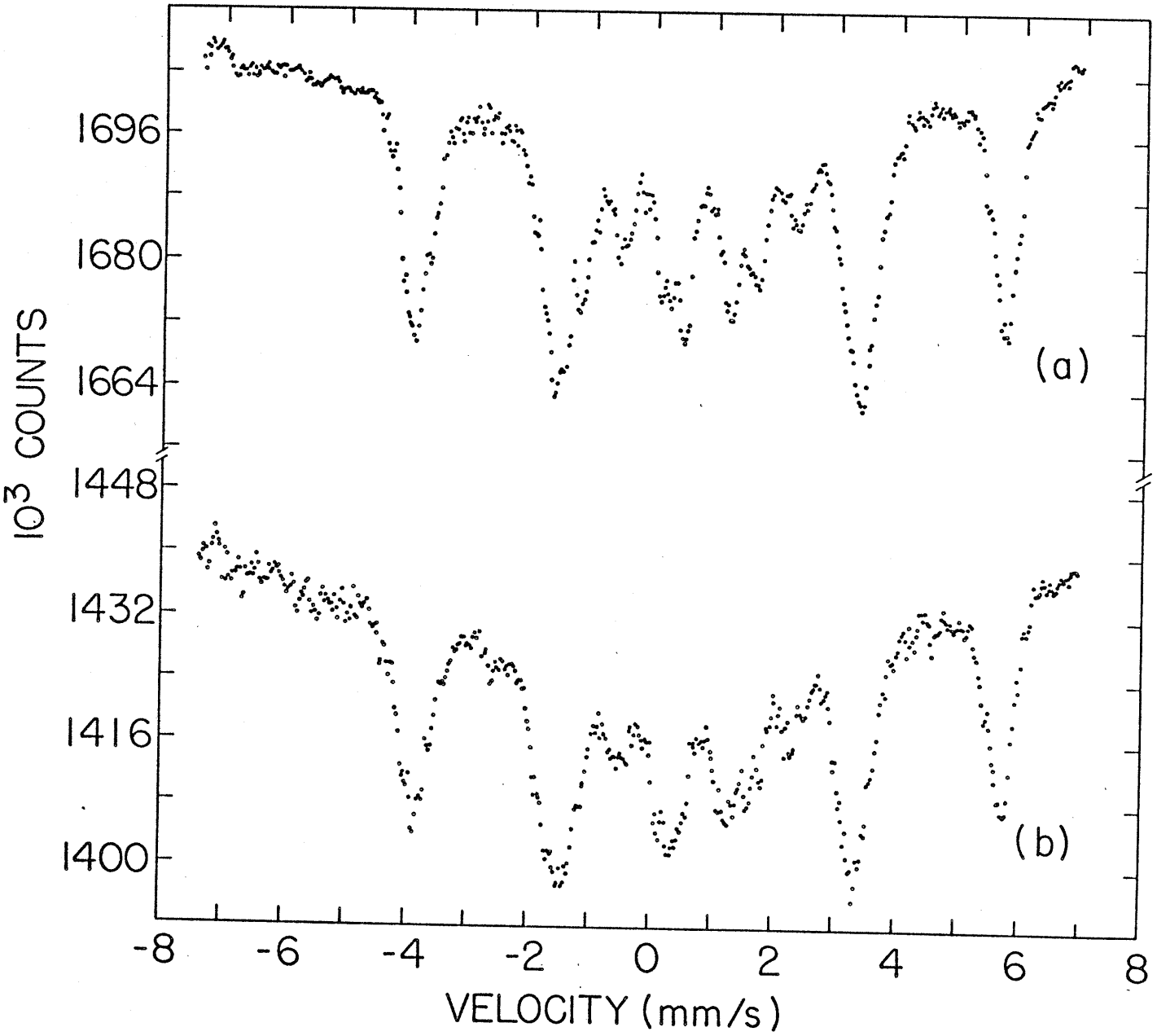

FIGURE 3-18: Spectra obtained at room temperature in an applied field of 50 kOe for an absorber with a) the 3c superstructure and b) the 4c superstructure.

A spectrum taken at room temperature in an external magnetic field of 50 kOe applied parallel to the propagation direction of the γ-rays is shown in Figure 3-18 spectrum a. The 2 and 5 lines ($\Delta M = 0$ transitions) are greatly reduced but not absent indicating that saturation was incomplete. The spins at the B- and C-sites lie parallel to one another and antiparallel to those on the A-sites. Thus the net moment will be in the direction of the B- and C-site spins. Since the hyperfine field is in the opposite direction to the atomic moment in ^{57}Fe, [17, 18] we expect the external field to decrease H_B and H_C, and to increase H_A. (Note that the splitting of the A-site pattern is observed only as a line broadening at room temperature, as shown in Figure 3-7 spectrum a or d). By inspection of Figure 3-18 spectrum a as compared to Figure 3-7 spectrum a, it is clear that the splitting of the outermost pattern has increased whereas that of the inner patterns has decreased. This result confirms our identification of the pattern associated with the A-site ions.

The hyperfine fields for the various sites are shown as a function of temperature in Figure 3-19. For the B- and C-sites the data are plotted for the outer and inner patterns associated with these sites. The magnitudes of all the hyperfine fields change abruptly at about 130 K. This is presumably to be associated with the spin rotation at this temperature.

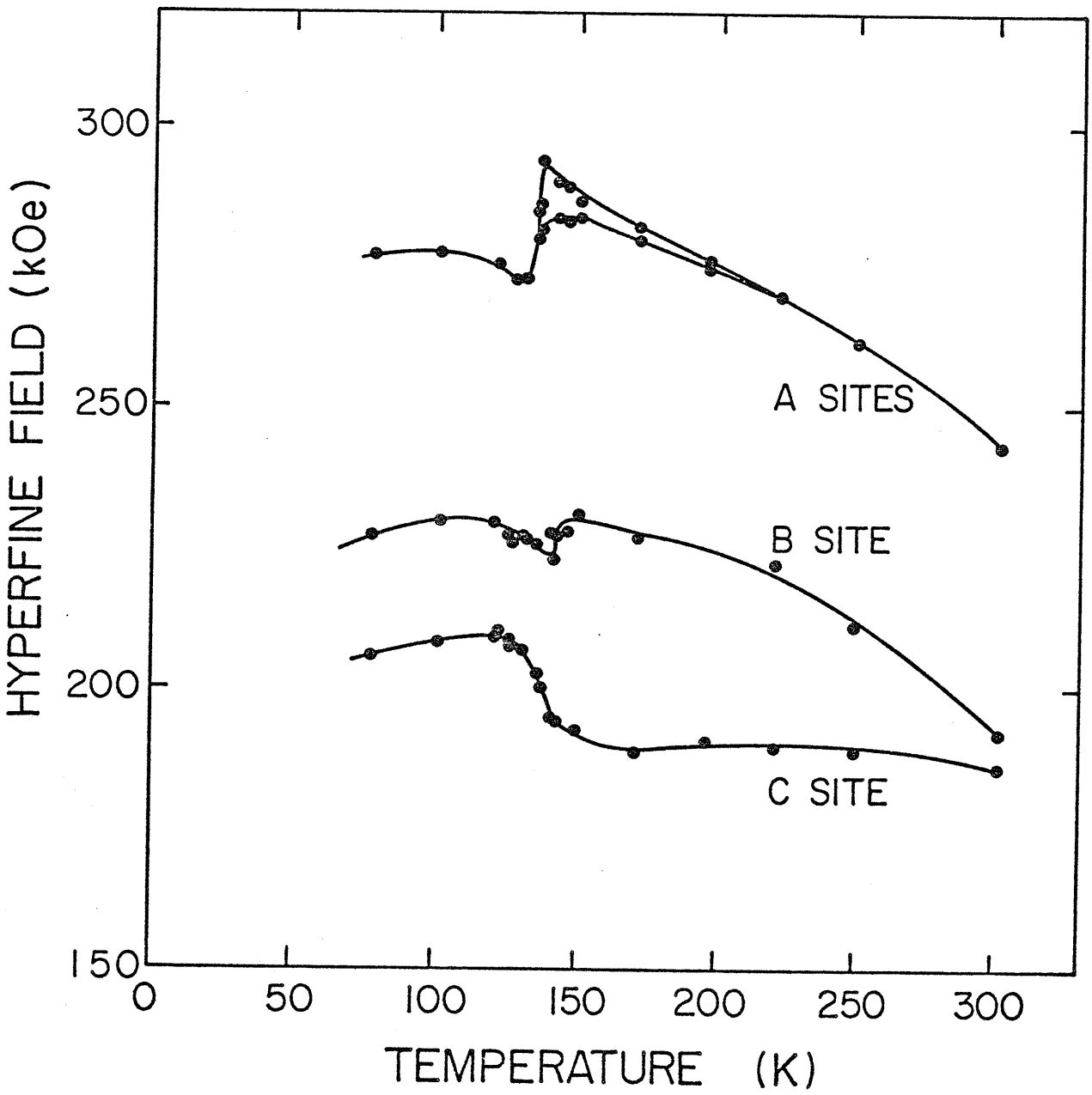

FIGURE 3-19: The temperature dependence of the hyperfine field for the 3c superstructure.

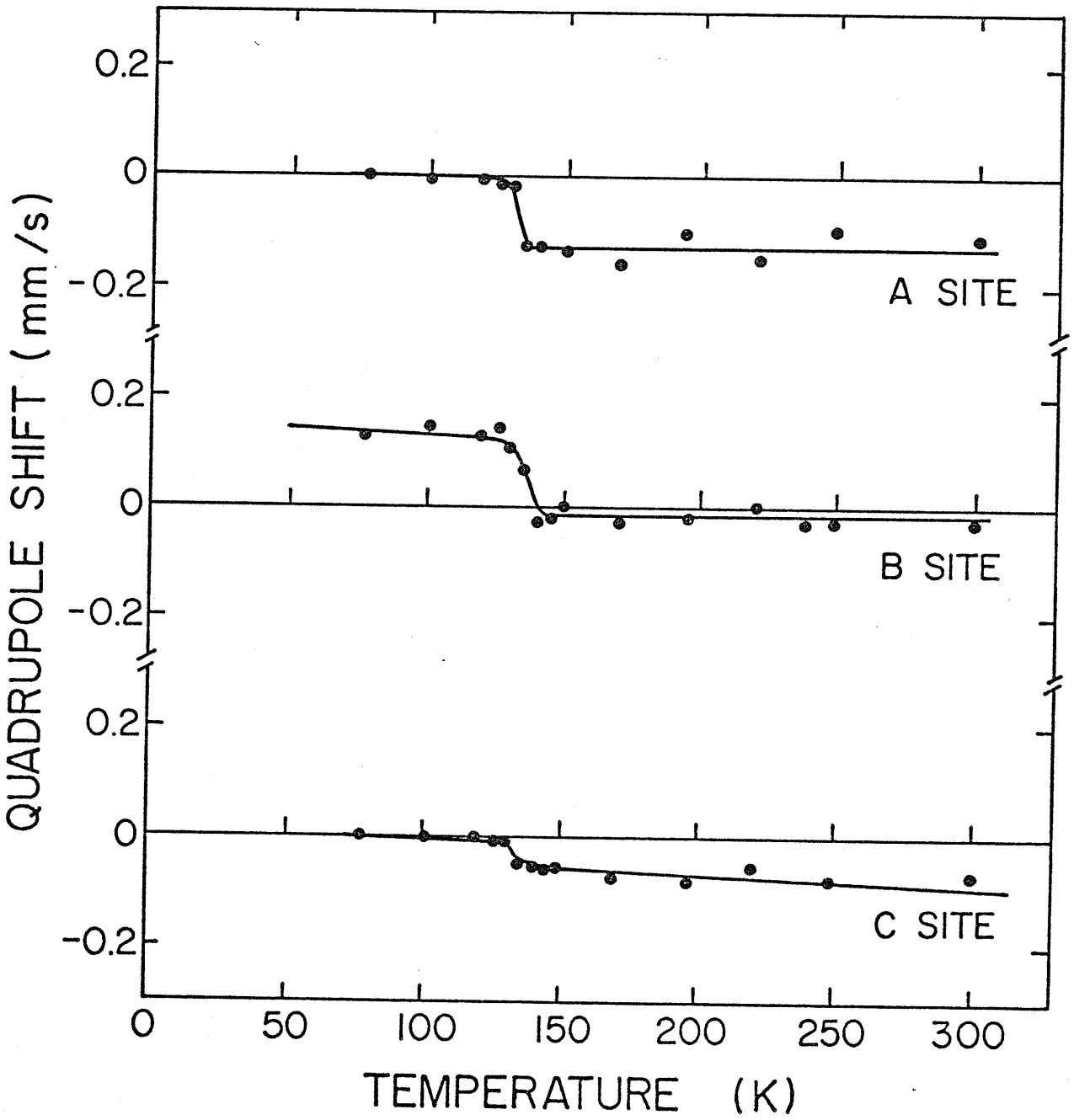

FIGURE 3-20: The temperature dependence of the quadrupole shift defined as $\frac{1}{4}\left\{\Delta_{21} - \Delta_{65}\right\}$ *for the 3c structure.* Δ_{21} *and* Δ_{65} *are the distances between the outermost lines on the left and right hand sides of the spectrum respectively.*

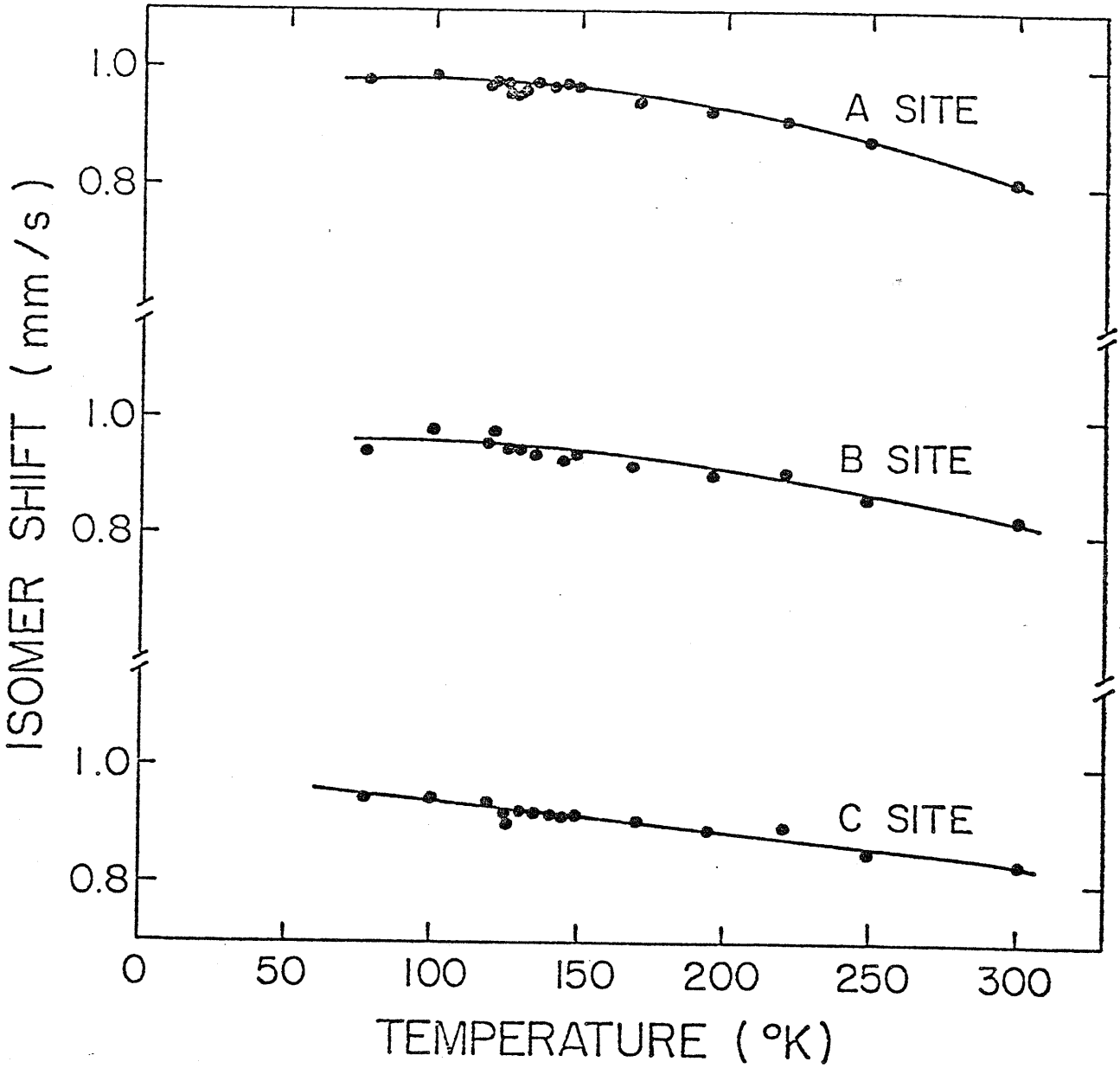

FIGURE 3-21: The temperature dependence of the isomer shift for the 3c structure.

Even stronger evidence for the spin rotation is provided by the measured quadrupole shifts in spite of the large errors due to overlapping patterns. We define the quadrupole shift as $\frac{1}{4}(\Delta_{21} - \Delta_{65})$ where Δ_{21} and Δ_{65} are the splittings in mm/s between the second and first, and fifth and sixth lines of the spectrum respectively. As shown in Figure 3-20, the quadrupole shift at all sites undergoes a sudden change at T = 130 K as would occur if the angle between the principal axis of the electric field gradient and the direction of the hyperfine field changed abruptly at this temperature.

The isomer shifts relative to chromium are shown as a function of temperature in Figure 3-21. They are $\sim$ 0.82 mm/s at T = 300 K at all sites, increasing monotonically to $\sim$0.97 mm/s at T = 77 K. These values imply that all the cations are in the ferrous Fe^{2+} state.

6.2 The 4c Structure

Mössbauer spectra from 4c absorbers are shown in Figure 3-22 covering the temperature range 4.2 K to 300 K. Again full analysis was limited to spectra recorded at or above 77 K. The spectra were adequately fitted with four overlapping patterns as shown in Figure 3-23. The two outermost patterns (with the largest hyperfine fields) are now identified as corresponding to cations in A_2- and A_1-sites respectively, on the basis of their relative line intensities. The triclinic lattice distortion should split

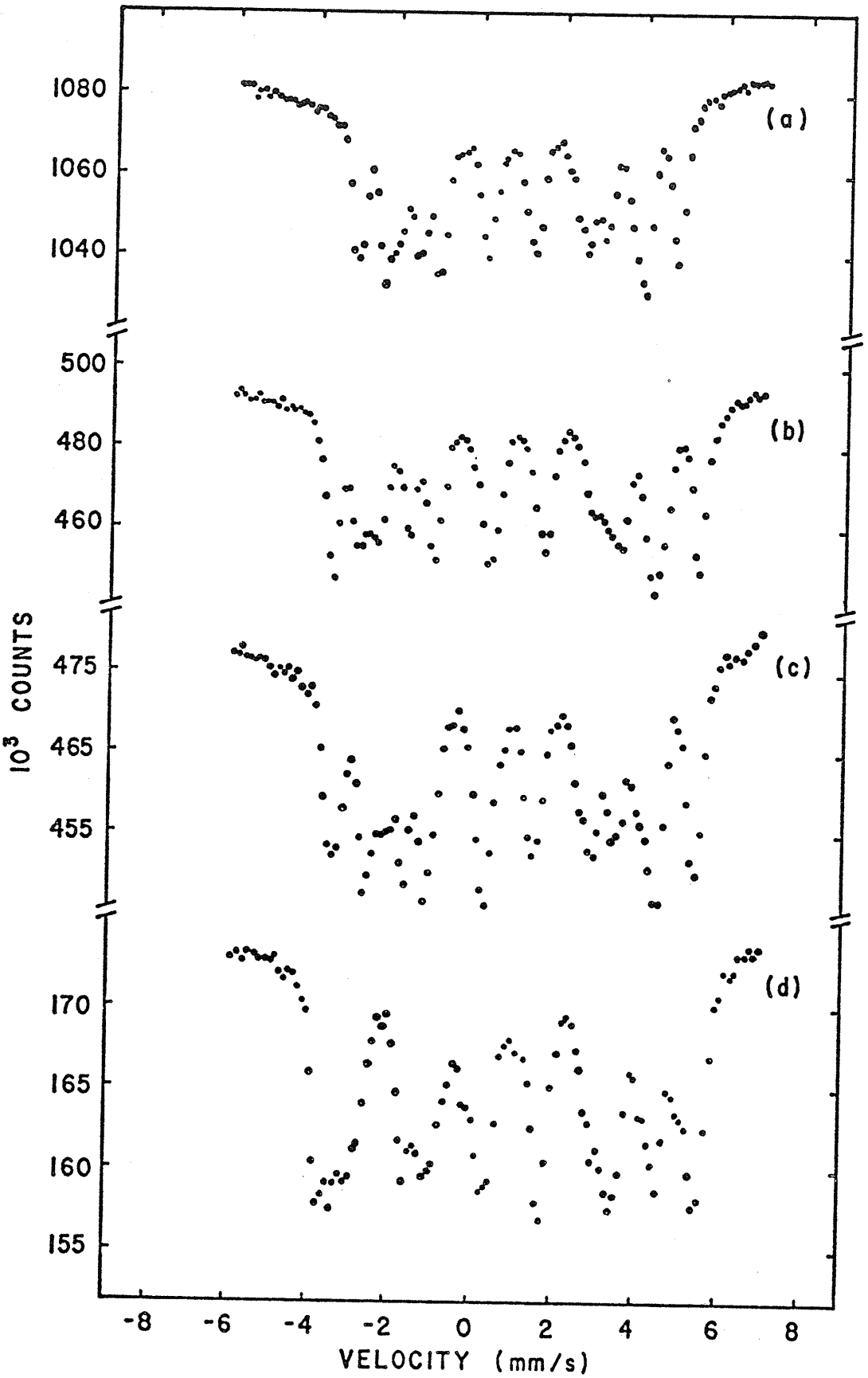

FIGURE 3-22: Mössbauer spectra from samples of Fe_7Se_8 with the 4c superstructure at a) 300 K b) 195 K c) 77K d) 4.2 K.

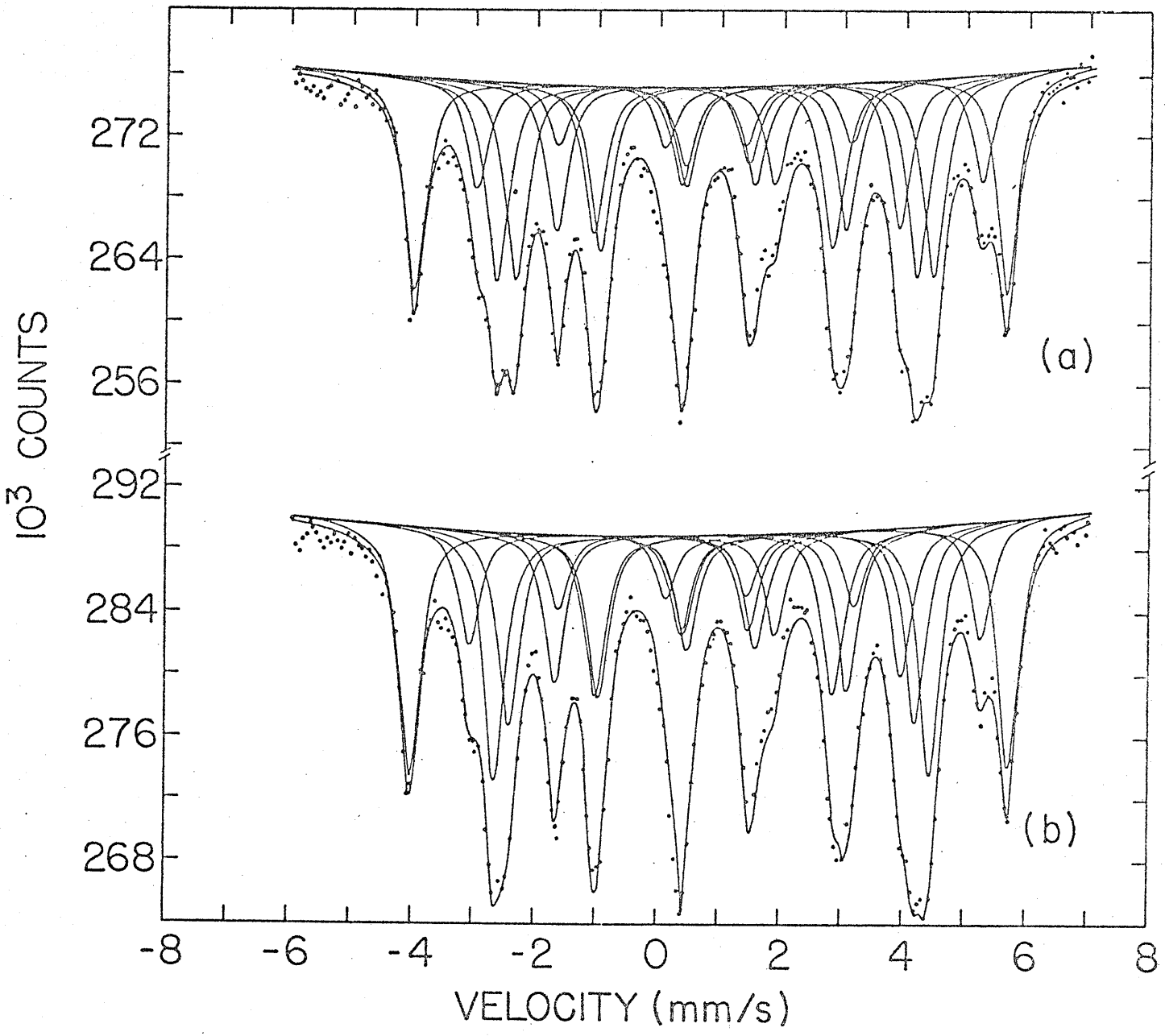

FIGURE 3-23: Spectra from a sample with the 4c superstructure a) at 145.0 K and b) at 121.0 K.

the A-site pattern into three due to the different contributions to the quadrupole shift. Further splitting due to this distortion was not detected, although the relative magnitude of the hyperfine fields of the A_1- and A_2-sites is reversed as compared to the 3c structure.

The distorted lattice also seems to inhibit any vacancy disorder in the 4c structure since the B- and C-site absorptions now appear as two distinct six-line patterns. As can be seen from the fitted spectra in Figure 3-23, the relative intensities are in good agreement with the site multiplicity. A spectrum from a 4c sample in an applied field of 50 kOe is plotted in Figure 3-18 spectrum b and although saturation is again incomplete, it confirms the pattern identifications. The splitting of the A-sites does not disappear below 130 K (Figure 3-23 spectrum b) and the spectra do not show the abrupt changes at this temperature characteristic of the 3c structure.

The quadrupole shifts as a function of temperature are plotted in Figure 3-24 and show continuous changes, consistent with the gradual rotation of the spin direction observed for the 4c structure. The hyperfine fields and isomer shifts are given as a function of temperature in Figure 3-25 and 3-26. The isomer shifts indicate that the iron is again in the ferrous state.

No trace of Fe^{3+} ions was found even at low temperatures. If an electron hopping mechanism exists between the Fe^{2+} and Fe^{3+} ions similar to that proposed

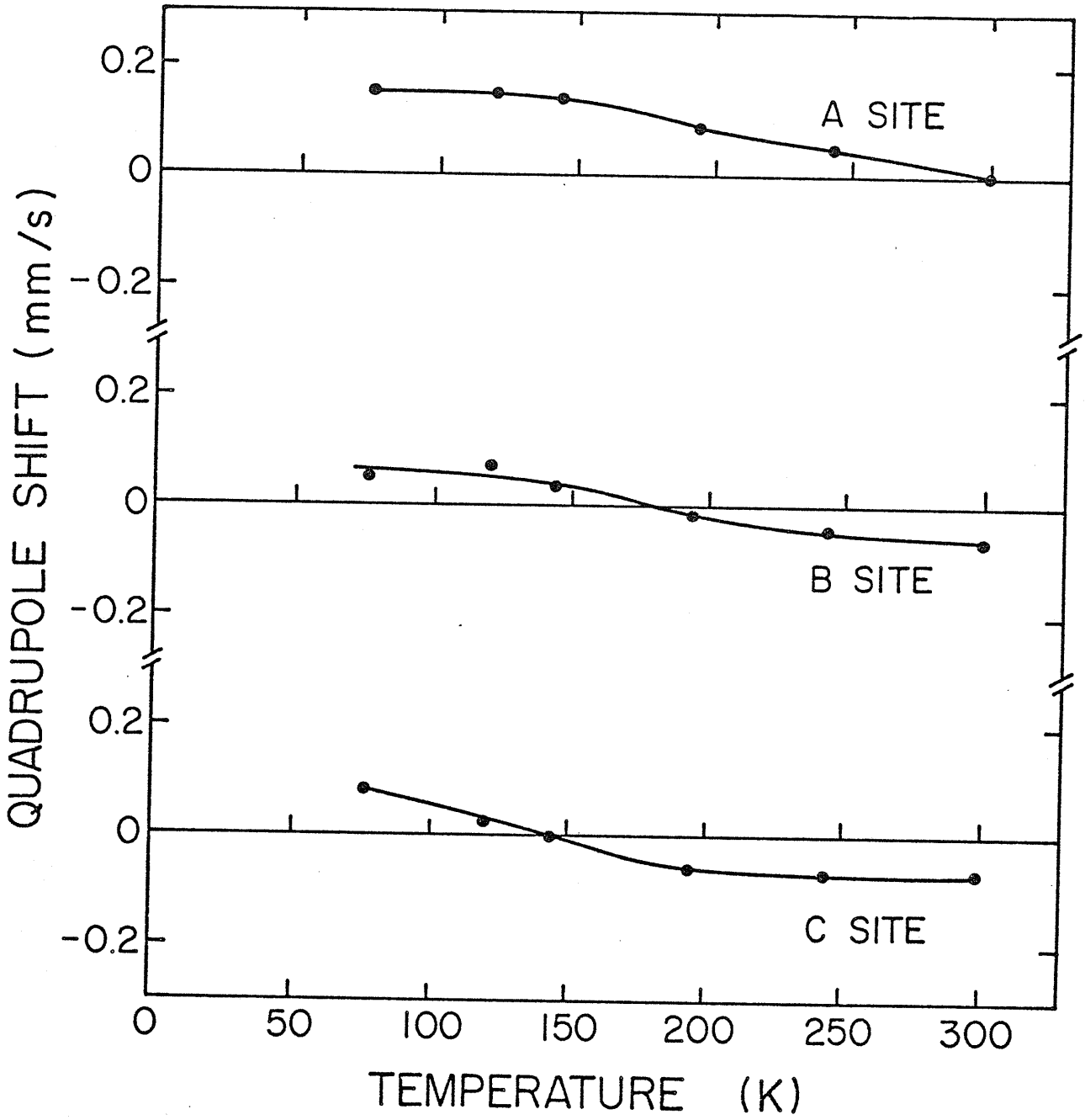

FIGURE 3-24: The quadrupole shift $\frac{1}{4}\{\Delta_{21} - \Delta_{65}\}$ *versus temperature for 4c -* Fe_7Se_8.

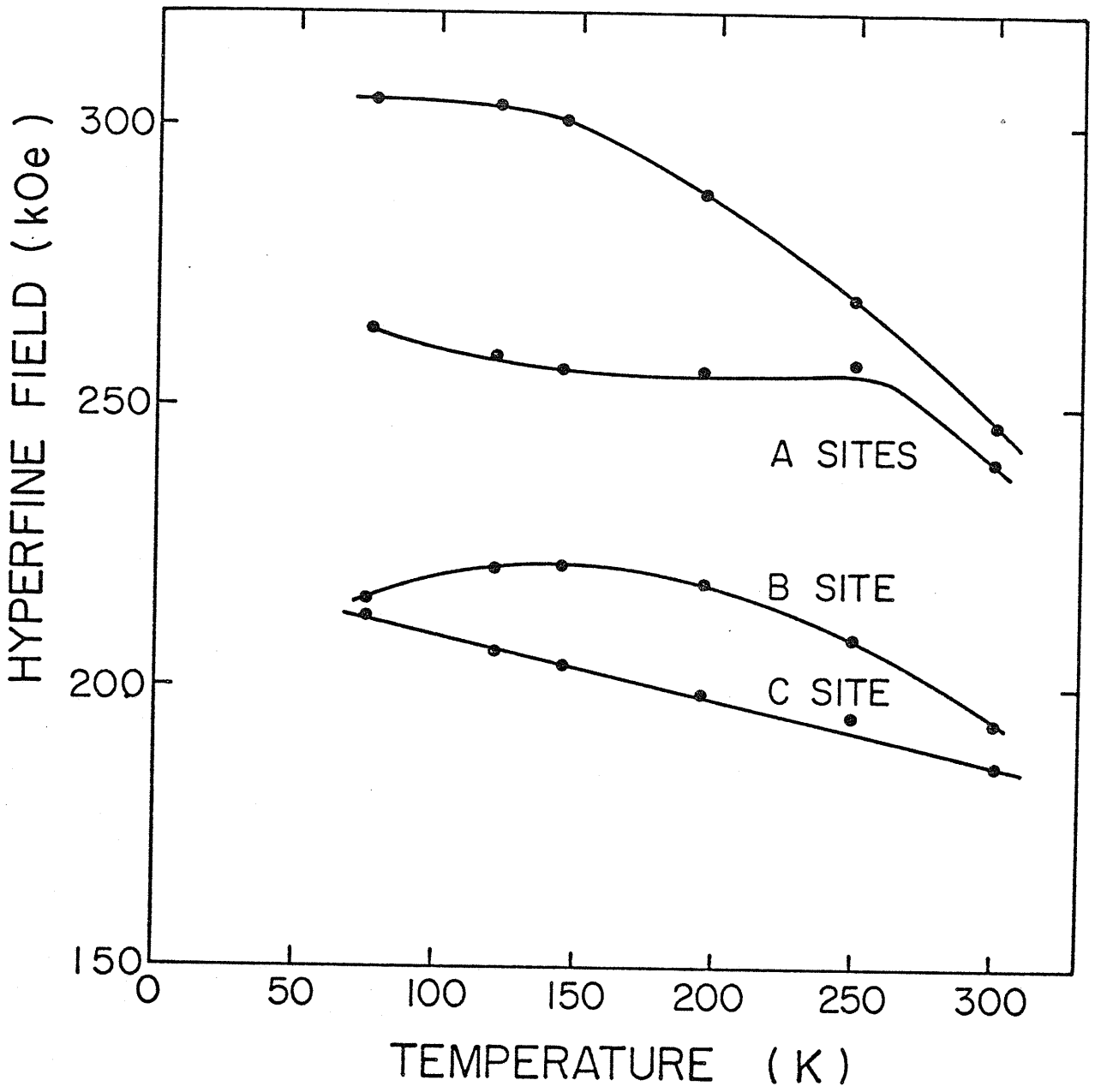

FIGURE 3-25: The temperature dependence of the hyperfine field for the 4c structure.

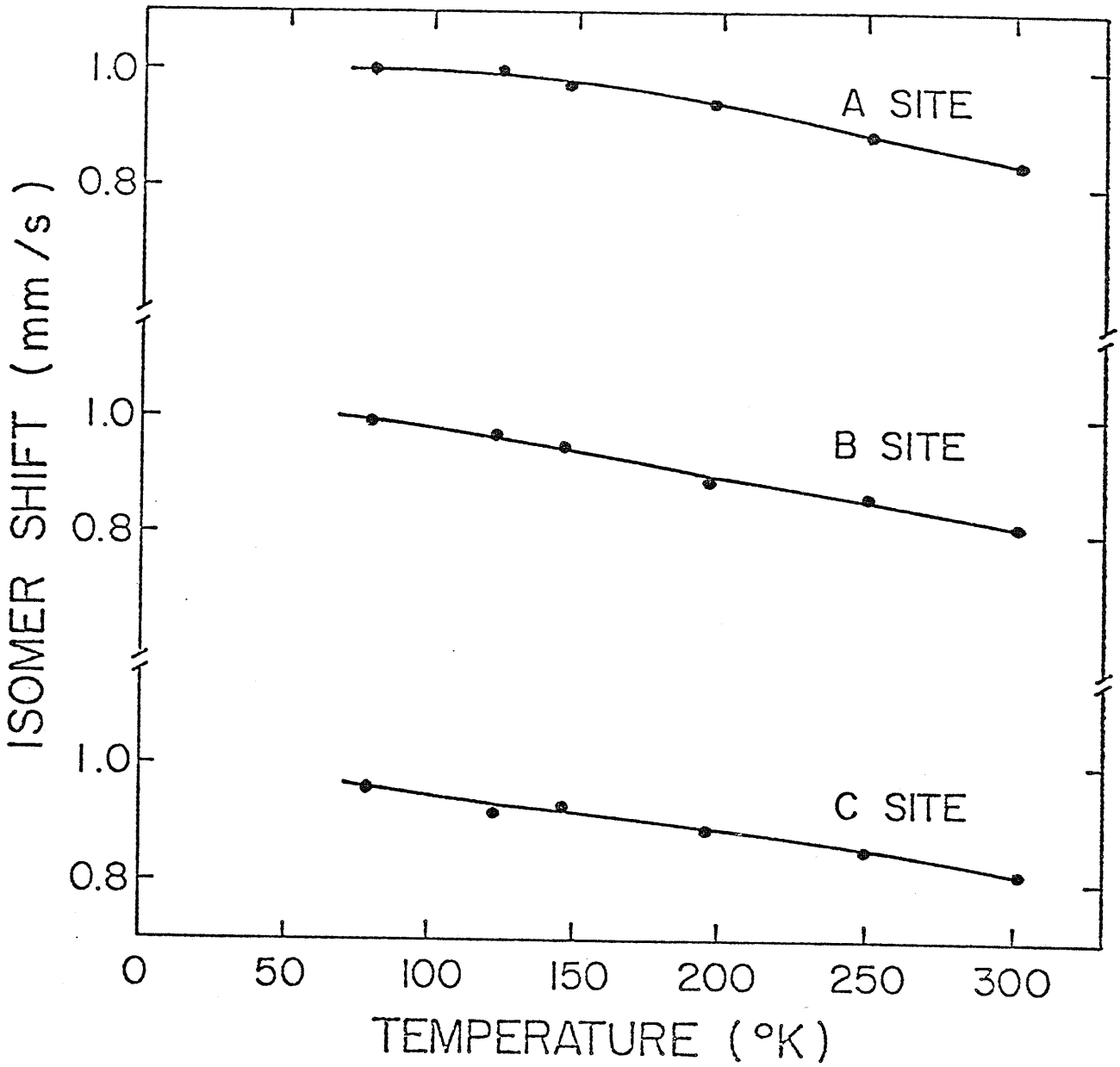

FIGURE 3-26: The Isomer shift as a function of temperature for the 4c structure.

for Fe_3O_4[19] to account for only one type of iron ion in the Mössbauer spectra, the hopping frequency must be fast with respect to the nuclear Larmour frequency even at 4.2 K. A more likely explanation was suggested by Ward[13] for the pyrrhotite (Fe_7S_8) case. Since all the iron cannot be Fe^{2+} and the sulphur S^{2-} he proposed that the necessary charge balance takes place via holes residing in orbitals which are mainly centred on the sulphur ions.

This situation is drawn schematically in Figure 3-27 a. The energy E is plotted against the density of states g. The outer 4p electrons from the selenium atoms form a broad valence band which overlaps a narrow band formed by the iron 3d electron levels. The conduction band arises from a broadening of the metal 4s electron levels due to the large overlap of metal s-functions and selenium p-functions.[20] Charge balance is then conserved by two holes/molecule in the valence band (selenium orbitals). Fe^{2+} ions, arranged with the ferrimagnetic structure discussed earlier would produce a net moment of $4\mu_B$/molecule which is in disagreement with the measured saturation moment of $2\mu_B$/mole. This difficulty can be overcome however if it is assumed that there is considerable spin splitting of the valence band at low temperatures such that all the holes reside in one sub-band as shown in Figure 3-27 b. This leads to a moment of $2\mu_B$ antiparallel to the net Fe^{2+} moment of $4\mu_B$. Similar valence band polarization has been used [21] to explain the low temperature moment in $CuCr_2X_4$ (X = S, Se, Te).

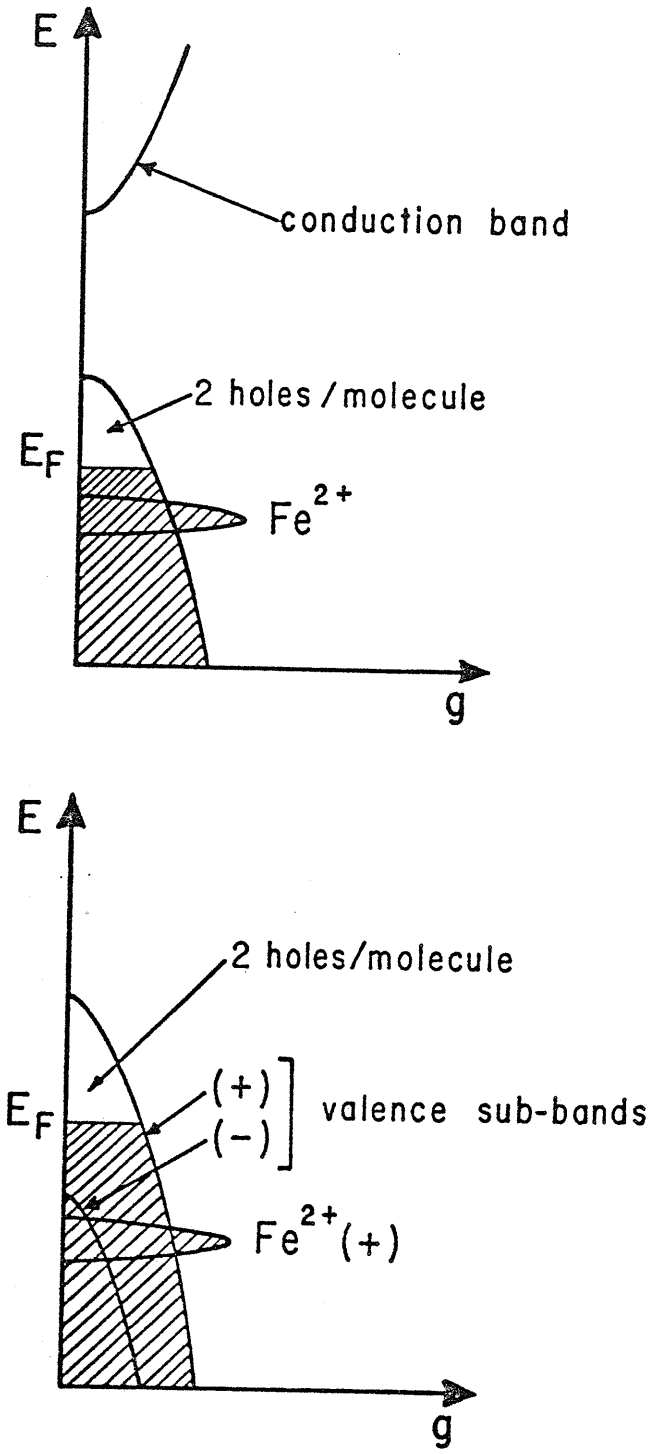

FIGURE 3-27: *a) An energy level scheme for Fe_7Se_8.*
b) The effect of band polarization.
The energy E is plotted versus the density of states g, and $\int g dE$ gives the number of states per molecule.

REFERENCES - CHAPTER III

1. A. Okazaki and K. Hirakawa, J. Phys. Soc. Japan 11, 930 (1956).
2. A. Okazaki, J. Phys. Soc. Japan 16, 1162 (1961).
3. K. Hirakawa, J. Phys. Soc. Japan 12, 929 (1957).
4. A.K. Andresen and J. Leciejewicz, J. Physique 25, 574 (1964).
5. M. Kawaminami and A. Okazaki, J. Phys. Soc. Japan 29, 649 (1970).
6. M. Kawaminami and A. Okazaki, J. Phys. Soc. Japan 22, 924 (1967).
7. T. Kamimura, K. Kamigaki, T. Hirone and K. Sato, J. Phys. Soc. Japan 22, 1235 (1967).
8. W.A. Robertson, J. Geophys. Res., 68, 2299 (1963).
9. C.W.F. Everitt, Phil. Mag., 7, 831 (1962).
10. E.W. Nuffield, X-Ray Diffraction Methods, John Wiley and Sons, New York (1966).
11. J.R. Regnard and J.C. Hocquenghem, J. Physique Suppl. C1 32, 264 (1971).
12. K. Sato, J. Phys. Soc. Japan 21, 733 (1966).
13. J.C. Ward, Rev. pure and appl. Chem. 20, 175 (1970).
14. L.M. Levinson and D. Treves, J. Phys. Chem. Solids 29, 2227 (1968).
15. H.N. Ok and S.W. Lee Phys. Rev. B 8, 4267 (1973).
16. J.B. Goodenough, Magnetism and the Chemical Bond,

Interscience, New York (1963).

17. S.S. Hanna, J. Heberle, G.J. Perlow, R.S. Preston and D.H. Vincent, Phys. Rev. Lett., 4, 513 (1960).

18. J.M.D. Coey, Ph.D. Thesis, University of Manitoba (1971).

19. J.M.D. Coey, A.H. Morrish and G.A. Sawatzky, J. Phys. 32, C1-271 (1971).

20. F.K. Lotgering, R.P. Van Stapele, G.H.A.M. Van Der Stein and J. S. Van Wieringen, J. Phys. Chem. Solids 30, 799 (1969).

21. F.K. Lotgering and R.P. Van Stapele, J. Appl. Phys. 39, 417 (1968).

CHAPTER IV

PROPERTIES OF THE MIXED SYSTEM $Fe_xCu_{1-x}Rh_2S_4$

Compounds in this series crystallize with the same general structure as the mineral spinel $MgAl_2O_4$.[1] The usual reason for the study of complex mixed systems such as the above is the opportunity they provide to examine the dependence of exchange interactions or transport properties on cation separation.[2, 3, 4] These goals are seldom realized however. Cation disorder, lattice distortions, covalency effects and magnetic or crystal structure changes are a few of the many variables which can complicate analysis of the experimental results.

Despite these drawbacks it seemed strange at the outset of this project that a detailed analysis of this system had not been attempted. Rhodium is known to have a strong preference for the octahedral sites of sulphur spinels where the covalent overlap causes it to take the low spin (t_{2g}^6, e_g^0) ground state.[2, 5] It therefore has a spin value (S) = 0 and is essentially diamagnetic. This removes the usual complication of magnetic ions on different crystallographic sites and makes this series a promising candidate for the study of tetrahedral site iron ions.

1.1 Crystal Structure

Since the anions are appreciably larger than the metallic ions, the spinel structure can be approximated by a cubic-close-packed array of anions in which the cations occupy certain interstices. For a spinel of the form PQ_2X_4 where P and Q represent cations and X represents the anion, each unit cell contains 8 formula units. The close packing forms 64 tetrahedral interstices and 32 octahedral interstices in each unit cell. Of these available cation sites, in the spinel structure 8 of the tetrahedral holes and 16 of the octahedral holes are occupied.[6] The unit cell is best illustrated by subdividing it into 8 octants as shown in Figure 4.1. The 'A' cubes contain a group A_2X_4 and the 'B' cubes a group B_4X_4 where A and B represent tetrahedral and octahedral sites respectively.

Table 4-1 gives the atomic positions of the atoms in the unit cell. The parameter u determines the anion-cation spacing. It has a value of 3/8 for the ideal structure illustrated in Figure 4.1 in which case each of the anions lies on a cube diagonal (length = $l_d = \frac{\sqrt{3}a}{2}$), ld/4 from the nearest cube vertex. In real spinel compounds the ideal face-centred-cubic lattice deforms and u is usually greater than 0.375. The anions are displaced along the <1 1 1> directions in such a way that the anion tetrahedron in the A cubes is expanded, retaining its cubic symmetry. The B cube octahedrons distort, resulting in trigonal fields

COORDINATES OF THE IONS IN THE A AND B CUBES OF FIGURE 4-1

Tetrahedral cations	Octahedral cations	Anions
0, 0, 0	5/8, 1/8, 1/8	u, u-1/4, u-1/4
		u-1/4, u, u-1/4
	7/8, 3/8, 1/8	u-1/4, u-1/4, u
		u u u
1/4, 1/4, 1/4	5/8, 3/8, 3/8	u+1/2, u-1/4, u-1/4
		u+1/4, u, u-1/4
	7/8, 1/8, 3/8	u+1/4, u-1/4, u
		u+1/2, u u

N.b. For the complete cell, translate as indicated in Figure 4-1 b.

TABLE 4-1: The co-ordinates of the ions in the A and B cubes of Figure 4-1.

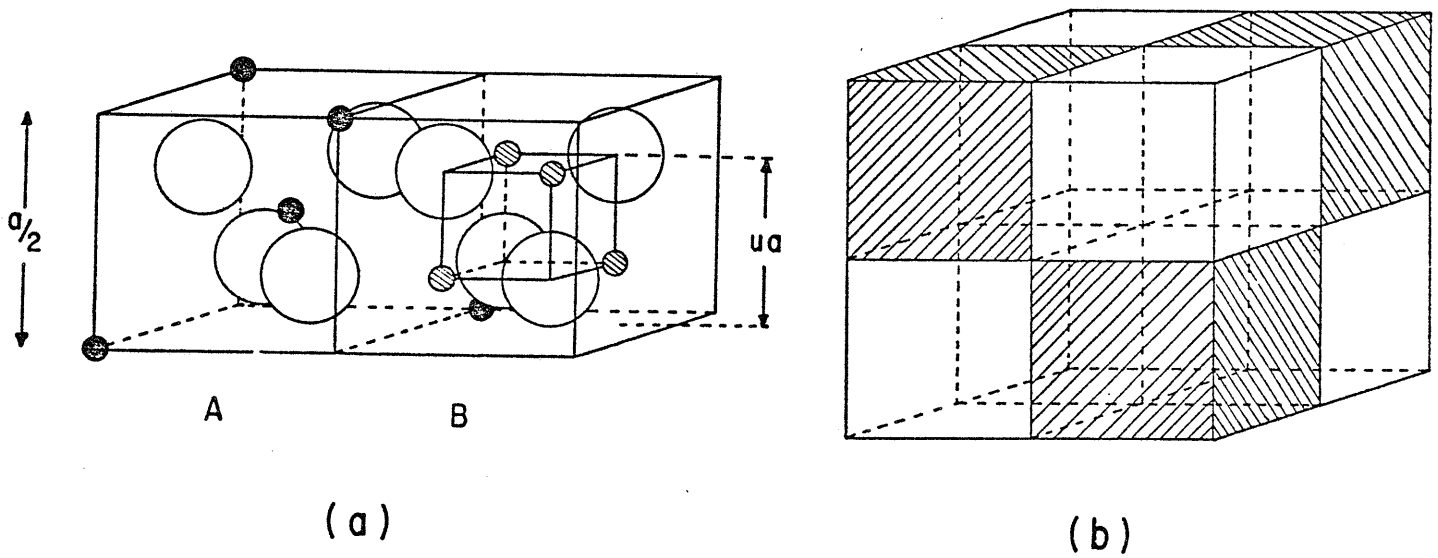

FIGURE 4-1: a) The atomic positions in the A and B cubes: ● represents an A site ion, ◍ a B site ion and ○ a cation.

b) The arrangement of A cubes (□) and B cubes (▨) to complete the unit cell.

superimposed on the B site cubic symmetry. Since this distortion is along different < 1 1 1 > directions at different B-sites in the unit cell, overall cubic symmetry is retained.[7] Large values of u can be expected if the tetrahedral interstices are occupied by comparatively large ions.

The tetrahedral A sites can be further subdivided into two interpenetrating face-centred-cubic lattices as shown in Figure 4-2. A cation on one lattice has four A-site nearest neighbours from the other lattice.

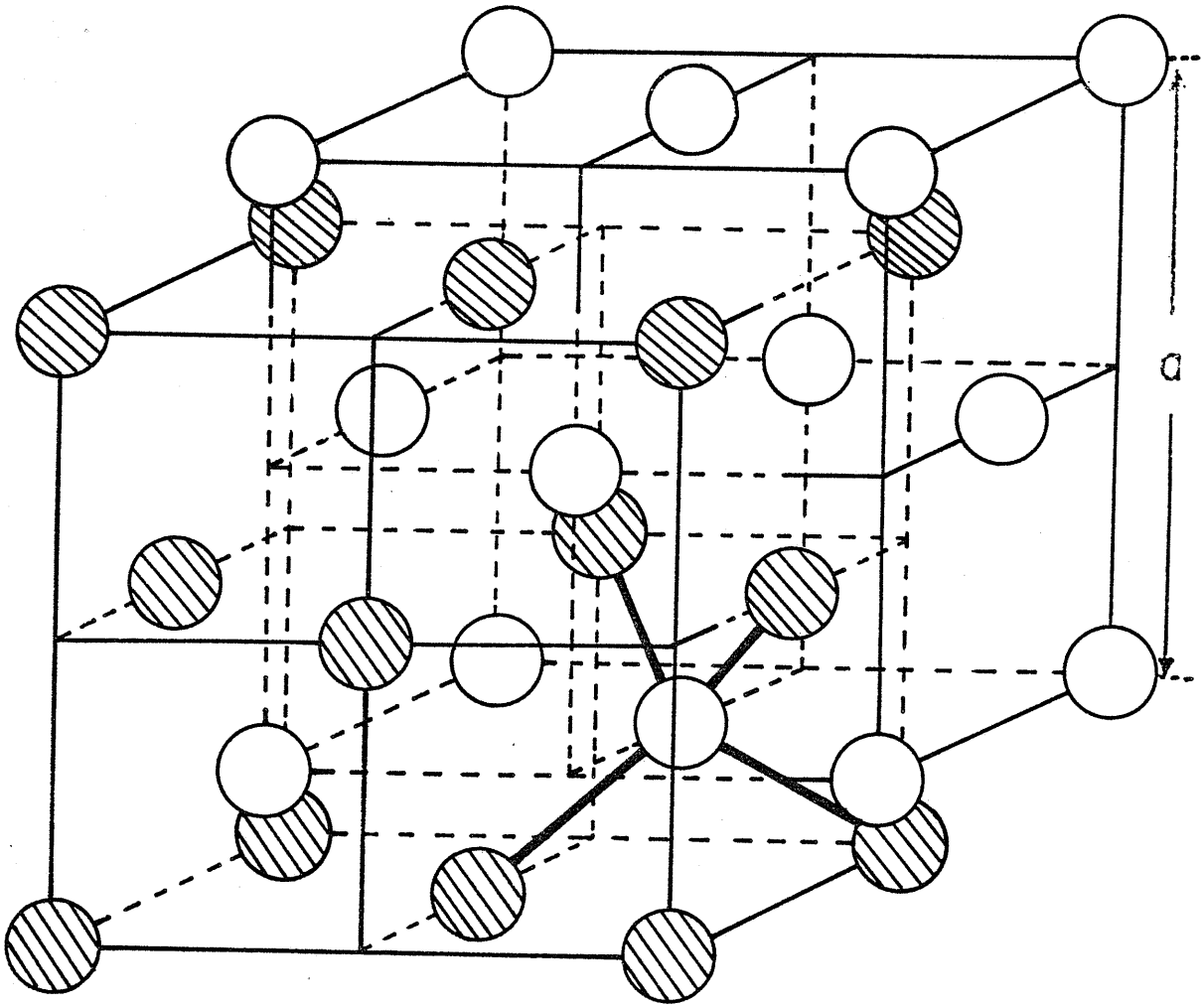

FIGURE 4-2: The spinel A sites subdivided into two interpenetrating face centred cubic sublattices.

The subdivision of the B-sites is more complex, with four B sublattices resulting. Spinels of the form $P\left[Q_2\right]X_4$, where B-site cations are contained in [ ] brackets, are termed normal spinels whereas those of the form $Q\left[PQ\right]X_4$ are given the name inverse spinels.

1.2 Magnetic Structure

There have been a number of studies of the end member of the series $CuRh_2S_4$.[5, 8, 9] It is a metallic compound showing a temperature independent paramagnetism which is believed to originate mainly from the Van Vleck susceptibility of the Rh^{3+} ions.[2, 10] An investigation of $Fe_{0.5}Cu_{0.5}Rh_2S_4$ showed it to be a p-type semiconductor[11] which ordered antiferromagnetically at 140 K. The neutron diffraction results indicated ordering of iron and copper on the A-sites with a spin value S = 1.95 on one site and almost zero for the other. The conclusions were an inversion on A-sites of about 20% with mainly Fe^{3+} ions on one A-site and Cu^{1+} ions on the other. The low-temperature neutron diffraction measurements were explained on the basis of a cubic magnetic cell with a lattice parameter 2a where a is the size of the chemical cell. From the extinction conditions it was deduced that magnetic moments at a distance a were opposite to each other as shown in Figure 4-3. This is 'ordering of the second kind'[12] observed for face-centred-cubic lattices. The dominant interaction is the second-nearest-neighbour (A-B) interaction.[13] The shortest path for this interaction is

Fe-S-Rh-S-Rh-S-Fe and yet the Néel temperature is ~140 K, which makes it the strongest interaction so far observed in a semiconductor for such large distances (9.84 A°).[11]

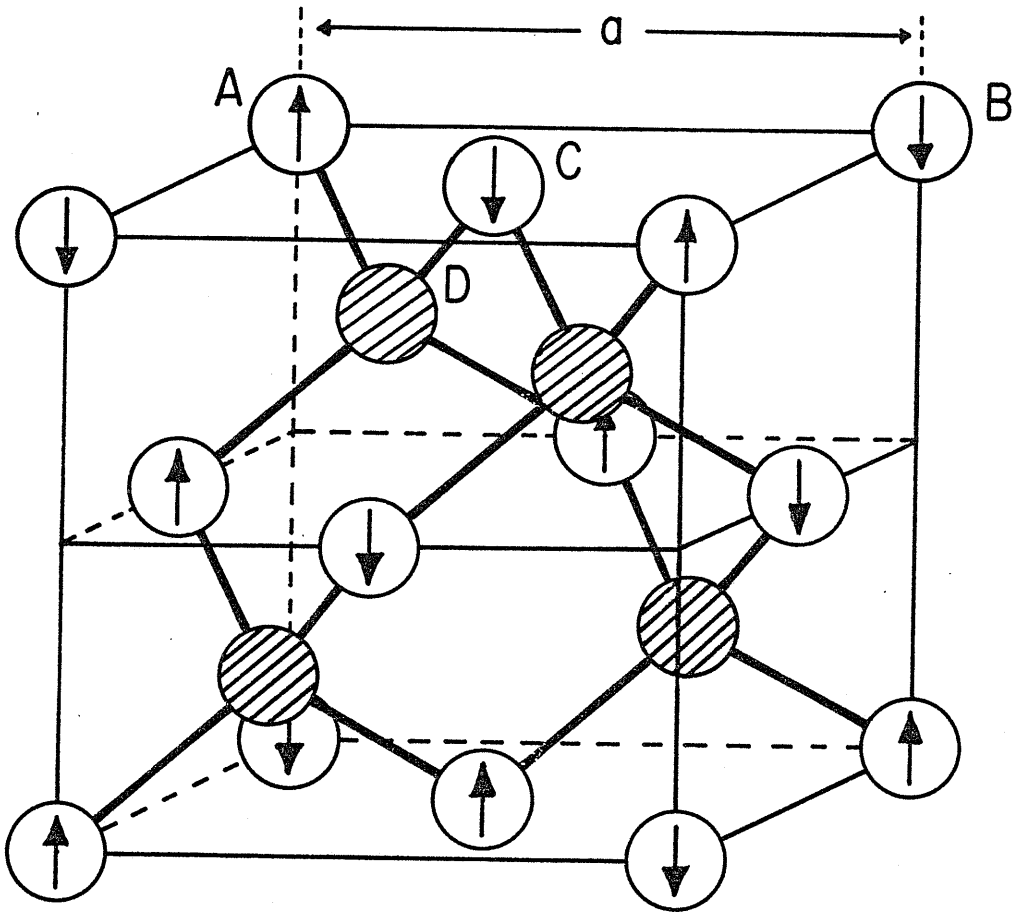

FIGURE 4-3: The antiferromagnetic A site ordering of $Fe_{0.5}Cu_{0.5}Rh_2S_4$.

There have been several unsuccessful attempts to prepare $FeRh_2S_4$.[14, 15] This is surprising since both $Co[Rh_2]S_4$ and $Ni[Rh_2]S_4$ are known to exist in spinel form.[14, 16, 17] Results from an impure sample of $FeRh_2S_4$ produced in our laboratory suggest that it is an antiferro-

magnetic semiconductor, similar to the cobalt spinel, with an ordering temperature of 215 K.[18] The sample however was not a single phase and theoretical fits to the Mössbauer data were unsatisfactory. It was concluded that the iron was in the Fe^{2+} valence state which led the author to propose $Fe^{2+}_{0.5}Cu^{2+}_{0.5}Rh^{3+}_{2}S^{2-}_{4}$ for the valence states in the middle member of the series.

Considerable controversy exists over the allocation of a valency state to copper in the copper containing Rh and Cr sulphur spinels.[8, 19, 20] The main disagreement seems to lie in the positioning of the copper d-bands with respect to the top of the valency band in the various energy schemes suggested for these compounds.[19] A Mössbauer investigation of the semiconducting $Fe_{0.5}Cu_{0.5}Rh_2S_4$ should provide direct evidence for the valence state of the iron.

2. Sample Preparation

The series of compounds was prepared by heating stoichiometric quantites of the elements in evacuated quartz ampules. Since the metals were in the form of easily oxidized fine powders it was necessary to reduce them by heating in a stream of hydrogen gas immediately prior to weighing the samples. The quartz ampules were cleaned, and heated to above 1000°C under vacuum to remove absorbed gases from the inner walls of the tube. All the elements used were 99.999% pure.

The weighed samples were sealed in evacuated quartz ampules and placed in the furnace at room temperature. Due to the high vapour pressure of the sulphur, the ampules were heated slowly to 400°C and held there for twelve hours before heating to higher temperatures. Initially, sulphur vapour was clearly visible inside the tube but this disappeared after 3 days at 1050°C. The samples were then allowed to cool to room temperature. Attempts to raise the temperature to 1050°C without the 12-hour anneal at 400°C often resulted in cracks in the quartz tubing and occasionally caused the ampules to explode. After the initial heat treatment the resultant sintered powder was ground for several minutes, pressed into a pellet and resealed in an evacuated ampule. The above heat treatment was repeated, without the initial anneal at 400°C, and the samples then examined with the X-ray diffractometer.

Samples with $x < 0.7$ i.e. those containing substantial amounts of copper, were found to be single phase spinels. However the iron rich compounds ($x \geqslant 0.7$) showed extra lines in the X-ray patterns and the high angle lines were substantially broadened. These samples were subjected to a third firing at 1050°C which reduced the intensity of the extra lines and sharpened the high angle lines of the diffractometer patterns. Further heat treatment produced similar results, until single phase spinels were prepared for x values $\leqslant 0.94$.

It was increasingly difficult to produce single phase samples as the copper content was reduced, and it was not possible to prepare $FeRh_2S_4$ as a single phase spinel using this method. It has been suggested[15] that this may be due to the nobility of the rhodium. If this is the case then it appears that copper acts as a catalyst for the formation of the spinel structure. However, since difficulties are encountered for some of the transition metal (Me) $\left[Rh_2 \right] S_4$ spinels (Me = Cr, Mn, Zn, Cd) and not for others (Me = Cu, Co, Ni),[14] this explanation seems unlikely.

Mössbauer samples were prepared as above, but due to the large non-resonant absorption of the Rh, iron enriched with ^{57}Fe had to be used. The expense of the enriched isotope limited the weight of each Mössbauer sample to less than 100 mg and so weighing errors became important when identifying a sample by its x value. To check for weighing errors, an attempt was made to find the relative iron to

copper ratios of the series of compounds using the X-ray fluorescence equipment. Although good agreement was found for the non-enriched samples, reproducible results were never obtained from the material used for the Mössbauer absorbers, presumably due to the small amount of sample available. An alternative method was devised to estimate the iron to copper ratio in these small samples.

To produce a uniform thickness (mg of $Fe_xCu_{1-x}Rh_2S_4/cm^2$) over the area of the Mössbauer absorber (approximately 3 cm^2) when using a small amount of sample, the compound was mixed with boron nitride powder and clamped between two thin Beryllium plates. Enriched absorbers contained approximately 0.5 mg/cm^2 of ^{57}Fe.

3. X-ray Measurements

The high melting points of all members of this series of compounds prevented any attempt to produce single-crystal samples. The X-ray work was therefore limited to an investigation using powder techniques. Ni-filtered-Cu radiation was used for both diffractometer measurements and Debye-Scherrer photographs.

The neutron diffraction investigation[11] of $Fe_{0.5}Cu_{0.5}Rh_2S_4$ indicated a 1:1 ordering of iron and copper on the A_1- and A_2- sites as described earlier. A-site ordering of this type surrounds the atoms on one A-site with four nearest A-site neighbours from the other site arranged in tetrahedral co-ordination. The cubic symmetry of the sites is thus retained. The presence of the (200)- and (420)-superstructure reflections characteristic of this ordering, was not detected using copper radiation, due to the small difference in scattering power of the copper and iron atoms. A similar result was obtained by Lotgering et al.[20] for $Fe_{0.5}Cu_{0.5}Cr_2S_4$. However in cases such as this where two ions have similar scattering powers it is sometimes possible to take advantage of the depression of the scattering factor of an ion close to its K absorption edge.[21]

Table 4.2 shows the reduction in the scattering factors of iron and copper as a function of λ/λ_k where λ_k is the wavelength at the K absorption edge (= 1.742 Å for iron and 1.380 Å for copper), and λ is the wavelength of the

incident radiation. These results were taken from reference 21 and are the averages of values reported in a number of experimental papers. It can be seen that cobalt or zinc K_α radiation should provide good results. Since iron already has the smaller scattering factor, it would be preferable to depress this further and hence iron filtered cobalt radiation was used to search for the superlattice lines indicating A-site ordering.

TARGET ELEMENT	COPPER		IRON	
	λ/λ_k(Cu)	Depression of the Scattering Factor	λ/λ_k (Fe)	Depression of the Scattering Factor
Cr	1.66		1.32	1.0
Mn	1.52		1.21	1.3
Fe	1.40	0.9	1.11	2.0
Co	1.30	1.0	1.02	3.9
Ni	1.20	1.3	0.95	3.4
Cu	1.12	1.8	0.88	1.8
Zn	1.04	3.2	0.83	0.9
Mo	0.51	0.0	0.41	0.0

TABLE 4-2: The reduction in the scattering factors of copper and iron for different wavelength radiation.

The (420) superlattice line was found to be present in samples within the composition range $0.45 \leqslant x \leqslant 0.7$ and though very weak in $Fe_{0.7}Cu_{0.3}Rh_2S_4$, it does show that the

majority of copper ions still occupy only the one A sublattice. The (420) reflection was absent from the X-ray diffractometer tracings of all of the samples using any of the other X-ray tubes available in the laboratory (Cr, Fe, Cu and Mo).

Debye-Scherrer X-ray photographs of samples with $x \leq 0.94$ were indexed on a spinel unit cell as shown for $Fe_{0.5}Cu_{0.5}Rh_2S_5$ in Table 4-3. Intensities were measured from a diffractometer tracing for reflections with $2\theta < 130^{o}$ (where θ is the Bragg angle) but above this angle they had to be estimated from the photographs. Figure 4-4 is a reproduction of the high angle lines of Debye-Scherrer photographs from several members of the series and indicates a systematic change in unit-cell dimension with x-value. In order to investigate this variation, accurate values were required for the lattice parameters of the samples. The usual method for finding the lattice parameter (a) of a cubic crystal is to find a value $a(\theta)$ from each reflection with $2\theta > 90^{o}$, and to plot these values against the Nelson-Riley function $\frac{1}{2}\left\{\frac{\cos^2\theta}{\sin\theta} + \frac{\cos^2\theta}{\theta}\right\}$.[22] This function was developed such that a graph of $a(\theta)$ against the Nelson-Riley function produces a straight line which can be extrapolated to $\theta = 90^{o}$ (N.R. function = 0) to give an accurate value of a. When drawing this line, a heavy bias is given to the more accurate high angle measurements. In fact the highest angle value of $a(\theta)$ usually determines the position of the line, and the remaining measurements are used to estimate

	h	k	l	d_{obs} (A)	d_{calc} (A)	Intensity
	1	1	1	5.6586	5.6815	4
	2	2	0	3.4716	3.4792	2
	3	1	1	2.9640	2.9671	10
	2	2	2	2.8347	2.8407	1
	4	0	0	2.4558	2.4602	6
	3	3	1	2.2523	2.2576	1
	4	2	2	2.0035	2.0087	1
5 1 1	3	3	3	1.8909	1.8938	4
	4	4	0	1.7368	1.7396	6
	4	4	2	1.6477	1.6401	1
	6	2	0	1.5540	1.5559	1
	5	5	3	1.4992	1.5007	1
	6	2	2	1.4807	1.4835	1
	4	4	4	1.4192	1.4204	1
7 1 1	5	5	1	1.3761	1.3780	1
	6	4	2	1.3136	1.3150	1
7 3 1	5	5	3	1.2796	1.2811	2
	8	0	0	1.2289	1.2301	1
	8	2	2	1.1582	1.1597	1
7 5 1	5	5	5	1.1358	1.1363	1
	8	4	0	1.0990	1.1002	2
7 5 3	9	1	1	1.07915	1.08015	1
	9	3	1	1.03094	1.03158	1
	8	4	4	1.00294	1.00435	3
7 5 5	9	3	3	0.98834	0.98902	1
7 7 3	9	5	1	0.95064	0.95133	2
	9	5	3	0.91718	0.91764	1
	7	7	5	0.88683	0.88729	2
	8	8	0	0.86944	0.86979	3
	9	5	5	0.85945	0.85978	3
	9	7	3	0.83447	0.83467	3
	10	6	2	0.83166	0.83168	1
12 0 0	8	8	4	0.81990	0.82004	3
	7	7	7	0.81147	0.81164	1
	10	6	4	0.79805	0.79818	1
	9	7	5	0.79037	0.79042	3
	12	4	0	0.77791	0.77797	3

TABLE 4-3: X-ray powder diffraction data for $Fe_{0.5}Cu_{0.5}Rh_2S_4$.

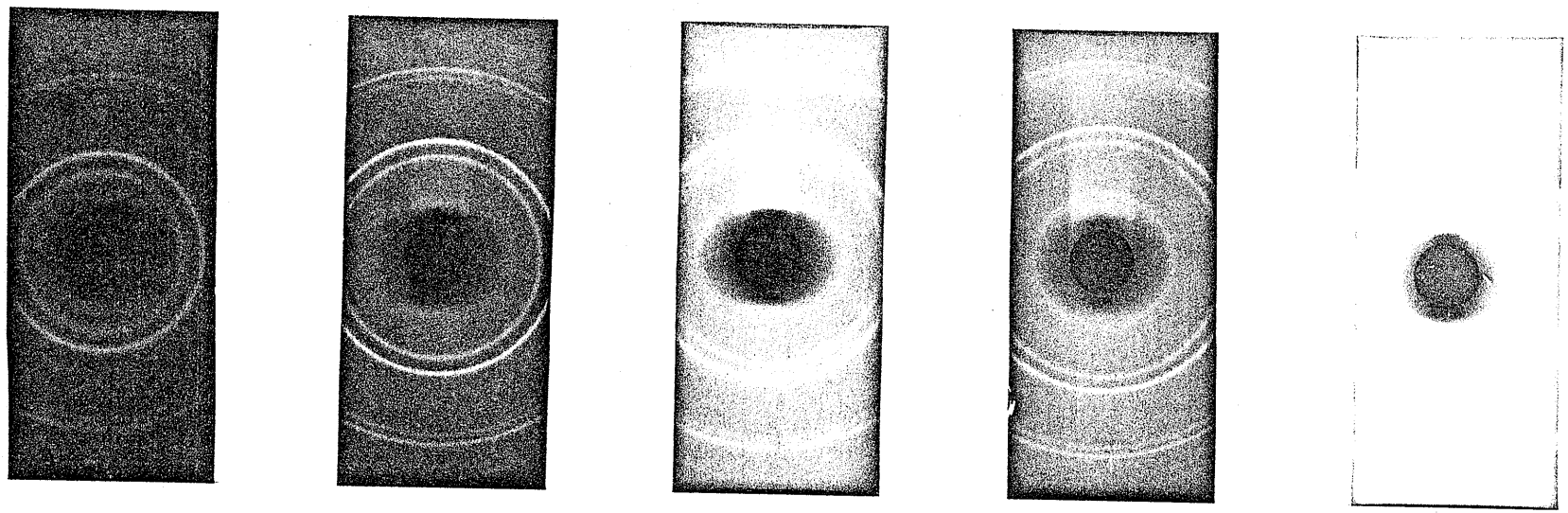

$Fe_{0.19}Cu_{0.81}Rh_2S_4$ $Fe_{0.5}Cu_{0.5}Rh_2S_4$ $Fe_{0.65}Cu_{0.35}Rh_2S_4$ $Fe_{0.8}Cu_{0.2}Rh_2S_4$ $Fe_{0.94}Cu_{0.06}Rh_2S_4$

FIGURE 4-4: A reproduction of the high angle lines from several members of the series $Fe_xCu_{1-x}Rh_2S_4$.

the gradient. This is a time-consuming method if a large number of samples are being measured at one time.

We already have an estimate of the error in d as a function of θ

$$\frac{\Delta d}{d} = -\cot\theta\,\Delta\theta$$

Since $d = \dfrac{a}{\sqrt{h^2+k^2+l^2}}$ for a cubic crystal, we also know the error in $a(\theta)$ as a function of θ

$$\frac{\Delta a}{a} = -\cot\theta\,\Delta\theta$$

A computer program was therefore written which fitted a straight line to a plot of $a(\theta)$ against $\frac{1}{2}\left\{\frac{\cos^2\theta}{\sin\theta} + \frac{\cos^2\theta}{\theta}\right\}$ using a least squares method with a bias of $\cot\theta$ to the deviation $\Delta a(\theta)$.

A copy of the program is given in the Appendix. It provides a quick and systematic method for finding accurate lattice parameters of cubic crystals. If required, the program could easily be extended to plot out the graph with the fitted line. However in its present short form, up to five sets of data can be run at one time before the page limit of the IBM 360 student terminal is exceeded. The output gives $a(\theta)_{observed}$ and $a(\theta)_{calculated}$ so that errors are immediately visible and results can be checked by running the program separately for measurements from $K\alpha_1$ and $K\alpha_2$ radiation. Results for the series are shown in

Figure 4-5 and indicate a linear variation of a with x.

Having established the variation of the cell dimension as a function of x, the composition of the Mossbauer samples was determined by measuring their lattice parameters and comparing them with the calibration curve obtained from the large non-enriched samples. The large deviations in x introduced by weighing errors in the smaller samples can be seen in Figure 4-5. For example the attempt to produce a sample enriched with ^{57}Fe with an x value of 0.5 resulted in a sample of the composition $Fe_{0.46}Cu_{0.54}Rh_2S_4$. Although this method does not ensure that the number of (Fe + Cu) atoms is exactly one half of the number of Rh atoms, no evidence was found to question the stoichiometry of these samples.

Later magnetization and Mössbauer measurements suggested the possibility of a crystallographic distortion in the iron rich members of the series as the temperature was reduced. To check for this, the low temperature attachment to the diffractometer was used to record X-ray tracings at a number of temperatures from 4.2 K to room temperature. No evidence of any crystallographic change was found, other than the contraction of the lattice as the temperature was lowered. No extra lines or line broadening could be detected and the linear variation of the lattice parameter with x was retained at all temperatures. The results at 77 K are also shown in Figure 4-5. These measurements are not as accurate as those taken at room temperature for which the Debye-Scherrer camera was used. The equipment had to be realigned each time the

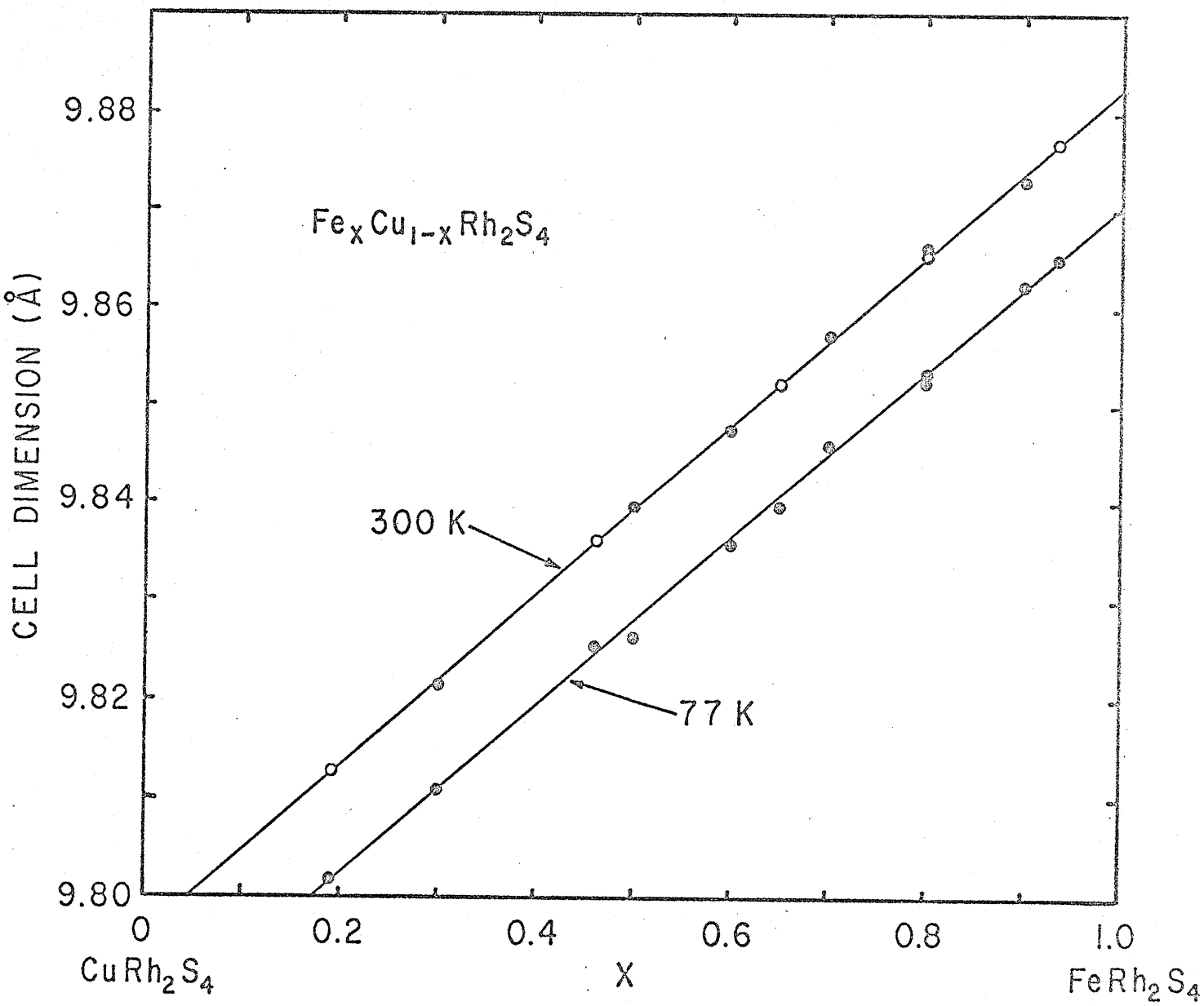

FIGURE 4-5: The variation of the cell dimension with concentration. Open circles represent samples enriched with Fe^{57}, placed onto the room temperature calibration curve.

sample was changed therefore a room temperature trace was always recorded and checked with the regular diffractometer and Debye-Scherrer results. Room temperature 2θ values (where θ is the Bragg angle) were consistently 0.3^{o} lower when the low-temperature system was used, and so measurements taken with this equipment were corrected by this amount before the lattice parameters were calculated. However equipment design limited measurements to $2\theta \leq 130^{o}$ and so larger errors must be expected on the cell dimensions at lower temperatures.

4. Magnetization Measurements

Magnetization measurements in the temperature range 4.2 to 300 K indicated antiferromagnetic order for all members of the series. The susceptibility of all of the samples was very small especially at higher temperatures. In fact reproducible results could not be obtained above room temperature due to the relatively high background signal and increased noise produced by the magnetometer furnace.[15] Even when using the low temperature cryostat, the original fibre glass sample rod had to be replaced by a quartz extension tube, since the low temperature signal produced by the glass fibre was larger than the signal from some of the samples.

Figure 4-6 shows a plot of the inverse molar susceptibility (χ_m^{-1}) against temperature for samples of $Fe_xCu_{1-x}Rh_2S_4$ with $0.3 \leqslant x \leqslant 0.9$. Measured values of C_m and θ are shown in Table 4-4 together with the theoretical spin only values calculated for Fe^{3+} and Fe^{2+}. The Van Vleck contribution to the susceptibility from Rh^{3+} ions in spinel octahedral sites was estimated by Lotgering[2] to be 3.8×10^{-4} emu/Oe mole of $A\left[Rh_2^{3+}\right]S_4$. Values of C_m and θ with this correction are also given in Table 4-4.

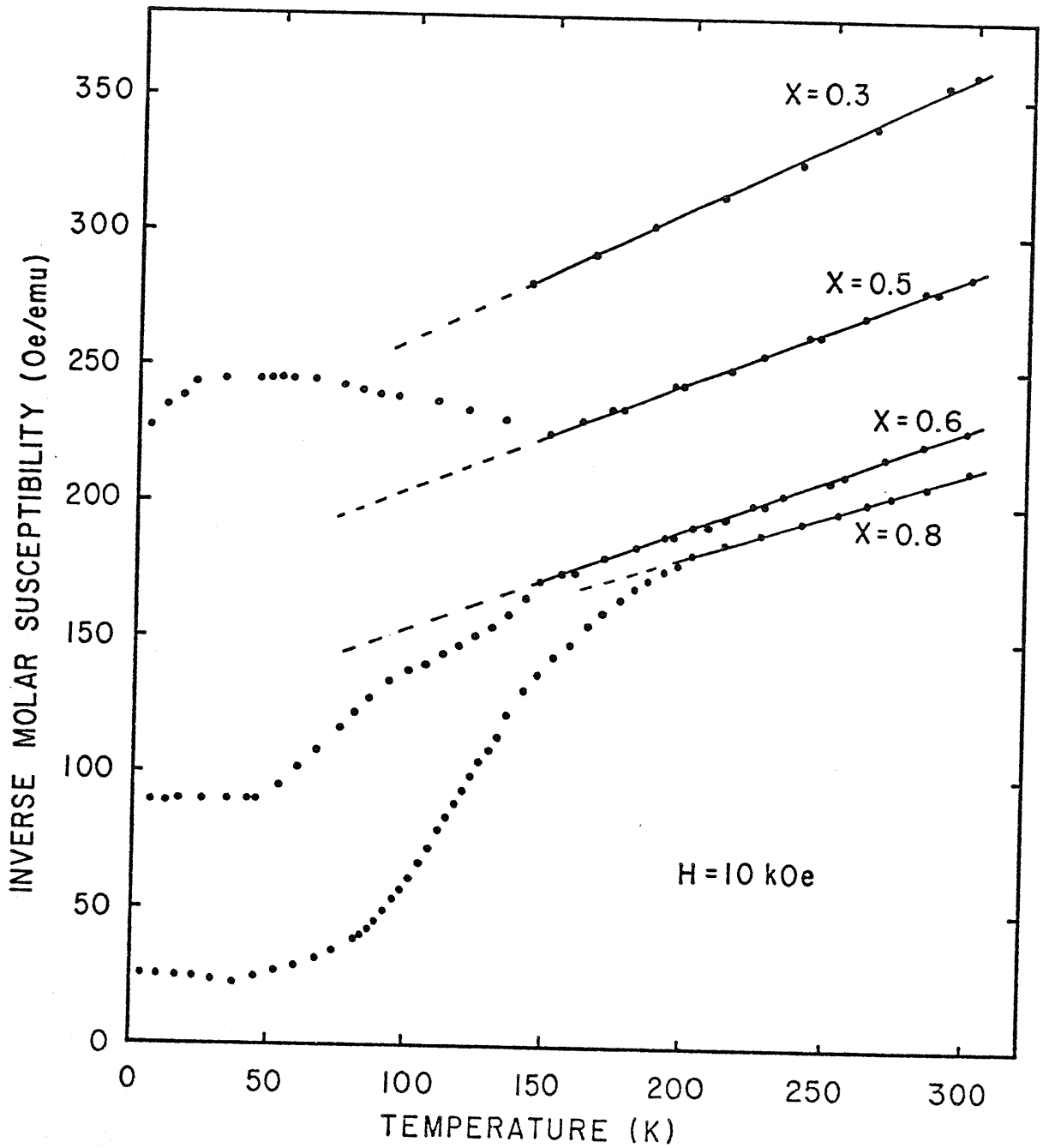

FIGURE 4-6: The temperature dependence of the inverse molar susceptibility for samples of $Fe_xCu_{1-x}Rh_2S_4$.

X	Observed				Calculated		
			with Van Vleck correction				
	C_m	θ	C_m	θ	$C_m(Fe^{3+})$	$C_m(Fe^{2+})$	$C_m(Fe^{3+}:Fe^{2+})$
0.3*	1.97	-410	1.57	-355	1.31	0.90	1.31
0.5	2.50	-412	2.09	-367	2.19	1.50	2.19
0.6	2.68	-310	2.34	-284	2.63	1.80	2.33
0.7	2.78	-278	2.46	-256	3.07	2.10	2.49
0.8	3.06	-355	2.69	-326	3.50	2.40	2.70
0.9	3.45	-427	3.02	-393	3.93	2.70	2.82
1.0					4.38	3.00	3.00

*Corrected for small ferromagnetic impurity.

TABLE 4-4: Magnetization data for the series of compounds $Fe_xCu_{1-x}Rh_2S_4$.

For $x > 0.5$, the iron cannot remain in the Fe^{3+} state proposed by Plumier and Lotgering[11] for the middle member of the series unless we have holes associated with the anion lattice as in the case of Fe_7Se_8.[23] If the charge balance is preserved via the iron ions, then with an ionic model we would have a compound of the form $\left(Fe^{2+}_{(1-y)}Fe^{3+}_{y}\right)_x Cu^{1+}_{(1-x)} \left[Rh_2^{3+}\right] S_4^{2-}$. The final column of Table 4-4 shows the expected C_m values with the Fe^{3+}:Fe^{2+} ratio required for charge balance. The agreement with the Van Vleck corrected experimental values is quite good and there is certainly a

trend towards Fe^{2+} as the iron content is increased. It should be noted however that the experimental errors on the C_m values become much larger for the iron-rich members of the series since the Curie-Weiss Law is obeyed over a smaller region of our experimental temperature range.

Excluding the middle member of the series, the Néel points of the different samples are not obvious from the curves of Figure 4-6. $Fe_{0.5}Cu_{0.5}Rh_2S_4$ has a single sharp minimum in its χ_m^{-1} vs.T curve at 135 ± 5 K and obeys the Curie-Weiss Law above this temperature. The other members of the series however, deviate from the Curie-Weiss Law at temperatures up to 150 K above the sharp breaks in the curves as shown for x = 0.6 and x = 0.8 in Figure 4-6. This behaviour is more evident in Figure 4-7 which is a graph of χ_m against T. For $x \geq 0.6$, the peaks fall between 35 and 45 K. Whether the peaks occur at the Néel point, or whether in fact the samples begin to order at the temperature at which the Curie-Weiss Law breaks down required further investigation. It is unlikely that short range order could cause deviations from the Curie-Weiss behaviour at temperatures as high as five times the ordering temperature. Similar results were found by Lotgering[20] from magnetization measurements on the series of compounds $Co_xCu_{1-x}Rh_2S_4$. He also indicated that there was a possibility of spin ordering in the intermediate region.

The copper-rich compound $Fe_{0.3}Cu_{0.7}Rh_2S_4$ appears to have a small soft ferromagnetic component superimposed on

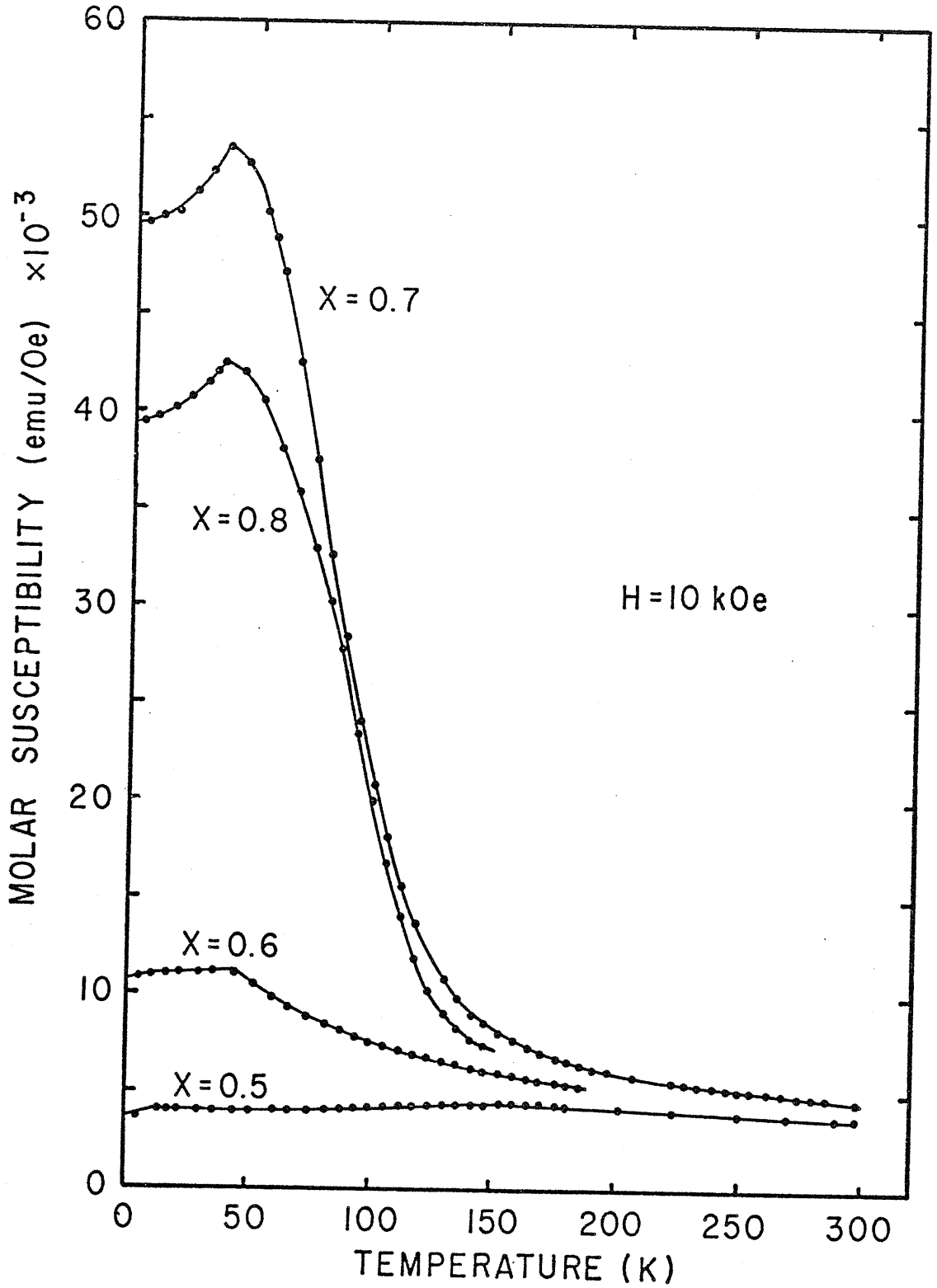

FIGURE 4-7: The temperature dependence of the molar susceptibility for the series $Fe_xCu_{1-x}Rh_2S_4$.

the antiferromagnetic background at all temperatures. The magnitude of this moment is remarkably constant at ~25 emu/mole over the whole temperature range. This is a very small value, equivalent to approximately 0.005 μ_B /formula unit and its most likely origin is some small ferromagnetic impurity, such as unreacted iron, too small to be observed in either Mössbauer or X-ray experiments. This moment was subtracted from all measurements recorded from $Fe_{0.3}Cu_{0.7}Rh_2S_4$. Spin clustering of iron ions on the A-sites could explain this small ferromagnetic component. (Clustering would also explain the high Curie constant calculated from susceptibility results which included this moment). However, since the component is present at all temperatures we would require the clusters to order above 300 K, which seems unlikely when the maximum ordering temperature in the series occurs at 138 K.

$Fe_{0.3}Cu_{0.7}Rh_2S_4$ has an abnormally high Néel temperature of 130 ±10 K, above which it follows a Curie-Weiss Law. (The Néel point is indistinct using the data from Figure 4-6 but it is later verified by Mössbauer measurements). The high Néel temperature in a compound with such a low concentration of magnetic ions points to indirect interactions via band polarization.[2] This transition to metallic behaviour as the iron content is reduced must be expected, since the end member $CuRh_2S_4$ is known to show p-type metallic conduction.[25] The possibility of a moment associated with the copper lattice in the iron deficient compounds

(i.e. localized Cu^{2+} ions) is discounted since there is no evidence of any long range magnetic order in $CuRh_2S_4$, and its susceptibility data is well explained by diamagnetic, Pauli paramagnetic and Van Vleck contributions.[2]

As described earlier, the spinel A-sites may be subdivided into A_1 and A_2-sites, where A_1 sites represent those A-sites occupied by iron ions in $Fe_{0.5}Cu_{0.5}Rh_2S_4$ and A_2 sites represent the interpenetrating face-centred-cubic A sublattice occupied by copper ions. Immediately iron ions occupy both A_1 and A_2 sites, very strong competing antiferromagnetic superexchange interactions exist:

1. The $A_1 \rightarrow A_1$ long range (Fe-S-Rh-S-Rh-Fe) superexchange interaction proposed by Lotgering for $Fe_{0.5}Cu_{0.5}Rh_2S_4$.[11] As the iron content is increased however the measured Curie constants (and later Mössbauer measurements) show a change in the valence state of the iron from Fe^{3+} to Fe^{2+}. From the sharp drop in Néel temperature between $Fe_{0.5}Cu_{0.5}Rh_2S_4$ and $Fe_{0.6}Cu_{0.4}Rh_2S_4$ it would appear that the change in electron distribution caused by the change in valence state, seriously weakens this superexchange coupling.

2. The $A_1 \rightarrow A_2$ (F-S-Rh-S-Fe) antiferromagnetic interaction which dominates in the cobalt-rhodium spinels, $CoRh_2O_4$ [24] and $CoRh_2S_4$.[20] The A_1-A_2 interaction is much stronger in the more covalent sulphide (T_N = 400 K) than in the oxide (T_N = 27 K). In these compounds, low spin Rh^{3+} ions also occupy the B-sites and the lattice parameters are very similar to those of the Fe-Rh series. The consequence of

this strong interaction in the cobalt compounds is a simple antiferromagnetic ordering between A-site nearest neighbours i.e. an antiparallel alignment of the A_1 and A_2 sublattices.

The presence of these strong competing interactions as the iron content is increased causes a number of interesting effects, the most visible of which being the displaced hysteresis loops described below.

The M-H curves of Figure 4-8 were recorded from samples of $Fe_{0.3}Cu_{0.7}Rh_2S_4$ and $Fe_{0.5}Cu_{0.5}Rh_2S_4$ at 4.2 K. The small ferromagnetic component can be seen on the curve from the iron-deficient sample. The samples were cooled to 4.2 K in zero applied field and the curves show neither hysteresis nor asymmetry about the origin. Identical results were obtained from samples cooled to 4.2 K in an external field of 18 kOe. This was not the case for samples containing an excess of iron ($x > 0.5$). All such samples exhibited hysteresis at 4.2 K and when cooled to 4.2 K in an external field the resulting hysteresis loops were displaced along the magnetic axis. This is shown in Figures 4-9, 10, 11 and 12, where the curves symmetric about the origin were obtained by cooling the sample from room temperature to 4.2 K in the absence of an applied field and the asymmetric curves from samples cooled in 18kOe.

As noted earlier, X-ray measurements showed clear evidence for some degree of ordering of copper and iron ions on A_1 and A_2 sites in the composition range $0.45 \leqslant x \leqslant 0.7$.

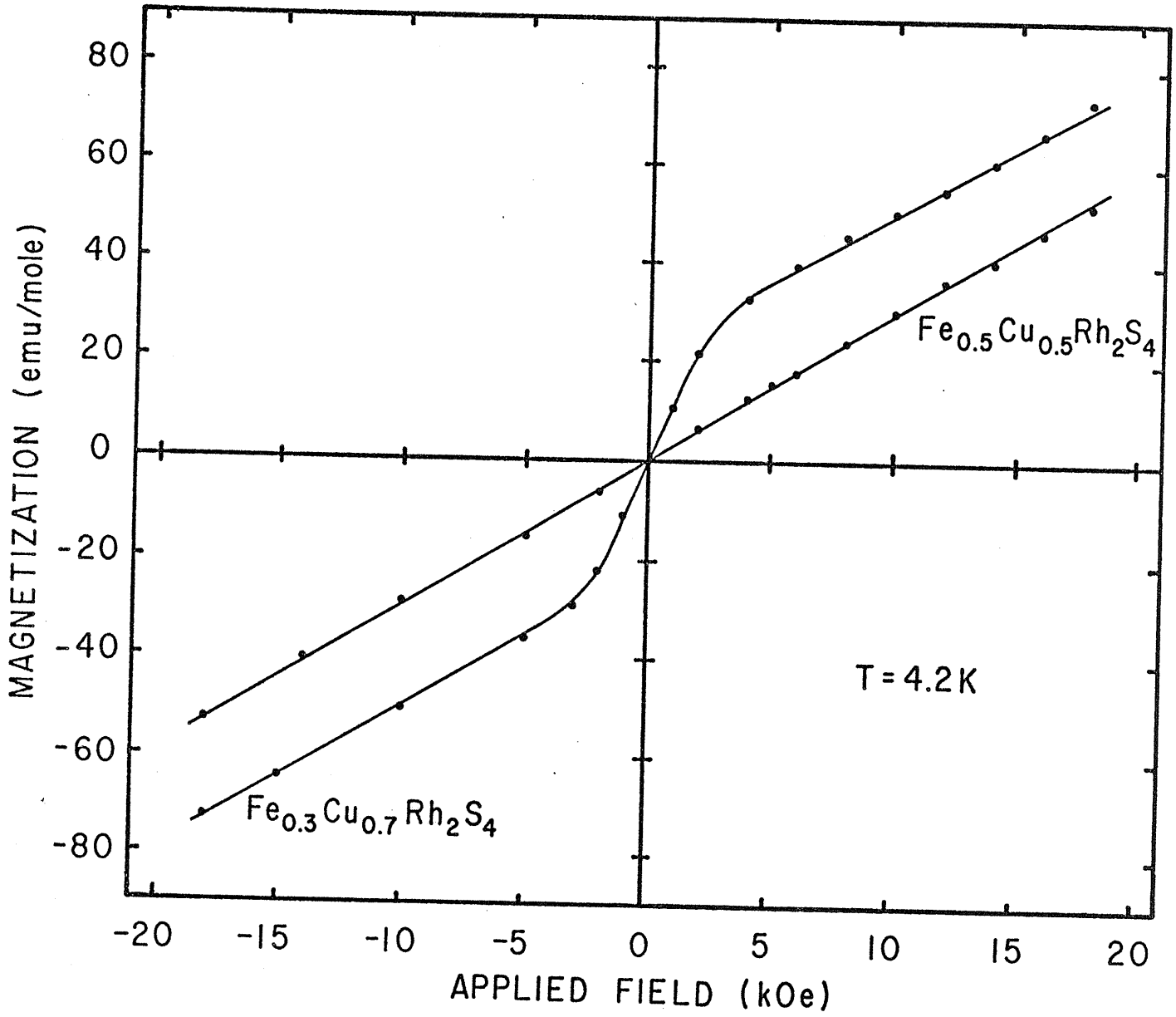

FIGURE 4-8: The magnetization as a function of applied field at 4.2 K for $Fe_{0.5}Cu_{0.5}Rh_2S_4$ *and* $Fe_{0.3}Cu_{0.7}Rh_2S_4$.

It may therefore be assumed that $Fe_{0.6}Cu_{0.4}Rh_2S_4$ has the majority of iron ions ordered antiferromagnetically on the A_1 sublattice, with the excess replacing copper ions on the A_2 sublattice. With this small number of excess ions it is unlikely that there will be interactions between iron ions on the A_2 sites. As can be seen from Figure 4-9, the result of the interaction between the excess spins and the antiferromagnetic A_1 sublattice is to align the spins in such a direction so as to produce a zero net moment. This is not surprising when we consider that we are dealing with a cubic crystal with many equivalent directions. Whether in fact we are witnessing simple Néel antiferromagnetism (antiparallel alignment) on the A_2 sites or whether the isolated excess spins are aligned along a number of equivalent directions so as to produce zero moment can not be determined from our present measurements. Both cases would produce the observed results, provided the majority of the excess spins are locked into position at 4.2 K with a sufficient energy barrier to prevent realignment by the 18kOe applied field. If this were not the case a larger hysteresis than that observed in Figure 4-9 would be expected.

With the magnetic structure described above, two possible mechanisms would explain the displaced hysteresis curve of the high field cooled sample. The first requires that the isolated spins be strongly coupled to the antiferromagnetic lattice, but with a number of magnetically

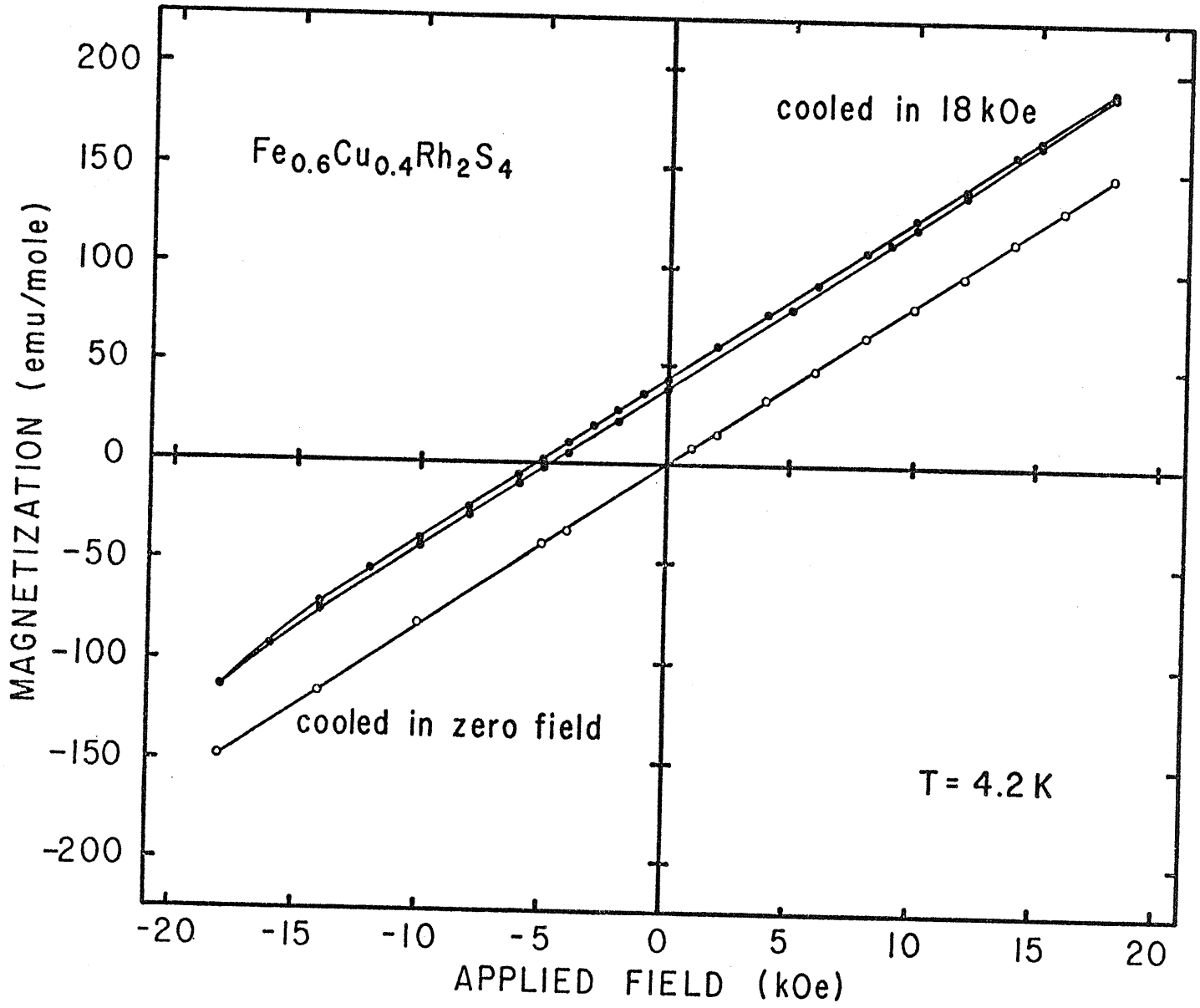

FIGURE 4-9: The magnetization as a function of applied field at 4.2 K for $Fe_{0.6}Cu_{0.4}Rh_2S_4$.

equivalent directions. At temperatures near the ordering or blocking temperature (T_B) of the excess spins, the coupling to the A_1 sublattice and hence the energy barrier between these equivalent directions will be small. As we cool through the blocking temperature in an external field, the (magnetic moments of the excess) spins will first align parallel to the applied field, then, as the temperature is further lowered and the exchange energy becomes comparable to the energy of interaction with the field, the spins will relax towards the nearest easy direction of magnetization. When the field is removed at low temperatures, the spins remain preferentially aligned with a net moment in the field direction. From the small hysteresis in the zero field cooled sample, we know that 18kOe is insufficient to overcome the energy barrier between the equivalent easy directions of the majority of spins at 4.2 K. The original antiferromagnetic M-H curve of the zero field cooled $Fe_{0.6}Cu_{0.4}Rh_2S_4$ will therefore have a very hard ferromagnetic component superimposed, producing the displaced loop of Figure 4-9.

For the second mechanism it is assumed that a lowest energy state exists for a particular orientation of each excess spin with respect to the A_1 sublattice. However the magnetic ordering proposed by Lotgering[11] (Figure 4-3) requires only that the alignment of the A_1 magnetic moments be along one of the set of $[100]$ directions. If the $Fe_{0.6}Cu_{0.4}Rh_2S_4$ sample is cooled to below T_N in the absence

of an applied field, all of the antiferromagnetic orientations in the powdered crystalites will be equally populated. Cooled in an applied field however, the excess magnetic moments on the A_2 sites will be initially in the field direction and the surrounding antiferromagnetic regions will have an orientation indirectly determined by the applied field through exchange coupling to the excess spins. When the applied field is removed at low temperatures, the excess spins will remain coupled to the preferentially aligned antiferromagnetic lattice whose orientation is not directly affected by the application of 18kOe. The high field cooled M-H curve will therefore have a hard ferromagnetic component superimposed on the antiferromagnetic background giving a displaced hysteresis loop.

As the iron content is increased i.e. more excess spins, the remanent moment of the high field cooled state will increase. However, since the superexchange coupling of the original A_1 lattice will be further distorted by the changing electron distribution of the iron ions, a weakening of the locking mechanism will also result. It is therefore expected that with an increased iron content, the zero field cooled M-H curve at 4.2 K will show an increased hysteresis, since the 18kOe field will now be strong enough to overcome more of the energy barriers between equivalent orientations. This increased hysteresis is evident in the M-H curve of $Fe_{0.7}Cu_{0.3}Rh_2S_4$ shown in Figure 4-10.

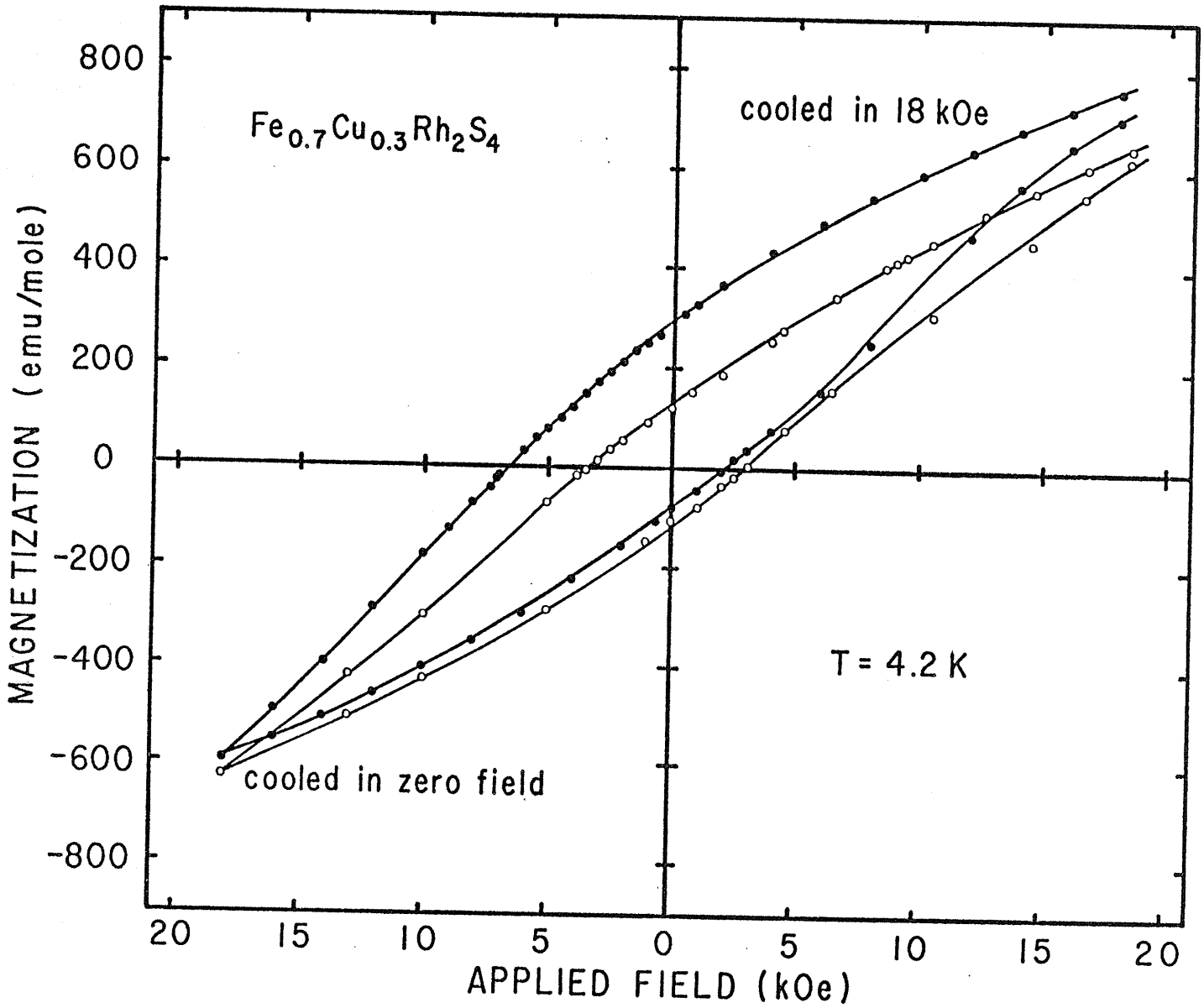

FIGURE 4-10: The magnetization as a function of applied field at 4.2 K for $Fe_{0.7}Cu_{0.3}Rh_2S_4$.

As the iron content is increased further, we must consider the most probable magnetic structure of the end member, $FeRh_2S_4$. Although this compound has never been produced as a single phase spinel, magnetization and conductivity measurements on a sample showing ~5% impurity[15] suggest it is an antiferromagnetic semiconductor with the same magnetic structure as $CoRh_2S_4$.[9, 10] (i.e. Fe spins on A_1 sites aligned antiparallel to spins on A_2 sites). In this case, A_1-A_2 interactions will begin to dominate as the iron content is increased. The susceptibility at temperatures below T_N will peak as the A_1 - A_1 and A_1 - A_2 interactions become comparable. From the susceptibility against temperature curves of Figure 4-7 this appears to occur in the region $0.6 < x < 0.8$.

In the composition region $0.7 < x < 1.0$, the magnetic ordering will be complex. The domination of the A_1-A_2 interactions will increase with increasing iron content, producing larger energy barriers against spin reorientation. Holes in the magnetic lattice (Cu ions) will reduce the barriers for a limited number of spins, which may then be locked into a preferential alignment on cooling in the field by one of the mechanisms described earlier. The M-H curves at 4.2K (Figures 4-11 and 12) from $Fe_{0.8}Cu_{0.2}Rh_2S_4$ and $Fe_{0.9}Cu_{0.1}Rh_2S_4$ demonstrate the increasing energy barriers by the reduction in the width of the hysteresis curve of the zero-field cooled sample with increasing iron content. The remanent moment of the high-field cooled

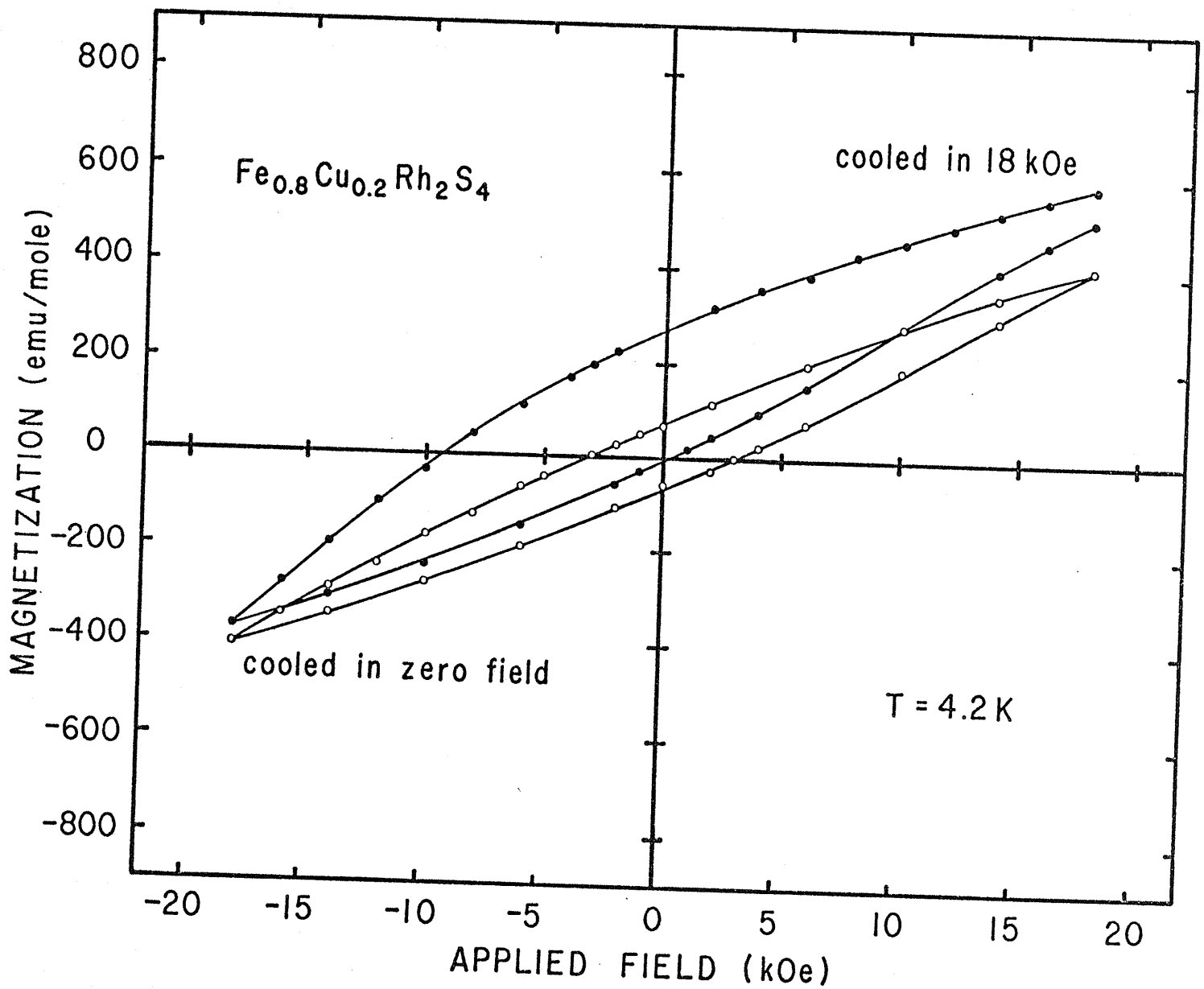
800
600
400
200
0
-200
-400
-600
-800
MAGNETIZATION (emu/mole)
$Fe_{0.8}Cu_{0.2}Rh_2S_4$
cooled in 18 kOe
cooled in zero field
T = 4.2 K
-20
-15
-10
-5
0
5
10
15
20
APPLIED FIELD (kOe)

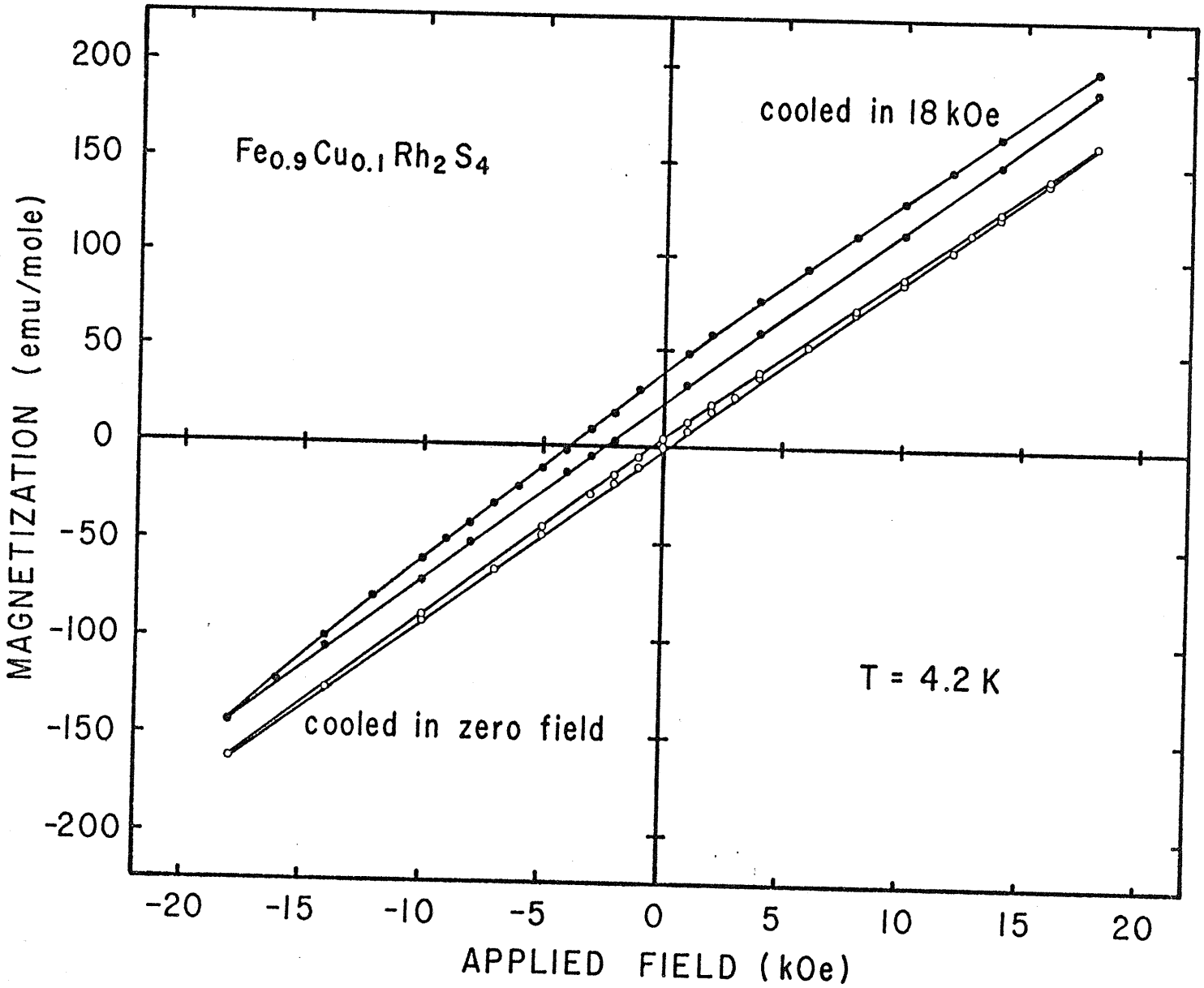

FIGURE 4-12: The magnetization as a function of applied field at 4.2 K for $Fe_{0.9}Cu_{0.1}Rh_2S_4$.

sample is also reduced as the number of spins which can be reoriented (i.e. number of copper ions) is reduced.

These results are summarized in Figure 4-13. At 4.2 K, the width of the hysteresis curve and the moment in 10kOe of the zero-field cooled samples, and the remanent moment of the high-field cooled samples, all peak approximately for the composition $Fe_{0.75}Cu_{0.25}Rh_2S_4$.

Thermal energy assists the preferentially oriented spins in overcoming the anisotropy barriers and thus the shifted hysteresis, as measured by the remanent moment of the high-field cooled samples, decreases on warming. At a sufficiently high temperature (T_B), thermal energy is sufficient to overcome the anisotropy barriers and the remanence disappears. T_B was difficult to measure accurately but was constant for all the iron-rich samples within the accuracy of the measurements. T_B was found to be 35 ±5 K, slightly below the minima in the χ_m^{-1} v T curves interpreted as T_N. The remanent moment approaches zero gradually, rather than a sharp drop at T_B, indicating a distribution in the heights of the energy barriers for different spins. This must be expected since these barriers depend upon the number, position and orientation of quite distant magnetic neighbours.

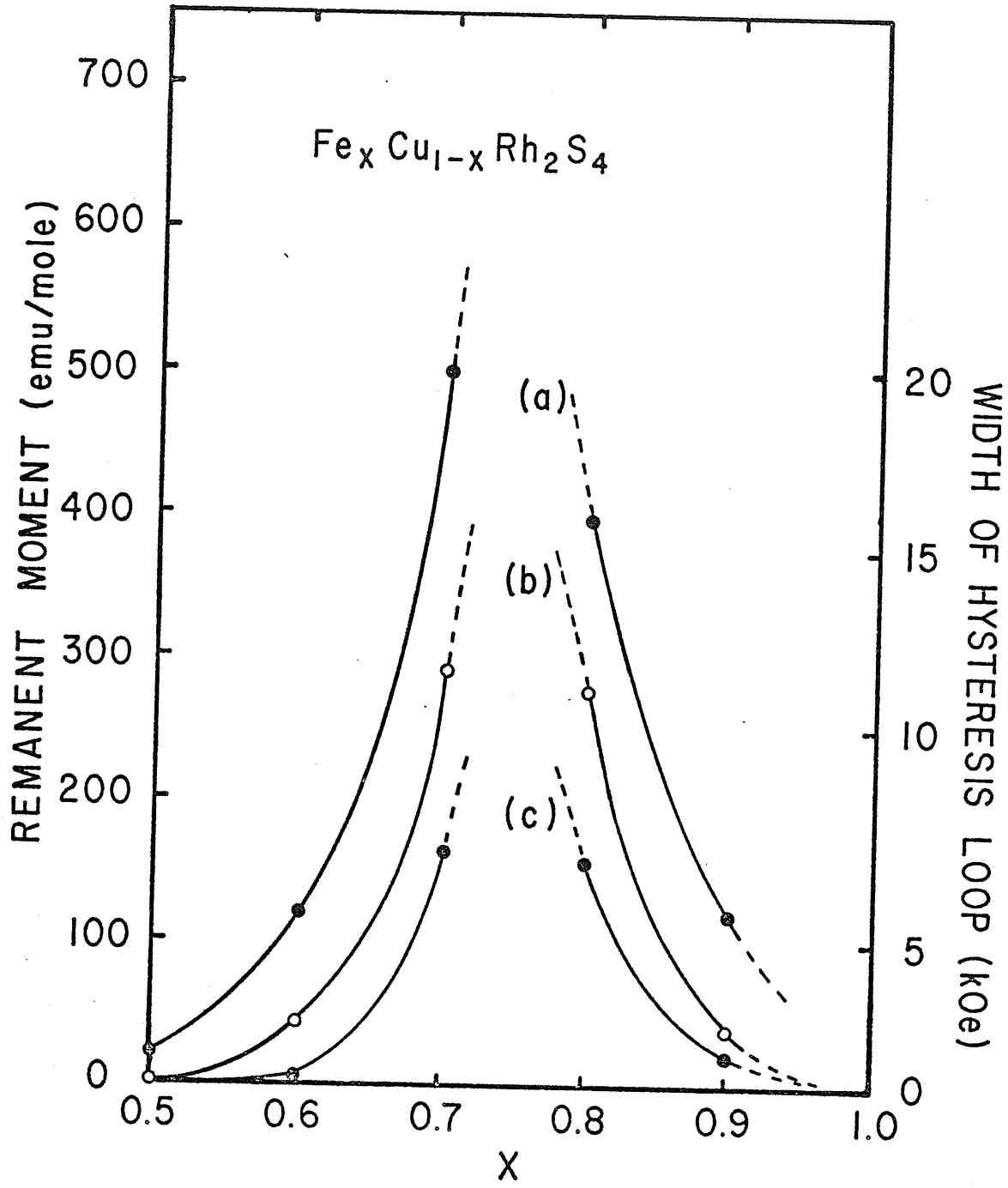

FIGURE 4-13: The compositional dependence of a) the moment in 10 kOe and b) the width of the hysteresis curves of the '0' field cooled samples, and c) the remanent moment of the high field cooled samples at 4.2 K.

5. Mossbauer-Effect Measurements

As was explained earlier, iron enriched with ^{57}Fe was used to prepare the material for the Mössbauer absorbers. Since this limited sample sizes to less than 100 mg, weighing errors were large and so the actual Fe:Cu ratios (x values) of the compounds were determined from their lattice parameters. Mössbauer spectra were recorded in the temperature range 2 K - 300 K and results were generally in good agreement with the magnetization investigation. Complications did arise however in interpreting the low temperature results from the iron-rich end of the series, where computer fitting was unreliable due to the broad overlapping lines of the Mössbauer patterns. Figures 4-14 and 4-15 show examples of spectra from $Fe_xCu_{1-x}Rh_2S_4$ with $x \leqslant 0.5$. Above the ordering temperature the patterns may be fitted with a single peak and below with a simple six-line pattern showing zero quadrupole shift. The absence of any measurable quadrupole splitting suggests Fe^{3+} ions in this composition range[26] as do the isomer shifts of the spectra. However with $x < 0.5$ there is a distribution of magnetic and non-magnetic neighbours which might be expected to produce line broadening, if not actual splitting into subspectra. The ordering temperatures of $Fe_{0.3}Cu_{0.7}Rh_2S_4$ and $Fe_{0.5}Cu_{0.5}Rh_2S_4$ agree with those found from magnetization measurements and are surprisingly high for all the low iron content samples. For samples with $x = 0.30$ and $x = 0.19$, ordering temperatures of 124 K and 48 K were

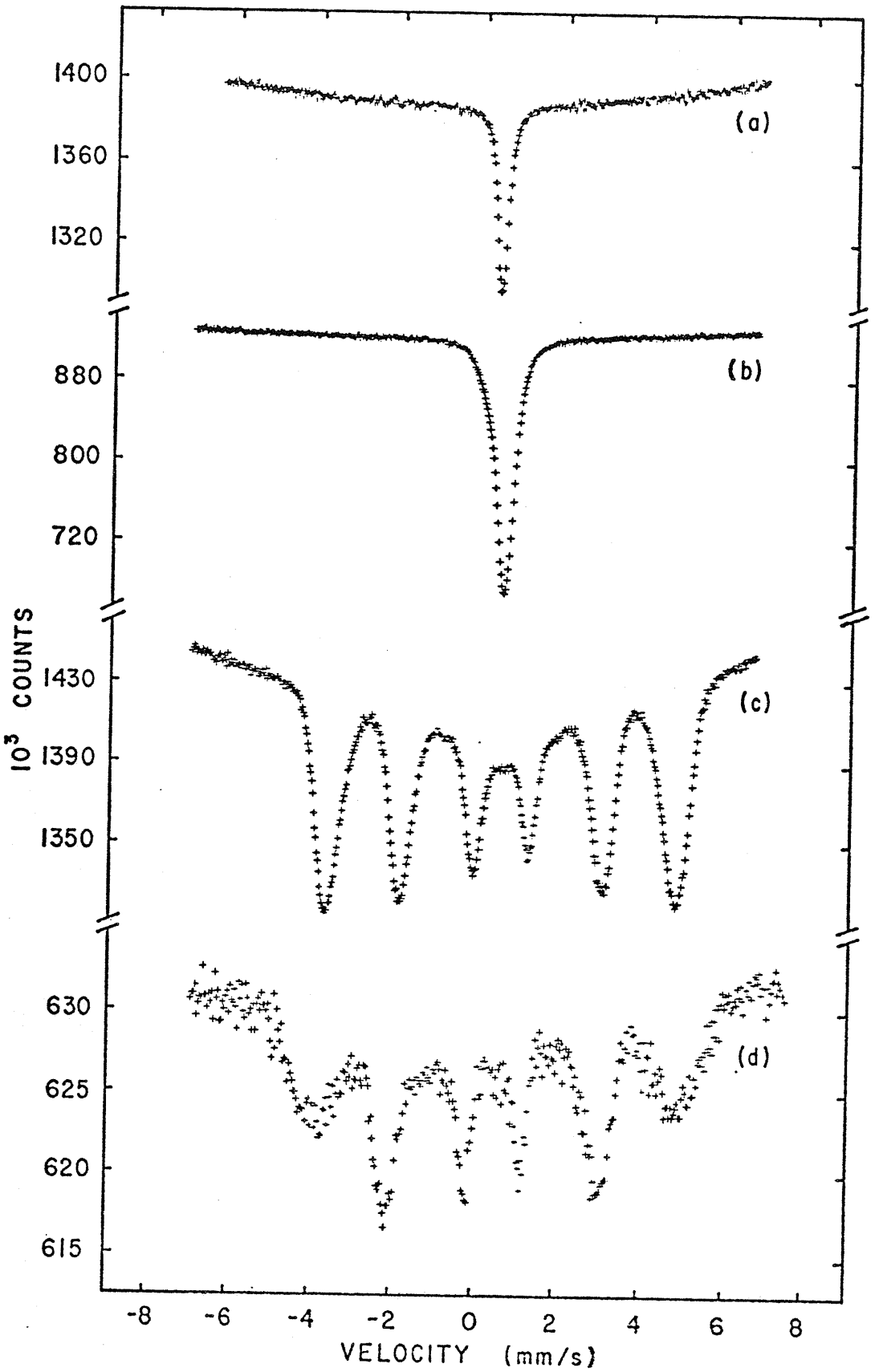

FIGURE 4-14: Mössbauer spectra from $Fe_{0.19}Cu_{0.81}Rh_2S_4$ at a) 300 K b) 77 K c) 4.2 K and d) at 4.2 K in an applied field of 50 kOe.

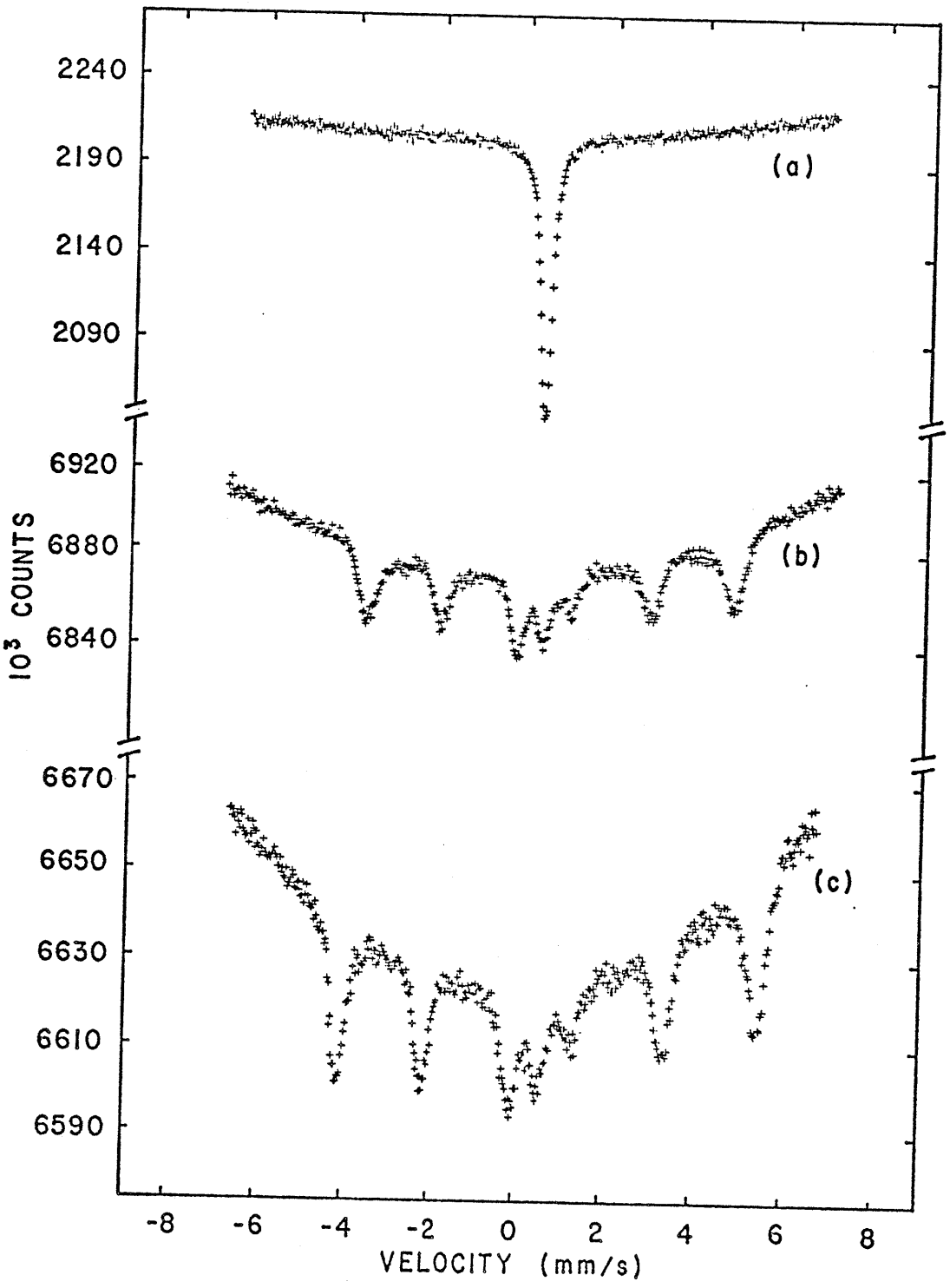

FIGURE 4-15: Mössbauer spectra from $Fe_{0.5}Cu_{0.5}Rh_2S_4$ at a) 300 K b) 77 K and c) 4.2 K.

measured when the magnetic ion content of these compounds is less than 5% and 3% by weight respectively. The magnetic interactions must therefore act over very large distances which would indicate that they do so via a band polarization mechanism. At 4.2 K hyperfine fields of 263.6 kOe and 296.2 kOe were found for x = 0.19 and x = 0.5 respectively. Figure 4-14d shows a spectrum of $Fe_{0.19}Cu_{0.81}Rh_2S_4$ at 4.2 K in an external field of 50 kOe. The presence of the $\Delta m = 0$ lines is expected from an antiferromagnetic powder. Due to the angular distribution of hyperfine fields with respect to the applied field, the spectrum shows line broadening. The splitting of the nuclear levels is proportional to $m_I H$ therefore this broadening is more severe in the outer lines (Table 1-1).[27] As the iron content is increased the possibility of ionic compounds of the form $(Fe^{2+}_{(1-y)}Fe^{3+}_{y})_x Cu^{1+}_{1-x}Rh_2S_4$ arises. However, as can be seen in Figure 4-16, the Mossbauer patterns show a single averaged spectrum although there is significant line broadening, particularly in the case of $Fe_{0.65}Cu_{0.45}Rh_2S_4$, both above and below the ordering temperature. This broadening may be caused by localization of electrons as the temperature is lowered to give both Fe^{2+} and Fe^{3+}, or it could simply be a result of sites with differing numbers of magnetic neighbours. The isomer shift values are higher than those from compounds with $x \leq 0.5$ and increase with iron content. The hyperfine fields extrapolated to T = 0 K decrease as the iron content is increased. Both of these effects are to be expected if

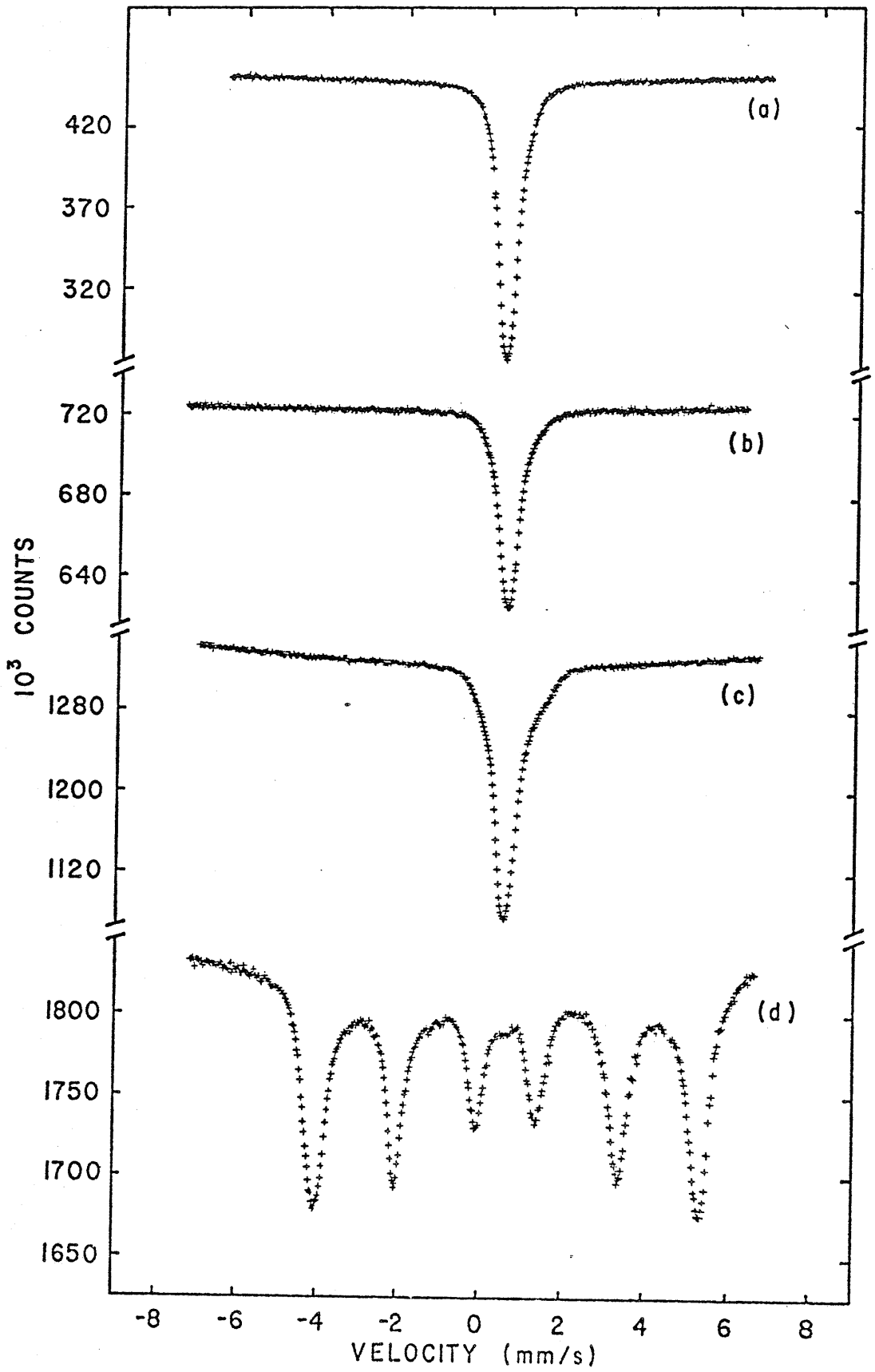

FIGURE 4-16: Mössbauer spectra from $Fe_{0.6}Cu_{0.4}Rh_2S_4$ *at a) 300 K b) 200 K c) 77 K and d) 4.2 K.*

what is being observed is an average spectrum from the Fe^{2+} and Fe^{3+} ions, with a fast electron exchange between the two, as suggested by Haacke and Nozik[27] for iron on the A-sites of $Fe_{1-x}Cu_xCr_2S_4$. If the exchange frequency is $>10^8$ s^{-1}, as explained in Chapter I, the Mössbauer ion will see an averaged charge. This situation is analogous to the electron 'hopping' mechanism which takes place between Fe^{2+} and Fe^{3+} ions on the octahedral sites of the spinel Fe_3O_4.[28] In the composition range $0.5 < x < 0.7$, lowering the temperature to 4.2 K does not slow the electron exchange frequency sufficiently to allow the divalent and trivalent iron ions to experience separate well defined magnetic hyperfine interactions. Additional line broadening will be caused by the distribution of hyperfine fields and quadrupole interactions from sites with different numbers of magnetic neighbours. $Fe_{0.65}Cu_{0.35}Rh_2S_4$ shows a small quadrupole shift and an 'averaged' hyperfine field of 285.2 kOe at 4.2 K. $Fe_{0.7}Cu_{0.3}Rh_2S_4$ shows evidence for two overlapping 6-line patterns at 4.2 K (Figure 4-17). The spectrum shifts at 4.2 K are 0.599 mm/s and 0.802 mm/s, and the hyperfine fields 274.5 kOe and 244.3 kOe respectively. The outer pattern (that with the larger hyperfine field) shows zero quadrupole shift whereas the inner pattern has a quadrupole shift of .222 mm/s. This indicates that electron localization is being observed as the temperature is lowered. The spectrum shift and zero quadrupole shift of the outer pattern are the same as those observed at 4.2 K

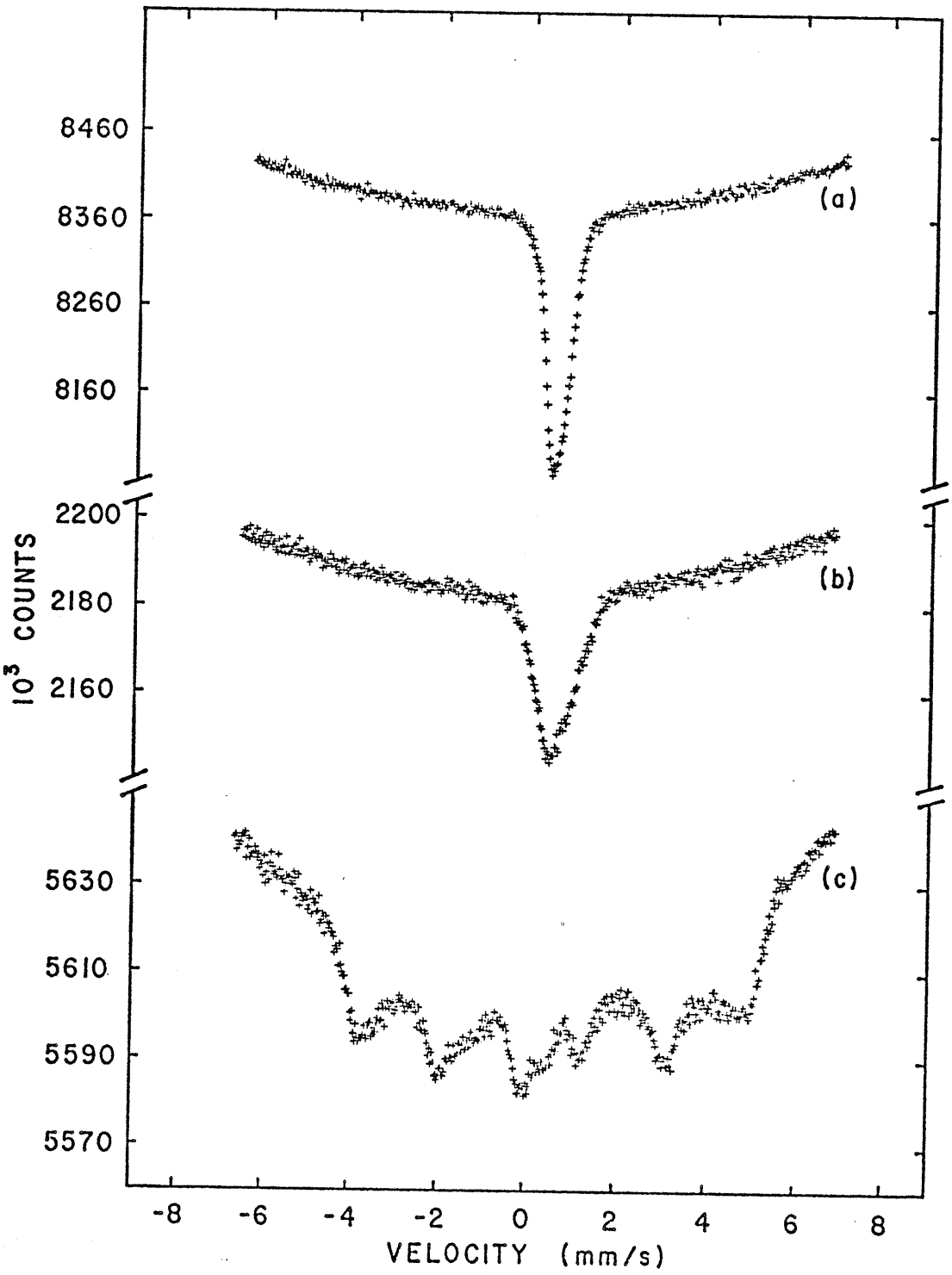

FIGURE 4-17: Mössbauer spectra from $Fe_{0.7}Cu_{0.3}Rh_2S_4$ at a) 300 K b) 77 K and c) 4.2 K.

in $Fe_{0.5}Cu_{0.5}Rh_2S_4$ (Fe^{3+} ions) and the appearance of a quadrupole shift at spinel tetrahedral sites is characteristic of Fe^{2+} ions. The paramagnetic spectrum at 77 K shows the presence of a singlet and a quadrupole split doublet which disappears as the temperature is raised. The ionic compound would have the formula $Fe^{2+}_{0.4}\ Fe^{3+}_{0.3}\ Cu^{1+}_{0.3}\ Rh_2S_4$ and the intensity ratio of the two subspectra are in good agreement with this at both 77 K and 4.2 K.

As the iron content is further increased, the Mossbauer spectra become much more complex. Figure 4-18 shows spectra recorded from $Fe_{0.8}Cu_{0.2}Rh_2S_4$. The most striking result is the appearance of a quadrupole splitting at room temperature. Although apparently a simple doublet, the spectra develops structure as the temperature is lowered, showing at least two and possibly more overlapping doublets at 77 K. The compound orders at 46 ±2 K, below which temperature the Mössbauer spectra can again be fitted with two broad overlapping 6-line patterns.

The samples became increasingly difficult to prepare with a spinel structure as the iron content was increased and in fact $FeRh_2S_4$ has never been prepared as a single phase. $Fe_{0.94}Cu_{0.06}Rh_2S_4$ was found to exist as a single phase spinel and a series of Mössbauer spectra from this compound are shown in Figure 4-19. Again, the apparently simple quadrupole split doublet at room temperature is broadened significantly as the temperature is lowered. Magnetic ordering takes place at 138 ±5 K producing the spectrum

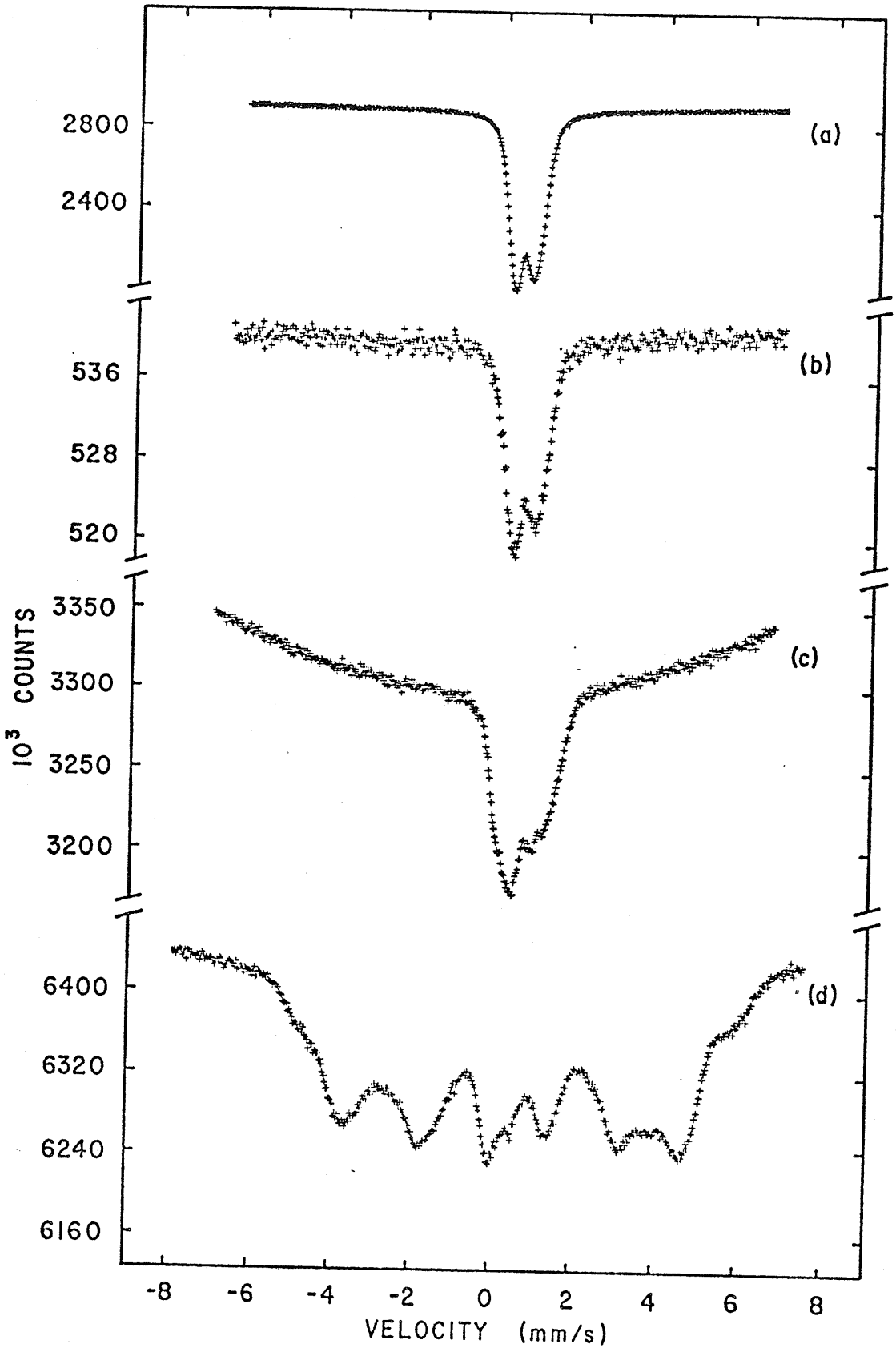

FIGURE 4-18: Mössbauer spectra from $Fe_{0.8}Cu_{0.2}Rh_2S_4$ at a) 300 K b) 200 K c) 77 K and d) 4.2 K.

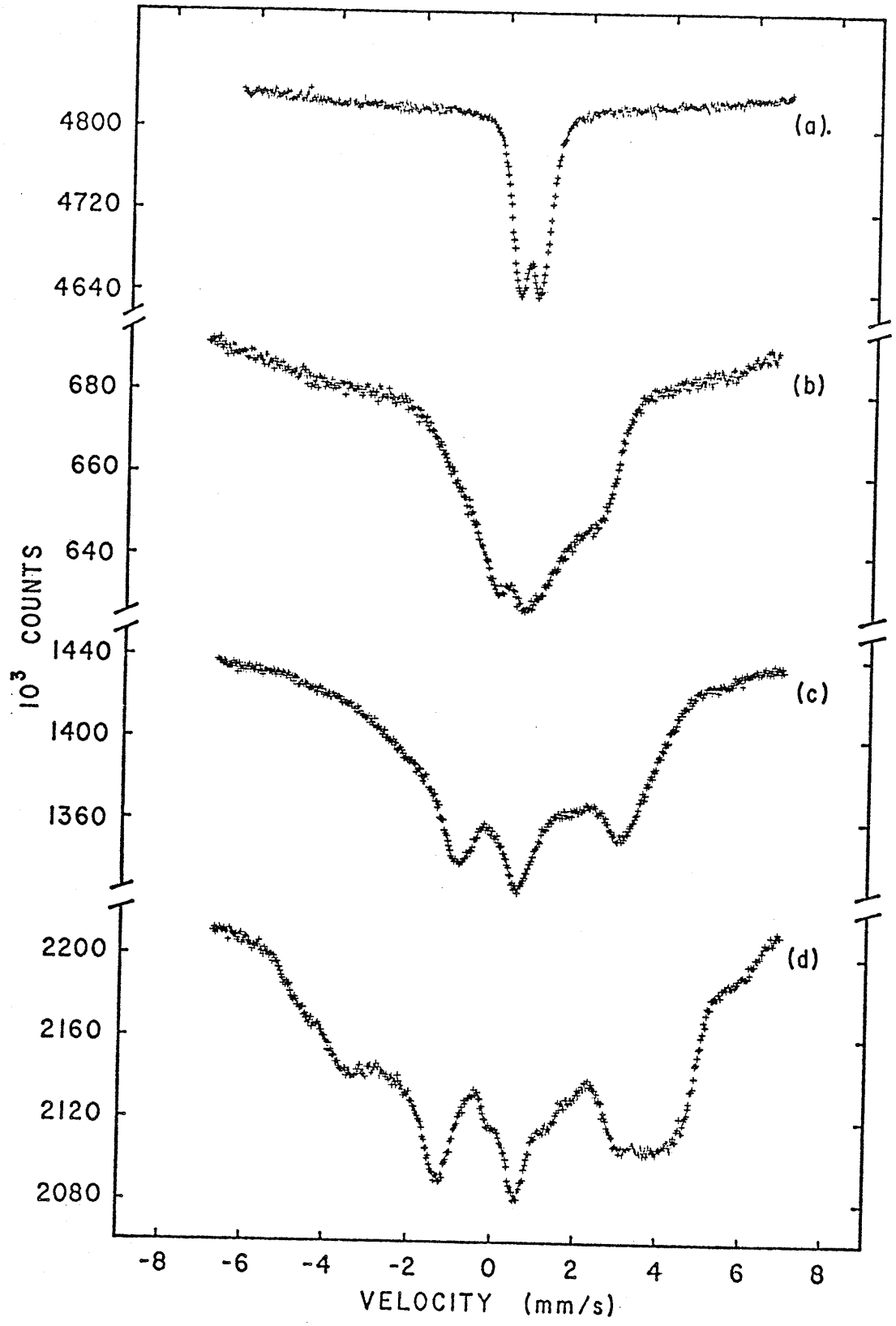

FIGURE 4-19: Mössbauer spectra from $Fe_{0.94}Cu_{0.06}Rh_2S_4$ *at a) 300 K b) 120.5 K c) 40 K and d) 4.2 K.*

shown in Figure 4-19b. This pattern persists until 32 ±5 K when part of the spectrum appears to order in a manner similar to that observed in $Fe_{0.8}Cu_{0.2}Rh_2S_4$. The lower ordering temperature coincides with T_B, the temperature at which the 'frozen' moment disappeared on heating a field cooled sample of $Fe_{0.9}Cu_{0.1}Rh_2S_4$ from 4.2 K.

Spectra were recorded at a number of temperatures in an external field of 50 kOe and showed the sample to be antiferromagnetic between 2 K and 138 K. The unusual spectra between 32 K and 138 K are very similar to those observed for the ferrimagnetic spinel $FeCr_2S_4$ at low temperatures.[30] Further work however[31] proved that the broad lines and lack of resolution were the result of strain induced by sealing the sample in a thermo-setting plastic. The measurements from a loose powder sample showed narrow distinct absorption lines which were in excellent agreement with theoretically fitted data. Examples taken from reference 15 are shown for comparison in Figure 4-20. All the Mössbauer samples from the series were produced in the form of a loose powder held between Beryllium discs and so the strain causing the distorted spectra of Figure 4-19 must be internally induced. Although no crystalline distortion could be found at any temperature in the X-ray investigation, this compound is at the limit of iron content for a spinel structure and from the Mössbauer results it is evident that considerable strain is induced at the individual ion sites.

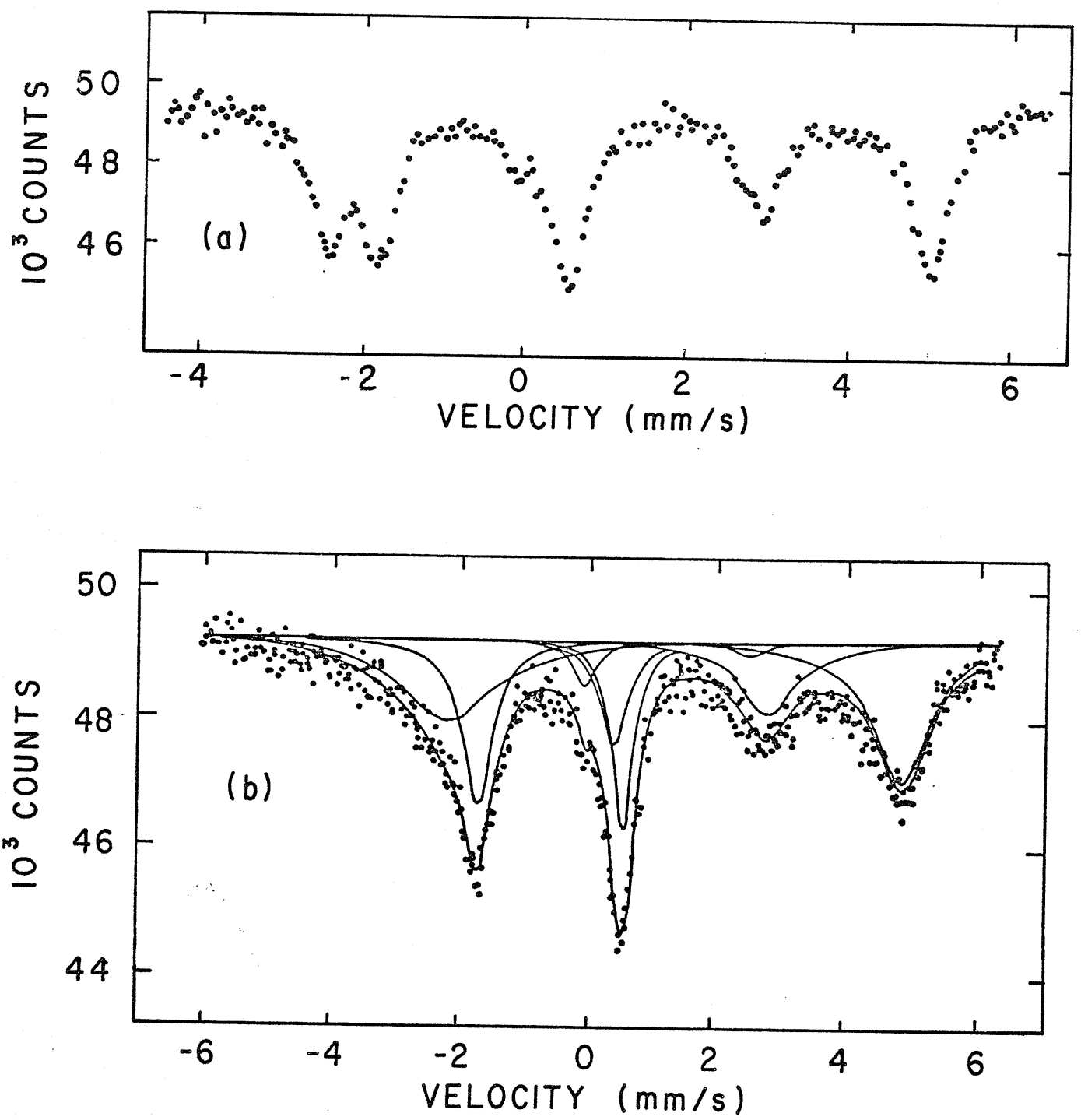

FIGURE 4-20: Mössbauer spectra of $FeCr_2S_4$ at 2 K a) from a loose powder sample and b) from a sample sealed in thermo-setting plastic. (Taken from reference 15).

The final Mössbauer experiment performed on this series was an attempt to verify the 'excess spin' model proposed to explain the frozen moments found in the magnetization investigation. If this model is correct, on cooling, the excess spins align along the applied field. The hyperfine field of these spins will then be reduced by an amount equal to the applied field and the $\Delta m = 0$ lines of their Mössbauer pattern will be absent.

$Fe_{0.65}Cu_{0.35}Rh_2S_4$ was chosen for this experiment since its low temperature spectra were not too complex and a reasonable remanent moment is expected at this composition. The sample was cooled to 4.2 K in an externally applied field of 50 kOe and a Mössbauer spectrum recorded without removing the field. If Figure 4-21b is compared with that from a normal randomly aligned antiferromagnetic powder (Figure 4-14d) it can be seen that Figure 4-21b has a spectrum with a smaller hyperfine field superimposed on the broad antiferromagnetic background. The relative intensity of the $\Delta m = 0$ (2 and 5) lines is also smaller indicating that they are greatly reduced if not absent from the superimposed spectrum. This spectrum may also allow us to choose between the two processes, indistinguishable from magnetization measurements, proposed earlier to explain the locking mechanism of the excess spins. Although the broad lines made computer fitting unreliable, the outer lines of the antiferromagnetic component appear to be simply broadened and show no evidence of splitting. This would be

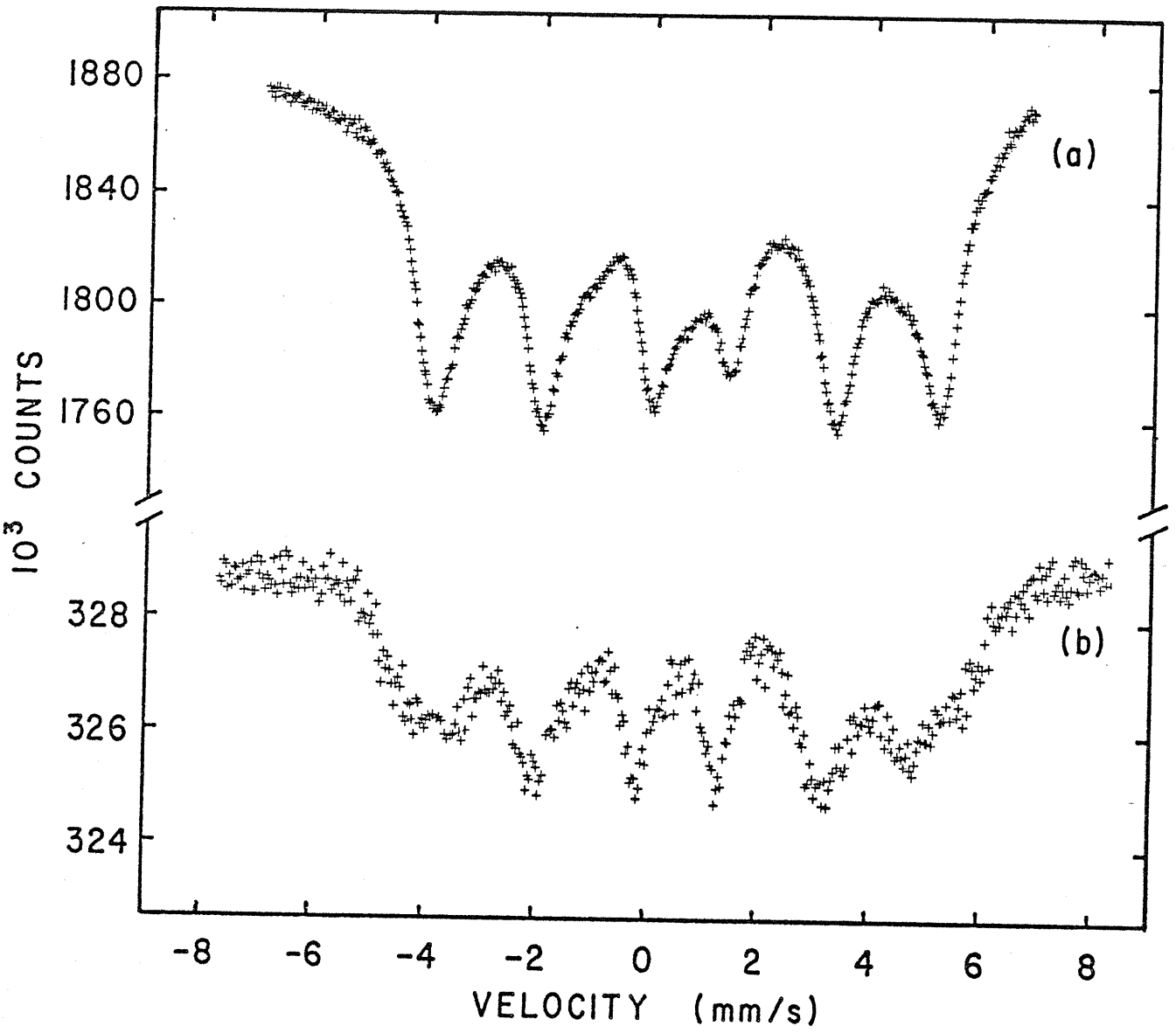

FIGURE 4-21: Mössbauer spectra from $Fe_{0.65}Cu_{0.35}Rh_2S_4$ at 4.2 K a) in zero applied field and b) in an external field of 50 kOe.

expected if the excess spin had a number of preferential directions with an energy barrier between them, since on cooling in an external field, the many antiferromagnetic directions of the powder would remain randomly oriented with respect to this field. If however the excess spins were strongly coupled to the antiferromagnetic lattice which itself rotated to the most preferential direction, the antiferromagnetic directions in the powder sample would form a broad cone around the field direction. In this case, rather than uniform broadening, the outer lines from the antiferromagnetic lattice should split, or at least show structure indicative of the two separate sublattices.

6. Discussion

A summary of isomer shifts and hyperfine fields found at tetrahedral sites for Fe^{2+} and Fe^{3+} ions is shown in Table 4-5. Figure 4-22 shows a plot of the isomer shift at room temperature against iron concentration. There is a definite change from values characteristic of 3+ ions to those characteristic of 2+ ions as the iron content exceeds x = 0.5.

Compound	Formal Ionic State	Isomer Shift rel. to Chromium (mm/s)	Hyperfine Field (kOe)	
Fe_3S_4	Fe^{3+}	0.41	311	32
$CuFeS_2$	Fe^{3+}	0.36	360	33
$Fe_{0.5}Cu_{0.5}Cr_2S_4$	Fe^{3+}	0.46	380	29
$Fe_xCu_{1-x}Cr_2S_4$ $(0 \leqslant x \leqslant 1)$	$Fe^{3+} \rightarrow Fe^{2+}$ increasing x	0.36 → 0.73		27
$FeCr_2S_4$	Fe^{2+}	0.75	206(77K)	30
$Cd_{1-x}Fe_xCr_2S_4$	Fe^{2+}	0.71 → 0.80	210(77K)	4
$FeRh_2S_4$ (impure)	Fe^{2+}	0.71	140(77K)	18

TABLE 4-5: A summary of hyperfine fields and isomer shifts found at tetrahedral sites for Fe^{2+} and Fe^{3+} ions.

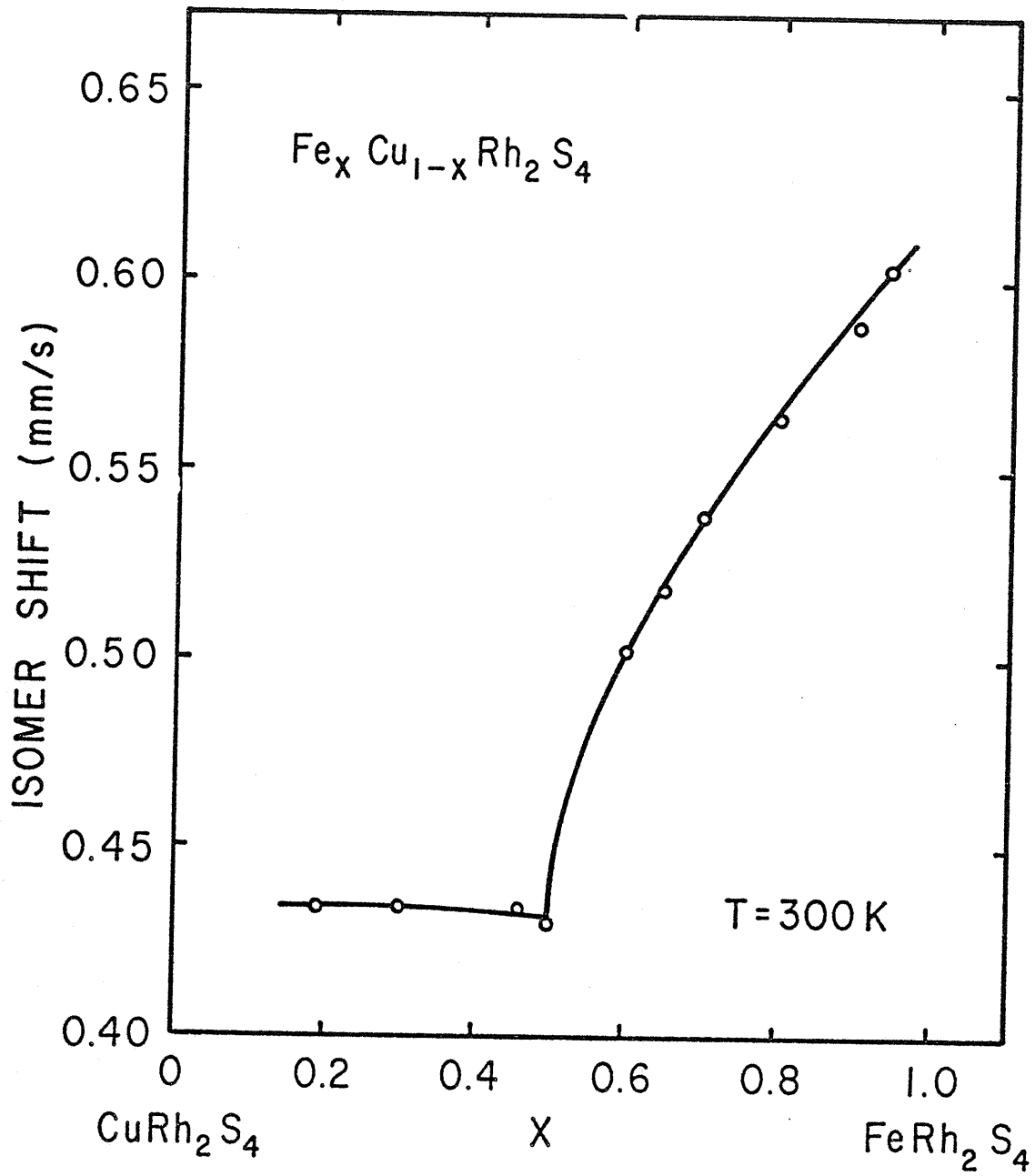

FIGURE 4-22: The compositional dependence of the isomer shift of $Fe_x Cu_{1-x} Rh_2 S_4$.

Values from non-enriched samples are included. The ordering temperature as measured from the Mössbauer results is plotted against iron concentration in Figure 4-23. It peaks at the fully ordered $Fe_{0.5}Cu_{0.5}Rh_2S_4$ as expected and drops suddenly with increased iron content. The Mössbuaer results showed ordering of $Fe_{0.94}Cu_{0.06}Rh_2S_4$ and $Fe_{0.9}Cu_{0.1}Rh_2S_4$ at 138 K and 107 K respectively, and not just above T_B ($\sim$35K) as indicated from the magnetization measurements. The rise in Néel temperature occurs with the approach to the $CoRh_2S_4$ type of ordering referred to earlier and already proposed for the magnetic structure of $FeRh_2S_4$.[15]

Following the work of Lotgering et al.[2, 16, 20, 25] the band diagrams of Figure 4-24 are presented for the $Fe_xCu_{1-x}Rh_2S_4$ series. The energy E is plotted versus the density of states g. An area $\int gdE$ gives the number states per molecule. The conduction band arises from a broadening of the metal 4s electron levels due to the large overlap of metal s functions and the sulphur p functions. The outer sulphur 3p electrons form a broad valence band.[29] The metal 3d electrons are more localized than the 4s electrons and hence the overlap with the p functions is much smaller giving a narrow band of 3d levels. Many such models have been proposed for sulphides, with the 3d levels positioned both in the energy gap and overlapping either valence or conduction bands. The clear evidence for Fe^{3+} in $Fe_{0.5}Cu_{0.5}Rh_2S_4$ lead to the choice of the Lotgering model[2] over that of Goodenough[8] for copper containing spinel

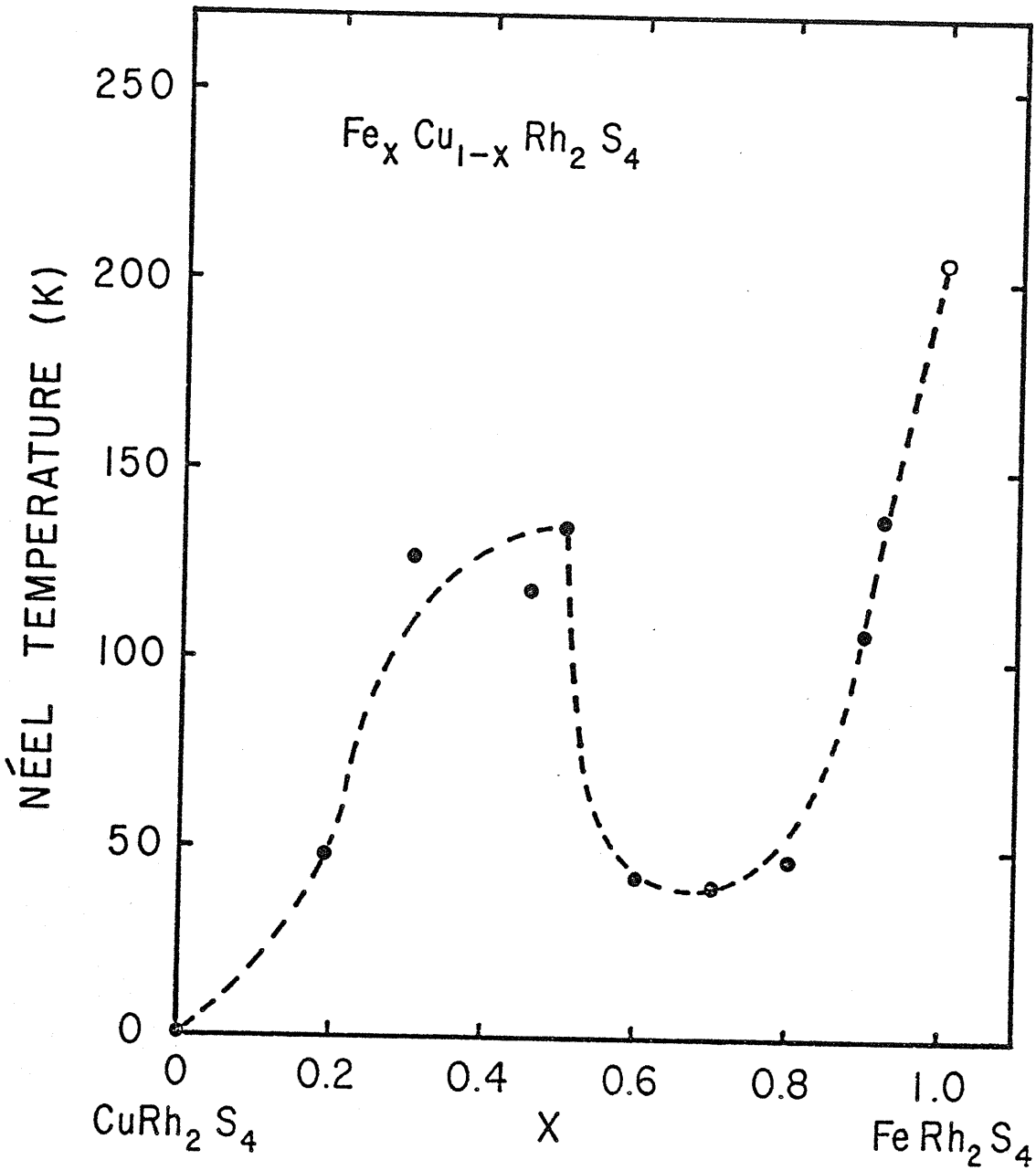

FIGURE 4-23: The compositional dependence of the ordering temperature of $Fe_xCu_{1-x}Rh_2S_4$.

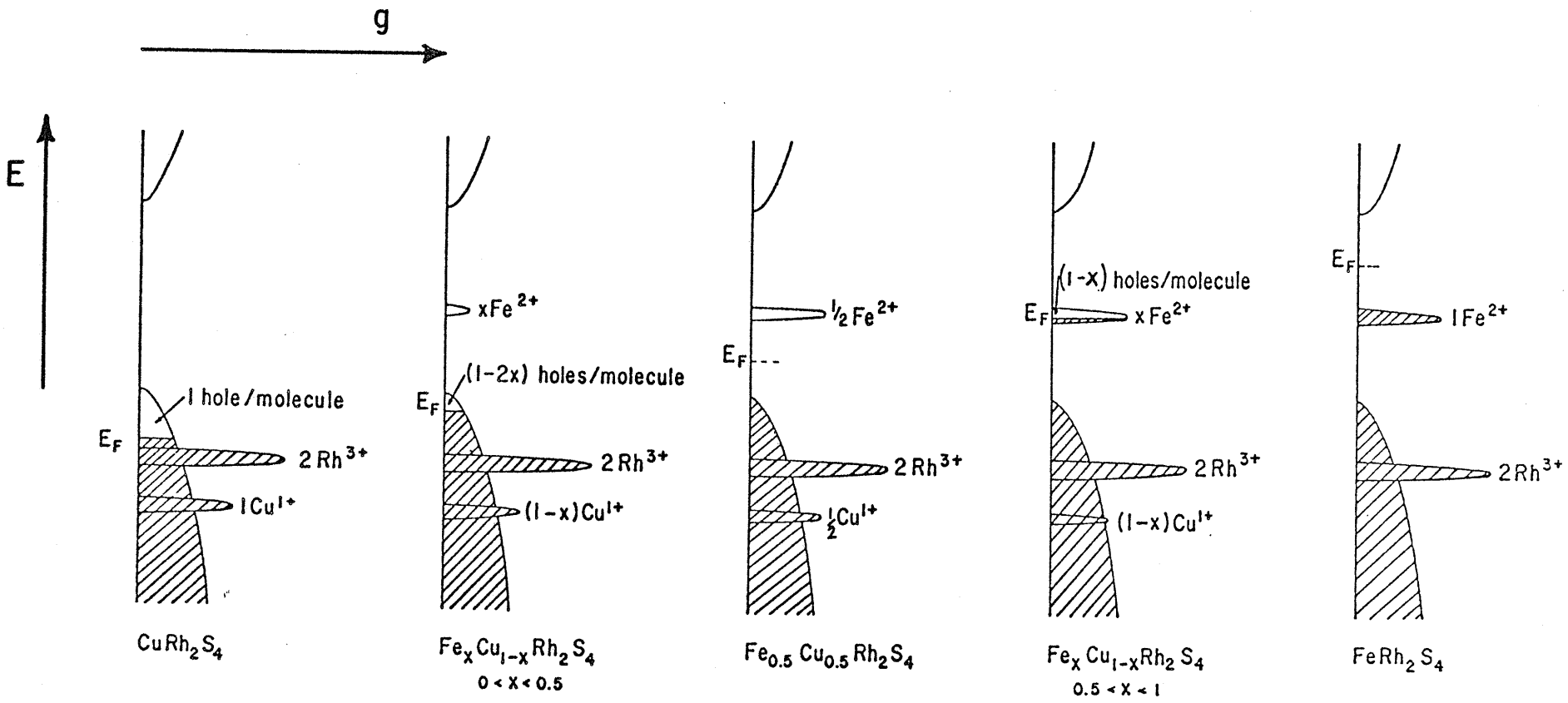

FIGURE 4-24: Energy level schemes for the series $Fe_xCu_{1-x}Rh_2S_4$. The Energy E is plotted versus the density of states g, and $\int g dE$ gives the number of states per molecule.

sulphides, with monovalent copper represented by a filled 3d band for Cu^{1+} lying far below the top of the valence band. A completely filled Rh^{3+} band overlaps the filled part of the valence band throughout the series. The Fe^{2+} band lies in the energy gap, an occupied level representing a 3d electron bound in the Fe^{2+} ion and an empty level a Fe^{3+} ion. With the Fermi level E_F situated in the 3d band a mixture of Fe^{2+} and Fe^{3+} ions is present, whereas with E_F below the top of the valence band electrons are missing from sulphur 3p states. The band scheme of $CuRh_2S_4$ is taken from the work of Lotgering.[20] The valence band contains one hole/molecule leading to p type metallic conduction and a small temperature independent susceptibility. The hole is associated with the sulphur 3p electrons leading to the formal valencies $Cu^{1+}Rh_2^{3+}S_3^{2-}S_1^{-}$. As iron replaces copper, an empty Fe^{2+} band (Fe^{3+} ions) appears in the band gap and the number of holes in the valence band is reduced. The valencies can now be represented by the formula $Fe_x^{3+}Cu_{1-x}^{1+}Rh_2^{3+}S_{3+2x}^{2-}S_{1-2x}^{1-}$ for $0 \leqslant x \leqslant 0.5$. That is one hole/molecule for $CuRh_2S_4$ and zero holes for $Fe_{0.5}^{3+}Cu_{0.5}^{1+}Rh_2^{3+}S_4^{2-}$. In this case, the series will be p type metallic for low iron content members as suggested earlier, and become semiconducting for $Fe_{0.5}Cu_{0.5}Rh_2S_4$. Conduction could then take place via holes in the valence band or via electrons in the narrow Fe^{2+} d band. Plummier reported resistivity results from two samples of $Fe_{0.5}Cu_{0.5}Rh_2S_4$, one of which was p-type semiconducting and the other an

n-type semiconductor. With the above model, very slight compositional variations would explain this effect. With $0.5 < x < 1$ the Fe^{2+} band is partially filled producing a mixture of Fe^{2+} and Fe^{3+} ions. Electron localization is seen at low temperatures in the Mössbauer measurements only for the samples with $x \geqslant 0.7$. $FeRh_2S_4$ would be semiconducting on this model if it existed in the spinel structure. In fact resistivity data from the impure sample reported in reference 15 do show semiconducting behaviour and the magnetization measurements do indicate Fe^{2+} iron with antiferromagnetic, $CoRh_2S_4$ type ordering.

REFERENCES - CHAPTER IV

1. E.J.W. Verwey and E.L. Heilmann, J. Chem. Phys. 15, 174 (1946).
2. F.K. Lotgering and R.P. van Stapele, J. Appl. Phys. 39, 417 (1968).
3. P.F. Bongers, C. Haas, A.M.J.G. Van Run and G. Zanmarchi, J. Appl. Phys, 40, 958 (1969).
4. M.R. Spender and A.H. Morrish, Can. J. Phys., 49, 2659 (1971).
5. P.R. Locher and R.P. Van Stapele, J. Phys.Chem. Solids 31, 2643 (1970).
6. A.H. Morrish, The Physical Principles of Magnetism, John Wiley , New York (1965).
7. J.B. Goodenough, Magnetism and the Chemical Bond, John Wiley and Sons, New York (1963).
8. J.B. Goodenough, J. Phys. Chem. Solids 30, 261 (1968).
9. G. Blasse, Phys. Lett. 19, 110 (1965).
10. G. Blasse and D.J. Schipper, J. inorg. nucl. Chem. 26, 1467 (1964).
11. R. Plumier and F.K. Lotgering, Solid State Commun. 8, 477 (1970).
12. J.S. Smart, Effective Field Theories of Magnetism, Sanders, Philadelphia (1966).
13. P.W. Anderson, Phys. Rev. 79, 705 (1950).

14. R.E. Tressler and V.S. Stubican, N.B.S. Pub. 364, (Sol. State Chem. Proc. of 5th Mat. Res. Symp., 1972). p. 695.

15. M.R. Spender, Ph.D. Thesis, University of Manitoba (1973).

16. F.K. Lotgering, Philips Res. Rep., 11, 190 (1956).

17. P. Gibbart, J.L. Dormann, and Y. Pellerin, Phys. Stat. Solidi, 36, 187 (1969).

18. M.R. Spender and A.H. Morrish, Proc. 5th International Conference on Mossbauer Spectroscopy, Czechoslovakia (Sept. 1973).

19. C. Haas, Rev. Solid State Sci., 1, 47 (1970). Chemical Rubber Co., Cleveland, Ohio.

20. F.K. Lotgering, J. Phys. Chem. Solids, 30, 1429 (1969).

21. N.F.M. Henry, H. Lipson and W.A. Wooster, The Interpretation of X-Ray Diffraction Photographs, Macmillan, London (1961).

22. J.B. Nelson and D.P. Riley, Proc. Phys. Soc. 57, 160 (1945).

23. J.C. Ward, Rev. pure and appl. Chem. 20, 1975 (1970).

24. G. Blasse, Philips Res. Repts. 18, 383 (1963).

25. F.K. Lotgering, J. Phys. Chem. Solids 29, 699 (1967).

26. M. Eibschutz, S. Shtrikman and Y. Tenenbaum Phys. Lett. 24A, 563 (1967).

27. H.N. Ok et al., Phys. Rev. 187, 704 (1969).

28. G. Haacke and A.J. Nozik, Solid State Commun. 6, 363 (1968).

29. A. Ito, K. Ôno and Y. Ishikawa, J. Phys. Soc. Japan 18, 1465 (1963).

30. F.K. Lotgering, R.P. van Stapele, G.H.A.M. Van Der Stein and J.S. Van Wieringen, J. Phys. Chem. Solids 30, 799 (1968).

31. M.R. Spender and A.H. Morrish, Can. J. Phys., 50, 1125 (1972).

32. M.R. Spender and A.H. Morrish, Solid State Commun., 11, 1417 (1972).

33. J.M.D. Coey, M.R. Spender and A.H. Morrish, Solid State Commun. 8, 1605 (1970).

34. N.N. Greenwood and H.J. Whitfield, J. Chem. Soc. A, 1697 (1968).

CONCLUSIONS

Mössbauer spectra of Fe_7Se_8 have been shown to be exceedingly complex. Apart from the fact that there are two distinct ordered phases below the ordering temperature, a small amount of cold-working apparently introduces either vacancy disorder in the planes or additional phases. The paramagnetic component may arise from $FeSe_2$ or perhaps from iron ions with a large number of vacancies on nearest neighbour cation sites. However, by employing correct preparation methods, single phase samples were produced with either the 3c or 4c superstructures and a variety of X-ray techniques were used to verify the sample structures.

Based on the relative line intensities, and with the aid of spectra taken in applied magnetic fields, the individual six-line patterns of the Mössbauer spectra were ascribed to cations located in different crystallographic sites. Computer fitting was limited to spectra collected in the temperature range 77 to 300 K. Spectra were recorded at temperatures below this range, but their complexity was much greater leading to increased uncertainty in the analysis.

Both magnetization data and Mössbauer spectra provided clear evidence for a large spin-rotation in the 3c structure at $\sim$ 130 K and hence confirm earlier neutron-diffraction results. The abrupt changes in the various parameters, characteristic of such a rotation, were not present in data recorded from 4c samples. From isomer shift measurements

it was concluded that all the iron ions were in the high-spin ferrous state, showing the suggested ionic structure, with Fe^{3+} ions on alternate c-layers, to be invalid. A simple band diagram was proposed to account for the charge imbalance created with all the iron in the Fe^{2+} state.

The compounds $Fe_xCu_{1-x}Rh_2S_4$ were shown to exist in spinel form for $0 \leqslant x \leqslant 0.94$. A low temperature X-ray investigation indicated an absence of any distortions from the spinel structure above 4.2 K for all members of the series. By taking advantage of the depression of the scattering factor of iron close to its K absorption edge, superlattice lines characteristic of spinel A site ordering were found in the range $0.46 \leqslant x \leqslant 0.7$. This confirmed earlier neutron diffraction work on $Fe_{0.5}Cu_{0.5}Rh_2S_4$.

Magnetization measurements showed the series to be anti-ferromagnetic, although a spontaneous moment could be induced for $0.5 < x \leqslant 0.94$ by cooling through the Néel point in an externally applied field. This moment was 'locked in' at low temperatures producing hysteresis loops which were displaced along the field axis. An explanation of this frozen moment was given based on a model with excess iron spins randomly distributed on the copper A sublattice.

Both susceptibility measurements above the ordering temperature, and isomer shift measurements at room temperature, indicated a gradual change in valence state of the iron from Fe^{3+} for $x \leqslant 0.5$ to Fe^{2+} as $x \rightarrow 1$. The low temperature Mössbauer measurements showed evidence for the presence of

both Fe^{2+} and Fe^{3+} ions for $x \geqslant 0.7$, with intensity ratios in good agreement with those required for ionic charge balance. The low temperature spectra became increasingly complex as $x \rightarrow 1$, the broad overlapping lines preventing theoretical fitting for $x \geqslant 0.9$. A possible explanation for this phenomenon was given in terms of induced strain at the individual iron sites.

Energy band diagrams were postulated which were consistent with the observed compositional dependence of the conductivity, valence states and magnetic data.

Further work.

a) The low temperature X-ray equipment now provides a means of examining the temperature dependence of the lattice parameters of '3c' and '4c' Fe_7Se_8. This could produce further evidence relating to the different spin rotation processes in the two superstructures. The single crystal X-ray work described in Chapter III should be extended to include a detailed investigation of the reported triclinic distortion in the 4c superstructure.

b) During high temperature magnetization measurements, a sample of Fe_7Se_8 was cooled through its ordering temperature in the remanent field of the electromagnet ($\sim$ 1 Oe). This field was reduced to zero when the feedback circuit was activated, and on further cooling, the magnetization of the sample was seen to change direction. Further investigation was not undertaken at the time due to

decomposition of the samples at high temperatures. However, if the samples were sealed in glass ampules, this phenomenon could be examined and related to similar effects observed in naturally occuring pyrrhotite (Fe_7S_8). It is possible that samples of pyrrhotite cooled in the Earth's field may exhibit a magnetization in the opposite direction to this field. It is important that this mechanism be fully understood if naturally occuring magnetic minerals are to be used to determine features of the Earth's ancient magnetic field.

c) By using a single crystal absorber, the complexity of the low temperature Mössbauer spectra of Fe_7Se_8 could be reduced, which would enable the theoretical fitting of the spectra to be extended down to 2 K. With a more sophisticated crystal-growing technique, larger single crystals could be produced. These could then be aligned and sliced to provide suitable Mössbauer absorbers.

d) The most important addition to the data so far reported on the series of compounds $Fe_xCu_{1-x}Rh_2S_4$ would be an investigation of the electrical properties as a function of concentration. Resistivity and Hall Effect measurements would provide valuable information as to the number and sign of the majority carriers which in turn would test the validity of the proposed energy band schemes.

e) The peaking of the remanence, hysteresis and moment at the approximate concentration $Fe_{0.75}Cu_{0.25}Rh_2S_4$

suggested by Figure 4-13, should be confirmed by magnetization measurements on such a sample, and further samples in the range $0.3 < x < 0.5$ could provide evidence for the change from metallic to semiconducting behaviour.

f) The final suggestion for further work is again associated with the complexity of the Mössbauer results from Fe_7Se_8. More insight into the nature of the magnetic interactions taking place in this compound may be gained if the data could be simplified by reducing the number of different iron sites being examined. To this end, several attempts were made to create NiAs-type compounds of the form $Fe_3A_4X_8$ where A = V or T_i and X = S, Se or Te. Partial success was achieved and work is continuing in this area.

APPENDIX

A program for determining an accurate value for the cell dimension, a, of a cubic crystal using a biased least squares fit to a plot as a (θ) against the Nelson-Riley function, $1/2\left(\frac{\cos^2\theta}{\sin\theta} + \frac{\cos^2\theta}{\theta}\right)$

```
1.          Character*80 Name
2.          Integer H,K,L
3.          Real A(2,2),W(2),IA(2),IR(2)
      C Program Reads 2Theta Values in Degrees
4.          F(X,T)=(Cos(X)**2/Sin(X)+Cos(X)**2/T)/2
5.          D1(X)=Alam/(2.*Sin(X))
      C     Read in the Name
6.        2 Read(5,700,End=3)Name
7.      700 Format(A80)
8.          Print 100
9.      100 Format('1')
10.         Print 800,Name
11.     800 Format(' ',7X,A80//)
12.         Print 200
13.     200 Format(' ',7X,118('*'))
14.         Print 300
15.     300 Format(' ',7X,'*',5X,'Theta (Degrees)',5X,'*',
           C'D (Angstroms)',5X,'*',5X,'A (Angstroms)',5X,'*',
           C5X,'(Cos(X)**2/Sin(X)+Cos(X)**2/X)/2',5X,'*')
```

```
16.          Print 200
       C     Alam = Wavelength of the Incident Radiation
17.          Alam=1.54434
       C     N = Number of Reflections Indexed
18.          Read 400,N
19.      400 Format(12)
20.          B11=B12=B22=B13=B23=0.
21.          Do 1 I=1,N
       C     T = 2Theta Value of Reflection (H,K,L)
22.          Read 500,T,H,K,L
23.      500 Format(F8.4,3I2)
24.          T=T/2
25.          X=T*.017453
26.          XF=F(X,T)
       C     Now Provide Bias
27.          C2=COTAN(X)**2
28.          D=D1(x)
       C     Now Calculate A(Theta)
29.          AL=SQRT(FLOAT(H**2+K**2+L**2))*D
30.          B11=B11+1/C2
31.          B12=B12+XF/C2
32.          B22=B22+XF**2/C2
33.          B13=B13+AL/C2
34.          B23=B23+AL*XF/C2
35.          Print 600,T,D,AL,XF
36.      600 Format(' ',7X,'*',9X,F7.4,9X,'*',8X,F7.4,8X,'*',
            C8X,F7.4,8X,'*',18X,F6.4,18X,'*')
```

```
37.         1 Continue
38.           Print 200
39.           A(1,1)=B11
40.           A(1,2)=A(2,1)=B12
41.           A(2,2)=B22
42.           W(1)=B13
43.           W(2)=B23
      C       Now do least squares fit
44.           Call LNEQNS(A,2,2,2,W,IA,IR,IER)
      C       IER = 0 indicates fit completed
45.           Print 900, IER,W(2)
      C       W(2) = Gradient and of the fitted line
46.       900 Format(' ',7X,'IER = ',12,'  W(2) = ',F7.4)
47.           Print 777,W(1)
      C       W(1)=Intercept on the 'Y' Axis
48.       777 Format('-',7X,'The Value of the Lattice Parameter
          C Was Found to be ',F7.4,'Angstroms')
49.           Go To 2
50.         3 Print 100
51.           Stop
52.           End
```